MEASUREMENT OF THE TRANSVERSE SPIN POLARIZATION OF THE Λ IN QUASI-REAL PHOTOPRODUCTION AND ELECTROPRODUCTION AT HERMES

BY

AARON ELVIS ANDRUS

B.S., University of Michigan-Dearborn, 1997
M.S., University of Illinois at Urbana-Champaign, 2000

DISSERTATION

Submitted in partial fulfillment of the requirements
for the degree of Doctor of Philosophy in Physics
in the Graduate College of the
University of Illinois at Urbana-Champaign, 2006

Urbana, Illinois

MEASUREMENT OF THE TRANSVERSE SPIN POLARIZATION OF THE Λ IN QUASI-REAL PHOTOPRODUCTION AND ELECTROPRODUCTION AT HERMES

Aaron Elvis Andrus, Ph.D.
Department of Physics
University of Illinois at Urbana-Champaign, 2006
Dr. N. C. R. Makins, Advisor

The mystery of hadron polarization has been a source of both experimental and theoretical interest the last few decades. Measurements of polarizations in such particles as the Λ particle have been done in proton-proton collisions, but studies in positron-proton scattering with high statistical accuracy have been lacking. At the HERMES experiment, the polarization of the Λ and $\bar{\Lambda}$ have been measured in the inclusive, quasi-real photoproduction regime. A positive polarization with respect to the Λ production plane has been observed for the Λ. Also, semi-inclusive deep inelastic scattering (SIDIS) measurements for the Λ have been obtained. The results indicate a small, positive polarization, but more statistics are required to make a more positive statement.

To Mom, Dad, and Dawn.

Acknowledgements

I would like to thank God, first and foremost, Jesus, for dying for my sins, the holy spirit for giving me the strength to make it through each day, and for our Blessed Mother Mary, for being the floodgate through which all these Graces and Blessings flow.

I would like to thank Mom and Dad for being awesome parents. They gave me shelter, food, clothing, and love (and a lot of other stuff). They were patient with me and gave me the opportunity to make the most of my educational experience. My sister, Dawn, has also been most supportive and is an inspiration of hard work. My family is one of the greatest Blessings that God has given me.

Another source of joy and happiness has been my friends. It is inevitable that I leave some people out (my apologies in advance), but that is not meant to lessen the feelings of gratitude that I feel towards you. Where to begin, but at the beginning. Patrick, I am not sure if you'll ever read this, but you were a good friend and a great help in getting through quantum mechanics. Andreas and Michael, two better roommates I could not have asked for in Sherman Hall. You helped me see past the books and constant studying. Your time here was too short. Joon, my buddy, you are an inspiration of life. I always saw you with a smile on your face... never lose that.

Thanks to the old crew back in the basement of the ESB: Seongshik, Dario, Soren, and Maitri. Seongshik, I told you before, I'll tell you again, you have the most infectious laugh I have ever heard. You taught me what Korean I know (the most important of which is the expression for "My Friend"). I wish you and Kim all the best. Dario, my "father," I

never would have gotten into salsa (at least not during the good years) if not for you. Take care of Jenny and take care of yourself. Soren, you have been and will be one of **thee** best friends that I will ever have. Separately, our sense of humor is strange, but together we are kind of scary. Maitri, you and Ruwanthi are great people with **huge** hearts. If you are a small fraction as good at being parents as you are at being people, then your children are incredibly lucky.

To the gang that I met at ultimate, I want to say that you were are all great people and I had a lot of fun with all of you. John, you are the ultimate game changer and a true friend. I have a feeling that, no matter what it is you will choose to do with your life, the world will be a better place because of it. Benny, Vanilli, I hope that you have found the happiness that you so richly deserve. Keep on dancing, my friend. One day we'll get the "group" back together. Tom, you appreciate things that a great many people hardly notice. Thanks for sharing them with me and I'll see you in Madison. Paco, the new keeper of the cones, you keep getting better and better. You are always ready to laugh, even at my jokes. Dominic, stop running so fast when I am guarding you. It has been a pleasure knowing you and keep the Faith. Ken and Andrea, it would be wrong for me to mention each of you separately because you are both better together. Good luck with your family and God Bless you. Jeff, Jodie, Juan, and Natanya, I wish all of you the best. All of you are proof of the incredible power of ultimate and people coming together. Dustin, Ziggy, Michelle, Mary, Jim, Andy, Ben, Melissa, Dom, and the rest (sorry), it has been fun.

To my friends on the fourth floor of Loomis, I also wish to extend to you my gratitude. Alex, if I ever had a problem, you were there to fix it. We had some good times in Germany. Good luck to you and Erin. There was never a more motivating workout partner in my life and I thank you for making me get up so early in the morning. Josh, I think I shared the strangest experience in my life with you in Poland. I would do it again in an instant. You're awesome. Paul, we came in together, and we are leaving, more or less, together. Good luck

to you and Judy out in Texas. Mike, you have a great voice and I wish you the best in the days to come. Your sense of humor is immense. Don't stop laughing, even if it's at me. Rebecca, the newest member of the HERMES experiment from Illinois, it was nice meeting you. Areg, you welcomed me into your home for all your celebrations and I always enjoyed talking with you. I also enjoyed your tea, it just tasted better when you made it. I wish the best for you, Giovanna, and your family. A special thanks to Penny for helping out with **everything** that would have given me an headache if I had to do it for myself.

I would like to thank Naomi for taking me as a graduate student. Her teaching is incredible and she was patient with me as I was learning my responsibilities, how to program, and all about hyperon polarization. Maybe sometime in the next decade I will be able to get that "Banana Phone" song out of my head. I would also like to extend my appreciation to Maurice. I asked him a lot of questions and he gave me a lot of answers. He always had a witty sense of humor and taught me more than he realizes. Also, to the other members of the HERMES experiment, I want to say thank you. To those people I bothered late at night on shift as I was learning my responsibilities, I apologize if I woke you.

To all the people with whom I have enjoyed working on the Physical Review with, I had a great time. Eric, Soren, Josh, and Martin, I am glad to have been a part of all the fun. Thanks for including me.

To my friends from dancing, I also want to say thank you for putting up with all my mistakes and my jokes. Victor, Chakri, Rebecca, Grazyna, Florin, Adrianna, Mary, Joscelyn, Erika, Lisa, Erica, Jennifer, Ibrahim, Roberto, Ben, and everyone else, you have been inspirational and fun to be during salsa. To all the people that I tap danced with, I had the time of my life. Performing at the Virginia was an incredible experience and the support that I received during the classes from all of you meant a lot to me. My life wouldn't be the same without the triple time step.

Other people that I choose not to categorize, but still deserve mention are Lisa, Annie,

Carmel, Evan, Andy, and whoever else it was that put up with me at various social gatherings. You are all a great group of people with a wonderful sense of humor and are very giving to those around you. Also, to all the team and participants of NFK 71 and to the FOCUS staff and fellow members of the Bible studies, I want to thank you for helping to inspire me in the days to come.

Finally, I would like to thank the members of my committee. Everything flew by so fast as I was preparing for the defense and completing my thesis, I really appreciate the sacrifice of time that all of you went through on such short notice to help me accomplish my goal of graduating. Also, I would like to thank those people who came out to see my defense and help me prepare for it.

Table of Contents

List of Tables ..... **xi**

List of Figures ..... **xiii**

Chapter 1 Introduction **1**

Chapter 2 The HERMES Experiment **6**
2.1 Introduction to HERMES 6
2.2 Important Properties of Particles in Matter 7
2.3 HERMES Spectrometer 10
2.3.1 The Front Spectrometer Section 10
2.3.2 The Mid Spectrometer Section 12
2.3.3 The Rear Spectrometer Section 13
2.4 HERMES Particle Identification (PID) 16
2.5 Triggers 16
2.6 Offline Data Productions 18

Chapter 3 Theory **24**
3.1 Structure, Distribution, and Fragmentation Functions... Oh My! 25
3.2 Constituent Quark Model 28
3.3 Lund Model of the Fragmentation Process 29
3.4 DGM Model of Hadron Polarization 30
3.5 Quark Recombination Model of Hadron Polarization 32
3.6 Anselmino Prediction for HERMES SIDIS Λ Polarization 34
3.7 Formula for Measuring the Λ Polarization 35

Chapter 4 Monte Carlo Studies **39**
4.1 GMC_LPOL – A Polarized Λ Generator 39
4.2 Λ Kinematics Study 41
4.3 Study of Top/Bottom Asymmetry 44
4.3.1 Effect of Polarization on Top/Bottom Asymmetry 48
4.3.2 Effect of Inefficiencies in the Spectrometer 49
4.3.3 Effects of Misalignment in the Spectrometer 51
4.4 Conclusions From Monte Carlo 54

Chapter 5 The Spin of the Λ at HERMES **64**
5.1 The Extraction of the Λ from the Data 64
5.1.1 Cuts Common to both Q^2 Regimes 65
5.1.2 Cuts Exclusive to the Photoproduction Regime 69
5.1.3 Cuts Exclusive to the SIDIS Regime 72
5.1.4 Brief Mention of the K^0_S and Related Cuts 72
5.2 Mass Peaks for Both Inclusive and Semi-inclusive Regions 73
5.3 Background Subtraction Procedure 77
5.4 The Final Results 78

Chapter 6 Conclusions **87**

Appendix A Further Details of the Λ Analysis **91**
A.1 Error Analysis 91
A.2 Burst List Mask Description 92
A.3 Vertex Cut Determination 93

Appendix B Maximum Likelihood Method **96**
B.1 Introduction to Maximum Likelihood 96
B.2 Strengths and Weaknesses of Maximum Likelihood 97
B.3 Maximum Likelihood in Λ Polarization 98
B.4 Acceptance Correction 101

Appendix C Tables for Monte Carlo and Data **103**

References **140**

Author's Biography **143**

List of Tables

4.1 Monte Carlo results from GMC_LPOL using the photoproduction (inclusive) option and defining the Λ polarization axes in the Λ CM frame. 42
4.2 Monte Carlo results from GMC_LPOL using the standard high Q^2 (semi-inclusive) option and defining the Λ polarization axes in the γ^*-proton CM frame. 42
4.3 Table of Monte Carlo results for an input Λ polarization of 0.90. In the case of the iterated formula, the cuts are slightly different, mainly cutting out low transverse momentum Λ particles. 49
4.4 Table of Monte Carlo results for an input Λ polarization of 0.10 and 0.90 with an inefficiency of 30% in the top half of the spectrometer. In the case of the 0.10 polarization, the iterative procedure has slightly different cuts, mainly cutting out low transverse momentum Λ particles. 50
4.5 Table of Monte Carlo results for an input Λ polarization of 0.10 and 0.20 with NO misalignments. 52
4.6 Table of Monte Carlo results for an input Λ polarization of 0.05, 0.10, and 0.20 with θ_x and θ_y misalignments. 53

B.1 Table of Maximum likelihood tests performed using a polarized Λ Monte Carlo generator. Trial 1 had 250,000 generated events (199,985 after a vertex separation cut); Trial 2 had 25,000 generated events (20,013 after a vertex separation cut); Trial 3 had 25,000 generated events (20,013 after a vertex separation cut); Trial 4 had 9,000 generated events (7194 after a vertex separation cut). 100

C.1 p_T distributions for long track MC for $P_\Lambda = 0.05$ 104
C.2 ζ distribution for long tracks $P_\Lambda = 0.05$ 105
C.3 p_T distributions for short track MC for $P_\Lambda = 0.05$ 106
C.4 ζ distribution for short tracks $P_\Lambda = 0.05$ 107
C.5 p_T distributions for long track MC for $P_\Lambda = 0.10$ 108
C.6 ζ distribution for long tracks $P_\Lambda = 0.10$ 109
C.7 p_T distributions for short track MC for $P_\Lambda = 0.10$ 110
C.8 ζ distribution for short tracks $P_\Lambda = 0.10$ 111
C.9 p_T distributions for long track MC for $P_\Lambda = 0.20$ 112
C.10 ζ distribution for long tracks $P_\Lambda = 0.20$ 113
C.11 p_T distributions for short track MC for $P_\Lambda = 0.20$ 114
C.12 ζ distribution for short tracks $P_\Lambda = 0.20$ 115

C.13 p_T distributions for long tracks in Λ photoproduction 116
C.14 ζ distribution for long tracks in Λ photoproduction 117
C.15 p_T distributions for short tracks in Λ photoproduction 118
C.16 ζ distribution for short tracks in Λ photoproduction 119
C.17 Total distribution for long tracks in Λ SIDIS 120
C.18 x_F distribution for long tracks in Λ SIDIS 121
C.19 p_T distributions for short tracks in Λ SIDIS 122
C.20 x_F distribution for short tracks in Λ SIDIS 123
C.21 p_T distributions for long tracks in $\bar{\Lambda}$ photoproduction 124
C.22 ζ distribution for long tracks in $\bar{\Lambda}$ photoproduction 125
C.23 p_T distributions for short tracks in $\bar{\Lambda}$ photoproduction 126
C.24 ζ distribution for short tracks in $\bar{\Lambda}$ photoproduction 127
C.25 p_T distributions for long track K^0_S in Photoproduction 128
C.26 ζ distribution for long track K^0_S in Photoproduction 129
C.27 p_T distributions for short track K^0_S in Photoproduction 130
C.28 ζ distribution for short track K^0_S in Photoproduction 131
C.29 p_T distributions for long track K^0_S in SIDIS 132
C.30 x_F distribution for long track K^0_S in SIDIS 133
C.31 p_T distributions for short track K^0_S in SIDIS 134
C.32 x_F distribution for short track K^0_S in SIDIS 135
C.33 p_T distributions for long track $\bar{K^0_S}$ in Photoproduction 136
C.34 ζ distribution for long track $\bar{K^0_S}$ in Photoproduction 137
C.35 p_T distributions for short track $\bar{K^0_S}$ in Photoproduction 138
C.36 ζ distribution for short track $\bar{K^0_S}$ in Photoproduction 139

List of Figures

1.1 Diagram of the $\Lambda \to p\pi^-$ decay. 3

2.1 A side view of the HERMES spectrometer. 9
2.2 Theoretical curves showing the Ĉerenkov angle vs. particle momentum for different hadrons. 15
2.3 Plot of PID3 against the TRD signal (PID5). The leftmost peak consists of positrons and the rightmost peak ($PID3 < 0$) consists of hadrons. 17
2.4 HERMES production chain 19
2.5 Example plots from the slow data quality program. a) HERA beam status, b) luminosity, c) longitudinal and transverse polarimeters, d) tracking efficiencies, e) trigger, calorimeter, and target status. 23

3.1 Feynman diagram of a simple deep-inelastic scattering experiment. 25
3.2 Proton incident on some target to create a Λ particle. Also shown are the spin, $\vec{S}$, and angular momentum, $\vec{L}$ of the diquark, (ud), and quark, s, referred to in the DGM model. 31
3.3 Prediction of the Λ polarization of $\gamma p \to \Lambda X$. Data points are taken from previous HERMES preliminary data and the solid line represents the fit to the data with the QMM model. Please see text for reference. 34
3.4 a) Transverse Λ polarization as a function of z_h averaged over the transverse Λ momentum. b) Transverse Λ polarization as a function of the transverse Λ momentum when averaged over the range $0.4 < z < 0.8$. Please see text for reference. 36

4.1 Comparison of a GMC_LPOL to GMC_DISNG for some sample kinematics. . 40
4.2 Monte Carlo plots of a) x_F vs. ζ and b) the "real" p_T vs the "photoproduction" p_Ti for $\zeta > 0.25$. The lower panel of each plot shows the standard deviation from the average value in each bin. Long tracks are represented in red and short tracks in blue. 43
4.3 Monte Carlo plots of a) x_F vs. the photoproduction p_T for $zeta < 0.25$ and b) x_F vs. the photoproduction p_T for $zeta < 0.25$. The lower panel of each plot shows the standard deviation from the average value in each bin. Long tracks are represented in red and short tracks in blue. 44
4.4 Plot of momentum vs. θ_x for proton long tracks in a) data and b) Monte Carlo. A momentum cut of 1.08 GeV $< M_\Lambda <$ 1.16 GeV was used. 46

4.5 Plot of momentum vs. θ_x for π^- tracks in a) data and b) Monte Carlo. A momentum cut of 1.08 GeV $< M_\Lambda <$ 1.16 GeV was used. The long tracks are shown in the top panel and the short tracks are shown in the bottom. 47
4.6 Monte Carlo Λ mass peaks with background fraction of 17%, a mass width of 0.0022 GeV. Λ polarization of 10%, and a background polarization of 15% for a) the top half of the spectrometer and b) the bottom half of the spectrometer. 48
4.7 Λ polarization versus ζ for long and short tracks in a large statistics set of Monte Carlo for an input polarization of 0.05 and comparing the iteration technique and the even weighting formula. 55
4.8 Λ polarization versus p_T in the region $\zeta < 0.25$ for long and short tracks in a large statistics set of Monte Carlo for an input polarization of 0.05 and comparing the iteration technique with the even weighting formula. 56
4.9 Λ polarization versus p_T in the region $\zeta > 0.25$ for long and short tracks in a large statistics set of Monte Carlo for an input polarization of 0.05 and comparing the iteration technique with the even weighting formula. 57
4.10 Λ polarization versus ζ for long and short tracks in a large statistics set of Monte Carlo for an input polarization of 0.10 and comparing the iteration technique and the even weighting formula. 58
4.11 Λ polarization versus p_T in the region $\zeta < 0.25$ for long and short tracks in a large statistics set of Monte Carlo for an input polarization of 0.10 and comparing the iteration technique with the even weighting formula. 59
4.12 Λ polarization versus p_T in the region $\zeta > 0.25$ for long and short tracks in a large statistics set of Monte Carlo for an input polarization of 0.10 and comparing the iteration technique with the even weighting formula. 60
4.13 Λ polarization versus ζ for long and short tracks in a large statistics set of Monte Carlo for an input polarization of 0.20 and comparing the iteration technique and the even weighting formula. 61
4.14 Λ polarization versus p_T in the region $\zeta < 0.25$ for long and short tracks in a large statistics set of Monte Carlo for an input polarization of 0.20 and comparing the iteration technique with the even weighting formula. 62
4.15 Λ polarization versus p_T in the region $\zeta > 0.25$ for long and short tracks in a large statistics set of Monte Carlo for an input polarization of 0.20 and comparing the iteration technique with the even weighting formula. 63

5.1 Figure (not shown to scale) depicting the various vertex and distances used in some of the cuts. 65
5.2 Gaussian plus second order polynomial fit to the Λ mass peak for a) the top and b) the bottom half of the spectrometer. The selected bin is $0 < \zeta < 0.25$ and $0.48 < p_T \leq 0.664$ GeV and these are short tracks only. 74
5.3 Gaussian plus second order polynomial fit to the K^0_S mass peak for a) the top and b) the bottom half of the spectrometer. The selected bin is $0 < \zeta < 0.25$ and $0.48 < p_T \leq 0.664$ GeV and these are short tracks only. 75

5.4 Gaussian plus second order polynomial fit to the $\bar{\Lambda}$ mass peak for a) the top and b) the bottom half of the spectrometer. The selected bin is $0.241 < \zeta < 0.32$ and $0.2 < p_T \leq 3.00$ GeV and these are long tracks only. 75
5.5 Gaussian plus second order polynomial fit to the $\bar{K^0_S}$ mass peak for a) the top and b) the bottom half of the spectrometer. The selected bin is $0.241 < \zeta < 0.32$ and $0.2 < p_T \leq 3.00$ GeV and these are long tracks only. 76
5.6 Gaussian plus second order polynomial fit to the Λ mass peak (SIDIS) for a) the top and b) the bottom half of the spectrometer. The selected bin is $0.0 < x_F < 1.00$ and $0.38 < p_T \leq 3.00$ GeV and these are long tracks only. . 76
5.7 Gaussian plus second order polynomial fit to the K^0_S mass peak (SIDIS)for a) the top and b) the bottom half of the spectrometer. The selected bin is $0.0 < x_F < 1.00$ and $0.38 < p_T \leq 3.00$ GeV and these are long tracks only. . 77
5.8 Sample a) first and b) second cosine moments versus the Λ mass minus the value of the peak Λ mass in each of the five bins mentioned in the text and the fit to the four side bins in the case of the inclusive Λ. Plotted in this fashion, the y-intercept gives the value of the background polarization The fit is for the kinematic region $0.25 < \zeta < 1$ and $x.xxx < p_T < x.xxx$, long tracks, and the top half of the spectrometer. 79
5.9 P_{Ks} and P_{MC} vs. a) ζ, b) p_T ($\zeta < 0.25$), and c)p_T ($\zeta > 0.25$). 80
5.10 $P_{\bar{K}s}$ and P_{MC} vs. a) ζ, b) p_T ($\zeta < 0.25$), and c)p_T ($\zeta > 0.25$). 81
5.11 P_Λ vs. a) ζ, b) p_T ($\zeta < 0.25$), and c)p_T ($\zeta > 0.25$) for long and short tracks. 82
5.12 P_Λ vs. a) ζ, b) p_T ($\zeta < 0.25$), and c)p_T ($\zeta > 0.25$) for both tracks together. 83
5.13 $P_{\bar{\Lambda}}$ vs. a) ζ, b) p_T ($\zeta < 0.25$), and c)p_T ($\zeta > 0.25$) for long and short tracks separately. 84
5.14 $P_{\bar{\Lambda}}$ vs. a) ζ, b) p_T ($\zeta < 0.25$), and c)p_T ($\zeta > 0.25$) for both long and short tracks. 85
5.15 P_Λ vs. a) x_F, b) p_T ($x_F > 0$) for both long and short tracks separately. . . . 86
5.16 P_Λ vs. a) x_F, b) p_T ($x_F > 0$) for both long and short tracks averaged together. 86

A.1 Mass peaks for a a) 10 cm and b) 25 cm vertex cut. The bin chosen for these peaks is in the text. 94
A.2 Λ Polarization vs. ζ for various vertex cut values. In a) we have long tracks only and in b) we have only short tracks. 94
A.3 Λ Polarization vs. p_T ($\zeta < 0.25$)for various vertex cut values. In a) we have long tracks only and in b) we have only short tracks. 95
A.4 Λ Polarization vs. p_T ($\zeta > 0.25$) for various vertex cut values. In a) we have long tracks only and in b) we have only short tracks. 95

Chapter 1

Introduction

"In the beginning, when God created the heavens and the earth, the earth was a formless wasteland, and darkness covered the abyss, while a mighty wind swept over the waters. Then God said, 'Let there be light,' and there was light." (Genesis 1:1-3) [1]

The story of how life began, the structure of the Universe, even something as seemingly simple as the structure of a tiny particle called a proton is an interesting one. Many scientists invest a great deal of time to solve these mysteries. However, sometimes new discoveries lead to even more puzzling questions.

Such was the case in 1976, when Bunce et al. collided an unpolarized proton beam on an unpolarized Beryllium target at 300 GeV and found that Λ hyperons produced in the collision emerges with a pronounced spin polarization. They measured a large (up to 40%) Λ polarization along the $\vec{p}_\Lambda \times \vec{p}_p$ axis where $\vec{p}_\Lambda$ and $\vec{p}_p$ are the momenta of the Λ and the proton, respectively. This polarization seemed to increase with the transverse Λ momentum, p_T [2].

Knowing that the polarization of a hadron is dependent on the interference between spin flip and non-spin flip amplitudes, this result was completely unexpected for two reasons. First, in high-energy scattering, there are many possible outcomes for particles in the final state. This makes it highly unlikely that there could be any significant coherence amongst

the spin dependent and independent amplitudes that would give rise to a noticeable polarization. Second, in perturbative QCD, there is no mechanism by which a spin flip amplitude can actually occur when the quarks are treated as essentially massless (an excellent approximation at high energies where such amplitudes are suppressed by $m_q/\sqrt{s}$, where m_q is the mass of the quark and $\sqrt{s}$ is the total energy of the colliding particles) [3].

The work of Bunce et al. continued onward. They analyzed Λ data taken at CERN for the purpose of normalization in a Σ^0 lifetime experiment [4]. This data involved lower energy beam (24 GeV) protons incident on platinum and showed no clear energy dependence of the Λ polarization on energy. This was again shown in 1978 [5] when higher energy (400 GeV) proton beams were again incident on a Beryllium target. This time around, it was also shown that the $\bar{\Lambda}$ had *no* significant polarization. At this time, it was hypothesized that this was an effect due to the suppression of any polarization from an $s\bar{s}$ pair (formed in the hyperon formation in the $\bar{\Lambda}$ case) by the polarization of $\bar{q}$ and $\bar{d}$ quarks whereas the u and d quark of the Λ (originated from a spin-0 singlet state from the incident proton beam) would have no effect on the Λ polarization.

Furthermore, Bunce et al. studied the effects of different targets on the induced Λ polarization [6]. This time, they used hydrogen, deuterium, and Beryllium targets at the Brookhaven AGS. The hydrogen target was a test as to whether or not there were any nuclear effects influencing the Λ polarization from their previous targets. Again, a similar polarization behavior was found as in previous experiments, but the polarization obtained from the hydrogen target was slightly greater, leading one to think that there are some nuclear effects involved wherein the Λ is rescattered in the target. Seeking to test the nuclear-effects theory further, they decided to look at the dependence of the Λ polarization on the atomic number of the target [7]. Here, they discovered that, indeed, the Λ polarization was lower in the case of the larger atomic numbers of the combined copper and lead data.

Other experimental groups also looked into this interesting puzzle of Λ polarization.

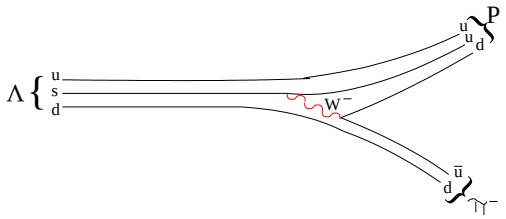

Figure 1.1: Diagram of the $\Lambda \to p\pi^-$ decay.

Lomanno et al. used a 28.5 GeV proton beam at Brookhaven National Laboratory incident on an iridium target [8]. The polarization they observed was similar to that of Bunce in the high-p_T range, but was higher in magnitude in the low p_T range. Also, Erhan et al. studied Λ polarization using the intersecting storage rings at CERN [9] with proton energies of 26.6 on 26.6 GeV and 31.4 on 31.4 GeV. Their results also showed a higher magnitude of polarization as well, but their error bars are also bigger.

Why is the Λ such an interesting particle to study? One reason is that it is the lightest hyperon (a baryon containing a strange quark) and so would be the easiest to produce. Second, and perhaps more importantly, is that it decays into a proton and a negative pion ($\Lambda \to p + \pi^-$) via a weak decay (see Figure 1.1). As the weak decay violates parity, the proton will be preferentially emitted in the same direction as the spin of the Λ. The equation describing the angular distribution of the protons from the $\Lambda \to p\pi^-$ decay (in the Λ center of mass frame) is:

$$\frac{dN}{d\Omega} = \left(\frac{dN}{d\Omega}\right)_0 \left(1 + \alpha P_n^\Lambda \cos(\theta_p, n)\right) \tag{1.1}$$

where $dN/d\Omega$ is the number of protons scattered into a solid angle $d\Omega$, $(dN/d\Omega)_0$ is the (isotropic) distribution of protons for an unpolarized sample of Λ hyperons, α is the weak decay constant equal to 0.642, P_n^Λ is the n^{th} component of the Λ polarization ($n = x, y, z$), and $\cos(\theta_p, n)$ is the angle of the proton momentum vector with respect to the n^{th} polarization axis. This formula can be shown to be the result of interference between s and p wave states. The derivation can be found in some textbooks, such as [10].

All in all, there are some general features of induced Λ polarization that are seen by

everyone in these experiments. For good review articles written by Heller, see [11] and [3]; also there are reviews written by J. Soffer [12] and J. Félix [13] which provide good theoretical insight. These common features are [11]:

- The Λ polarization points along a direction ($\vec{n} = \vec{p}_{beam} \times \vec{p}_{\Lambda}$) perpendicular to the production plane.
- The Λ polarization is independent of the energy of the reaction (at least from 10-2000 GeV).
- The magnitude of the Λ polarization is linear in the Λ transverse momentum, p_T, up to about 1 GeV, where it reaches a constant value. For protons incident on a nuclear target, this polarization is negative.
- The magnitude of the Λ polarization is linear in x_F, a variable called "Feynman-x", which is a measure of the "forwardness" of a produced particle's momentum. This variable will be covered in slightly more detail Chapter 3.

Two types of reactions will be studied in this thesis: inclusive and semi-inclusive Λ production using an electron beam. In the inclusive reaction, $e + p \rightarrow \Lambda + X$, only the Λ particle is measured in the final state. The Λ is not directly measured, but is reconstructed from its decay products, a proton, p, and a negative pion, π^-. The X represents everything else produced in the reaction which is unobserved. In the semi-inclusive reaction, $e + p \rightarrow e' + \Lambda + X$, the scattered lepton is also measured along with the Λ. The inclusion of the scattered lepton will enable the measurement of q, the four-vector describing the energy and momentum transfer from the electron beam to the target, i. e. $q = k - k'$, where k and k' are energy-momentum four vectors of the incident and scattered beam respectively. The importance of the q 4-vector and its relationship to the aforementioned x_F variable will be covered in more detail in Chapter 3.

A Λ is produced via the strong interaction. As such, its production must obey parity conservation and so its spin-polarization must lie along a pseudo-vector direction. In an inclusive reaction, there are only two vectors to choose from which to construct the pseudo-vector of the Λ spin polarization: the momentum of the Λ, $\vec{p}_\Lambda$, and the momentum direction of the lepton beam, $\hat{k}$, such that

$$\hat{n}_{incl} = \frac{\hat{k} \times \vec{p}_\Lambda}{|\hat{k} \times \vec{p}_\Lambda|}. \tag{1.2}$$

Thus, the polarization of the Λ is in a direction perpendicular, i. e. transverse, to the Λ production plane. In a deep inelastic, semi-inclusive reaction (SIDIS), there is no unique choice of axis, but it is still thought, in accordance with the experiments mentioned earlier, that the polarization vector should be perpendicular to the production plane. As such, the vector $\hat{k}$ in Eqn. 1.2 will be replaced with the more accurate $\vec{q}$ (in the sense that the virtual photon is the actual incident particle upon the proton target), the vector component of the 4-vector q.

This thesis will explore Λ polarization in detail in both the inclusive and semi-inclusive regimes. In Chapter 2, the HERMES spectrometer will be discussed. This will include some discussion of the properties of particles and their interactions as well as an examination of the HERMES offline data production. Then, in Chapter 3, a general view of some of the more common theories of hyperon polarization will be discussed as well as more detail about the analysis techniques by which the polarization ca nbe extracted from the data. This will be followed in Chapter 4 by a close look at different studies on the Λ kinematics and polarization in Monte Carlo for various situations. The results from the actual data set will then be presented in Chapter 5, including a list of cuts placed on the data and a step-by-step walkthrough of how the results are obtained. Finally, in the last chapter, some final comments and conclusions will be presented.

Chapter 2

The HERMES Experiment

2.1 Introduction to HERMES

The HERMES experiment is situated in the East Hall at the DESY (Deustches Electronen SYnchotron), located in Hamburg, Germany. HERMES uses the positrons (or electrons) from the smaller PETRA accelerator ring that are injected into the larger HERA ring (6.335 km circumference) that circulates through the East Hall. The energy of these leptons is typically 27.6 GeV with currents starting at around 40 mA at peak operating conditions and decaying down to about 15 GeV over the course of a typical 10 hour fill. There are currently three experiments that use the HERA ring at DESY: HERMES, ZEUS, and H1. Of these, only HERMES has an interest solely in the lepton beam, with the accompanying proton beam sometimes a hindrance due to high background levels caused by poor tuning and, consequently, drifting proton beams. Also, due to the Sokolov-Ternov effect, the leptons are automatically polarized transversely to the beam direction due to their circular orbit. HERMES has a series of magnets to orient the lepton spins longitudinal to their momentum and to reorient them to their transverse orientation after our experimental area. The lepton-beam polarization is an important component of many parts of the HERMES physics program, but is not used in the analysis presented here.

Something should be said about the polarimeters for the positron beam, however. There are two polarimeters on the HERA ring, the Transverse POLarimeter (TPOL) and the Longitudinal POLarimeter (LPOL). The TPOL is used by all the experiments on the HERA ring and is used to measure the transverse polarization of the positron spin due to the self-polarizing Sokolov Ternov effect. The LPOL is a HERMES polarimeter used to measure the polarization in the HERMES spectrometer region (where the beam has been aligned longitudinally by the aformentioned spin rotators). For the LPOL, a laser is incident on the positron beam and the backscattered compton photon is incident on the calorimeter of the LPOL. The asymmetry between right and left circularly polarized lasers along with the differences in energy distributions from the left and right circularly polarized light are used to determine the polarization of the positron beam [14][15]. The TPOL also uses an asymmetry measurement, but is dependent on both circularly polarized and linearly polarized terms and on spatial distributions of the scattered photon in its calorimeter [15]. The values obtained by the TPOL and the LPOL should be the same, but the LPOL measurement is preferred when it is operational.

This chapter will focus on the HERMES spectrometer as well as some of the details of my own responsibilities to the experiment. However, first a brief description of particle properties will be given to better understand how different types of particles are differentiated from each other in the experiment.

2.2 Important Properties of Particles in Matter

The particle-identification scheme at HERMES takes advantage of the different interactions of different particles in matter. The main processes by which particles lose energy in matter are through inelastic collisions with atomic electrons, elastic collisions with nuclei, brehmstrahlung, and Ĉerenkov radiation [16].

In brehmsstrahlung, charged particles of low mass, such as positrons and electrons, radi-

ate when decelerated (or accelerated) due to the the presence of the electromagnetic fields of nuclei. At low energies, it has a small effect on the incoming particle, but energies greater than around 40-50 MeV, the effect is seen to increase quite rapidly (although the fractional energy loss in this region is relatively constant to constant as energies increase beyond 1 GeV).

Ĉerenkov radiation occurs when a particle moves faster than the speed of light in some medium. Thus, this happens when

$$v > \frac{c}{n} \tag{2.1}$$

where n is the index of refraction of the medium. In this case, a conical "shock wave" forms behind the particle radiating photons in a cone of angle θ_c relative to the particle's trajectory such that

$$\cos\theta_c = \frac{1}{\beta n} \tag{2.2}$$

where $\beta \equiv v/c$.

There is a marked difference in the behavior in matter of light, charged particles (electrons and positrons) and the much heavier hadrons (of which, the pion, the lightest of all the hadrons, is 300 times more massive than the electron). At low energies, most of the energy lost by electrons and positrons is due to electron collision, but, as mentioned earlier, at higher energies of around a half a GeV, brehmsstrahlung becomes the dominant mechanism of energy loss. The radiation length of an electron for a material "...is defined as the distance over which the electron energy is reduced by a factor of 1/e due to radiation loss only" (pg. 41 of [16]). Thus, materials with a shorter radiation length will stop electrons quicker than a material with a long radiation length (compare 30050 cm in air to 0.56 cm in Pb (pg. 42 of [16])).

In contrast, for hadrons, most of the energy loss comes from low energy collisions with atomic electrons. As a hadron gains energy, it will spend less time interacting with these

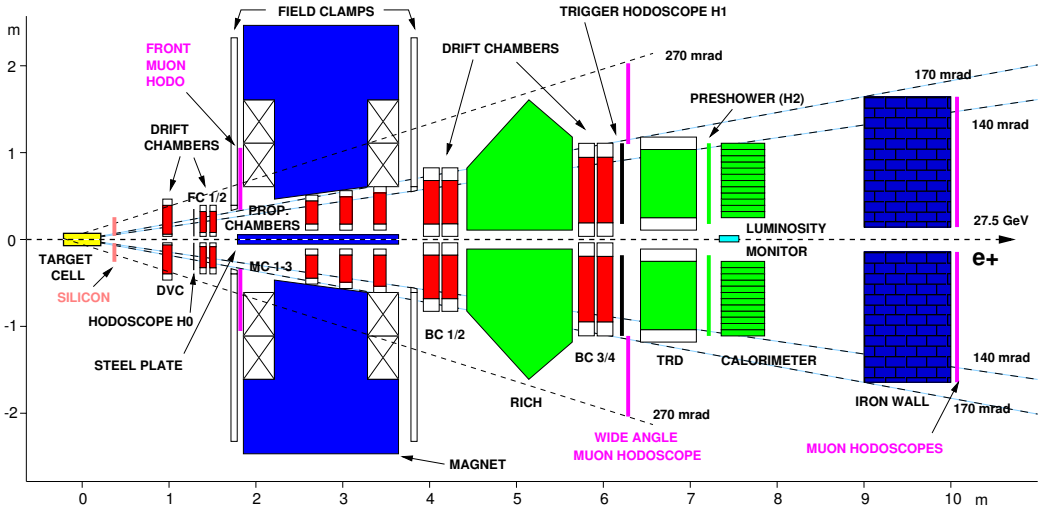

Figure 2.1: A side view of the HERMES spectrometer.

electrons and this results in a decreasing energy loss until the lowest amount of energy a heavy particle can lose is reached and the particle is referred to as being minimum ionizing. The energy that the hadron has at this point is referred to as its minimum ionization energy. For energies less than this minimum ionizing energy, different heavy particles have different energy curves which can be used for particle identification. Above the minimum ionization energy, the energy loss is roughly constant. Thus, heavy ions passing through matter will not show a rapid energy loss until traveling a certain amount of distance through the material, i. e. until they slow down enough to drop below the minimum ionizing energy. This is useful in medical applications wherein it would be desirable to destroy tumorous cells, but not any of the surrounding healthy tissue. All these details of particle properties have been taken from reference [16] and more details can be found there.

These properties come mainly into play when we discuss the rear of the spectrometer. It is there that we have most of the particle identification detectors and the differences in lepton/hadron behavior in matter are of great importance.

2.3 HERMES Spectrometer

The HERMES spectrometer, seen in Figure 2.1, is a forward going spectrometer with an angular acceptance of ± 170 mrad in the horizontal direction and $+(-)40$ to $+(-)140$ mrad in the vertical direction. It is separated into top and bottom halves by iron plates above and below the beam line . These plates are used to limit the effects of any magnetic fields from our experiment on the lepton and proton beams since they are shared by the other experiments. Aside from top and bottom, the spectrometer can be split into essentially three regions: the front section, the middle (or magnet) section, and the rear section. Each of these sections will be described briefly in what follows [17][18].

2.3.1 The Front Spectrometer Section

The front section of the HERMES spectrometer consists of the target cell, two front chambers (FCs), a drift vertex chamber (DVC), and a hodoscope. In the past, there were also two vertex chambers (VCs), but they are no longer in use. These detectors have essentially one main purpose, that is to provide the front tracking (before the spectrometer) information for each particle that passes through the spectrometer acceptance. Knowing this, we can obtain the initial momentum direction of the particle, i. e. the momentum direction before passing through the spectrometer magnet.

The target cell used at HERMES is a t-shaped tube with an elliptical cross section with its long axis along the beam direction. At HERMES, we use a gas target, which has the advantage of a higher purity and easier switching of the polarization state of the target as compared to a solid target. Gas can be unpolarized or (longitudinally or transversely) polarized and is fed to the cell from the Atomic Beam Source (ABS). The ABS takes advantage of the hyperfine splitting of atoms to separate different spin states and the desired spin states are focused using sextupole magnets. To reduce any synchrotron radiation damage to the target cell, both vertical and horizontal collimators are placed upstream of the target cell.

There are 2 FC modules, each consisting of 2 sets of 3 planes of wires (denoted as U, V, and X). The X-plane is completely vertical, with the U and V planes at angles of 30 degrees with respect to the vertical. This gives higher sensitivity to left/right measurements than up/down, but is advantageous since all rear wire chambers have a similar design and the left/right bend of the tracks due to the magnet gives us the particle's momentum. The other set of wire planes (U', V', and X') are shifted by half a cell to resolve any left/right ambiguities. The wires are alternating anode and cathode wires between cathode foils in a gas environment. Electrons in the gas are excited by incoming charged particles and are accelerated toward the anode (sense) wires. This causes an avalanche (either by direct collision from a hard process or when emitting a photon in a soft process) of more electron excitations that give a measurable signal in the sense wire. The DVC operates in a similar fashion as the FC, but is slightly smaller in size.

The VCs are no longer in use due to damage, but, when they were active (1996-1997), provided more accurate tracking than the drift chambers. Each VC module consisted of 3 planes of Micro Strip Gas Counters (MSGCs). In a particular cell of the MSGC, there was a cathode plane separated from a sheet of glass with anode and cathode strips. Within this gap of about 3 mm was a gas that would be ionized by an incoming particle, similar to what happens in the FC, above. The collected charge signal at the anode gives an indication of the particle's position when passing through the VC. Also, so as not to affect the electric field of the drift cell too significantly, the glass substrate on which these strips were grown had enough surface conductivity to get rid of any excess charge falling on the surface from the gas multiplication process.

Finally, the luminosity monitor is used to determine the rate at which the beam leptons are incident on an effective surface area of target nucleons, i. e.

$$LUMI \;=\; \left(\frac{no.targetnucleons}{area}\right) * \left(\frac{no.ofbeamelectrons}{sec}\right).$$

To do this, the interaction between the beam leptons with the atomic electrons of the target

gas is used. The lumi monitor has two calorimeters consisting of 12 $NaBi(W0_4)_2$ blocks on either side of the lepton beam that are used to record these leptonic interactions. When the incident lepton is a positron, this interaction is referred to as Bhabha scattering, $e^+ + e^- \rightarrow e^+ + e^-$, and when the incident lepton is an electron, the interaction is referred to as Møller scattering, $e^- + e^- \rightarrow e^- + e^-$. These interaction cross sections are known very precisely from QED. By ensuring that there is a minimum energy deposition of 5 GeV in both the left and the right calorimeter blocks (due to the symmetry of the interaction), background events are mostly excluded from the total luminosity rate recorded.

2.3.2 The Mid Spectrometer Section

The middle section of the spectrometer consists of the magnet and 3 Magnet Chambers (MCs). The magnet helps in the determination of the momentum of a particle. A charged particle moving in a magnetic field experiences a force proportional to the charge of the particle (q), the magnitude of the momentum (p), and the magnitude of the magnetic field (B). Assuming that the directions of the magnetic field and velocity are initially 90 degrees apart from each other (and that the magnetic field direction is constant), one can derive the radius of curvature of the particle, r, from Newton's second law and the fact that we have a centripetal acceleration

$$r = \frac{p}{qB}. \tag{2.3}$$

The magnet itself was designed to have a deflection power of $\int B \cdot \ell = 1.5$ T·M, but usually only 1.3 T·M are used to conserve power. Correction magnets are also used to help minimize the effect of the magnet on the lepton and proton beams and to reduce the fringe field in other parts of the spectrometer. The overall fringe field near the closest tracking detectors is less than 0.1 T, which should be weak enough at the FC so as not to affect its performance.

The three magnet chambers (MCs) are useful for tracking very low momentum particles, i. e. those particles whose radius of curvature in the magnet does not allow them to extend in the rear section of the spectrometer. These tracks are referred to as "short" tracks. Unfortunately, there is no way of doing particle identification on these tracks (as there are no PID detectors in the front region), but for certain particles, such as the Λ, the particle mass peak is well defined and enables a cut on some of these short tracks. This will be covered in detail later on in Chapter 5. Each MC consists of three submodules (X, U, V), each of which has two cathode planes and an anode plane. These modules are all located in the same gas volume.

2.3.3 The Rear Spectrometer Section

The rear section of the spectrometer has two purposes: complete the tracking of the particle to complete the momentum calculation and particle identification. The tracking is done by four back chambers (BCs). Each is composed of six wire planes and is very similar in form and function to the front chambers.

The hodoscopes (H0, H1, H2) arrays are vertically oriented scintillating panels attached to photomultiplier tubes. They provide fast signals for triggering and the rear hodoscope in the spectrometer (H2, also called the the "preshower") assists in particle identification. The particle identification is accomplished with the help of 11 mm of Pb in between two 1.3 mm steel plates which is placed in front of H2 to serve as a radiator. A heavy particle wil not deposit much of its energy passing through this thin layer of Pb, but a light particle such as a positron or electron will immediately start a electromagnetic shower upon contact with the Pb, causing more than one minimum ionizing particle to be recorded by the hodoscope paddles. This signal is yet another way to differentiate between leptons and hadrons. For a description of the triggering, please see Section 2.5.

Another useful device for hadron and lepton separation is the Transition Radiation Detec-

tor (TRD). Transition radiation is radiation emitted by an ultra-relativistic particle when it passes through matter. Thus, only a lepton is expected to transition radiate. Each TRD module (there are six each for the top and bottom of the spectrometer) has two sections. The first, called the radiator, consists of muliple fibers packed together through which a lepton will transition radiate. The second is a proportional chamber that will collect a charge signal from the emitted transition radiation. The signal from a single TRD module is not sufficient to separate pions from leptons. However, by doing a truncated average of all six modules (dropping out the module with the highest number of counts and taking the average of the remaining modules to help eliminate certain types of rare lepton events that resemble hadron events) a sufficient pion rejection is seen where the pion rejection is taken to be the ratio of actual pions to misidentified leptons that were really pions.

The calorimeter, placed at the rear of the spectrometer, is composed of 420 lead-glass blocks for each half (top/bottom) of the spectrometer. Behind these blocks is an array of photomultiplier tubes, one for each block. For a positron, the electromagnetic shower inside of lead-glass block is expected to starts relatively early (compared to a heavier particle), and as the 0.5 m depth of the blocks corresponds to 18 radiation lengths, the positron will end up depositing essentially all of its energy inside the spectrometer. In measuring the total energy deposited by the particle in the calorimeter divided by the momentum of the particle, one should have a ratio close to unity for a light particle such as an electron or positron. To prevent beam damage to the calorimeter during beam injection, the calorimeter is moved away from the beam until after the beam optics are tuned.

Once one has identified a particle as an electron or a hadron, one can then use the Ring Imaging CHerenkov (RICH) detector to determine what type of hadron it is [19]. This particular detector takes advantage of the fact that lighter particles emit Ĉerenkov radiation at lower momentum than heavier particles, as seen in Figure 2.2. The RICH consists of a heavy gas (C_4F_10), an aerogel surface directly behind the entrance window, a spherical

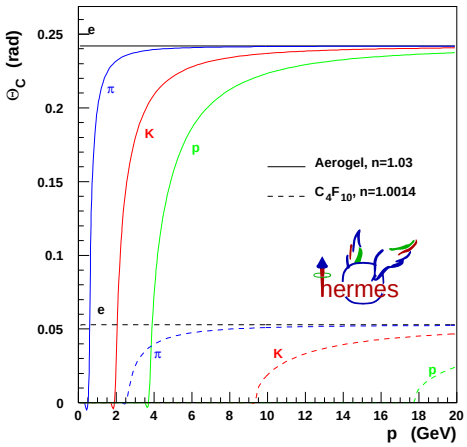

Figure 2.2: Theoretical curves showing the Ĉerenkov angle vs. particle momentum for different hadrons.

mirror, and an array of 1934 phototubes per spectrometer half. After a particle emits Ĉerenkov radiation, this light is reflected towards the phototubes such that a ring is formed, the ring being representative of the opening angle of the Ĉerenkov cone (Eqn. 2.2). The resultant particle ID can discriminate between pions, kaons, and protons over the momentum range 2–20 GeV. Before 1998, there was no RICH detector in the HERMES spectrometer and a Ĉerenkov detector was used. It operated on a similar principle as the RICH, with a single unit in the top and the bottom consisting of a radiator (a mixture of nitrogen and C_4F_10) and an array of 20 spherical mirrors to focus the Ĉerenkov radiated light onto photomultipliers. This old detector lacks the flexibility in momentum ranges achieved by using the two types of radiators in the RICH (again, see Figure 2.2) and is basically used as a pion rejector. Finally, the *rqp* value given by the RICH is a measure of how certain the hadron identification is, i. e.

$$rqp \quad = \quad \log_{10} \frac{Prob(h_1)}{Prob(h_2)} \tag{2.4}$$

where h_1 is the hadron species producing the maximum probability in the RICH and h_2 is the hadron species producing the second highest probability in the RICH. The ratio of these two probabilities will be greater when the the certainty of the identification of h_1 is large.

2.4 HERMES Particle Identification (PID)

The HERMES particle identification (PID) system is used to differentiate between hadrons and leptons (using the calorimeter, preshower, and TRD) and between different hadron types (using the RICH). To perform the lepton/hadron separation, quantities called "PIDx" are calculated which combine the responses of "x" PID detectors to each reconstructed track and provide a probabilistic measure of the particle's identity. For instance, in the year 1995 (pre-RICH), PID4 would be written as:

$$PID4 \;=\; \log_{10} \frac{P^e_{cal} P^e_{pre} P^e_{cer} P^e_{trd}}{P^h_{cal} P^h_{pre} P^h_{cer} P^h_{trd}} \tag{2.5}$$

where each P^i_{det} is the probability that the particle $i = e, h$ would have produced the measured response in the detector $det = cal, pre, cer, trd$ (the detectors being the calorimeter, the preshower, Ĉerenkov, and the transition radiation detector,respectively), given the track's measured momentum. The corresponding formula for PID3 is the same without the TRD involved and for PID2 is the same without the TRD and the Ĉerenkov. PID5 is just the PID from the TRD only. Notice that the expression for the PID is a log expression. Thus, if the probability of a particle being a lepton is greater than the probability of it being a hadron, the ratio of probabilities in eqn. 2.5 will be greater than one, meaning that the log of the ratio will be *positive*. However, if the particle is more likely to be a hadron than a lepton, the ratio will be less than one and the log of the ratio will be negative. This is a very efficient method of PID that, in the 1995 data taking year, produced an efficiency of 97% using the PID3+TRD formalism. For a comparison of the different pid schemes for the year 1995, see Figure 2.3, noticing the separation of the hadrons and leptons in each case.

2.5 Triggers

The trigger system used at HERMES provides a fast signal to the online computing software to record an event from the electronics. This is used to help cut background in the raw,

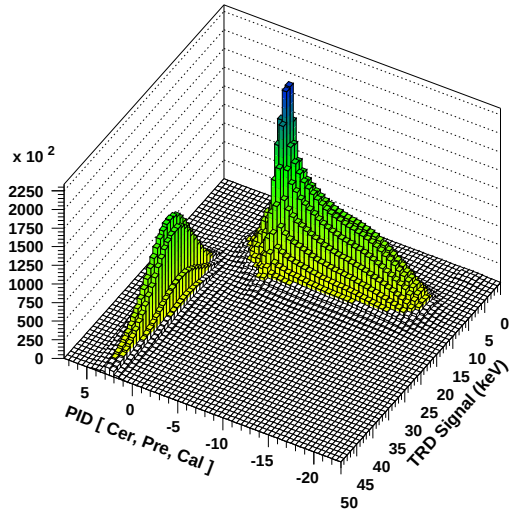

Figure 2.3: Plot of PID3 against the TRD signal (PID5). The leftmost peak consists of positrons and the rightmost peak ($PID3 < 0$) consists of hadrons.

recorded data (which helps save disk space). There is the capacity for up to four levels of triggers within the HERMES online system, however, only one level is generally needed. This first level trigger is the focus of this section. This is the trigger that operates on the smallest time-scale, approximately 400 ns. This time scale includes the time it takes for the trigger to be logically analyzed (about 150 ns) and the time it takes for the signal to reach the electronics trailer (about 250 ns).

The first level trigger involves the hodoscopes, the back chambers, and the calorimeters. The calorimeter has two threshold values, below which events are not accepted. For polarized running, the threshold is 1.4 GeV and for high-density, unpolarized running the threshold is set at 3.5 GeV for the positron. This calorimeter signal must occur at the same time as the hera clock signal (which is also taken as the time stamp for the event). The deep inelastic scattering trigger (trigger 21) also requires that the positron pass through all three of the hodoscopes. For the photoproduction trigger, it is required that there are hits in the both the top and bottom detectors of the spectrometer, using all three of the hodoscopes and the back chambers. This trigger also uses the HERA clock signal. For the photoproduction trigger, there are no requirements on the positrons since most of the positrons in photoproduction

go along the beam pipe and are not seen by the spectrometer.

2.6 Offline Data Productions

My responsibility for the experiment involved software, specifically the offline slow control production. The offline data production involves preparing of accumulated data for a period of running (usually by year) such that it is in a useful form for analysis. This production has three parts, the main production, the slow control production, and the uDST (micro Data Summary Tape) production. Figure 2.4 provides a detailed schematic diagram of the production chain. The data productions are labeled with the year, a letter indicating the main production version, and a number for the uDST production version. The "a" production includes the raw data taken on shift along with calibrations taken from the previous year of data. The first version available for analysis is always a "b" production (for older data sets, later productions versions are available which include improvements that were made in more recent years and so the "b" production is obsolete). The "b" productions include detector calibrations based on the "a" productions. These calibrations are supplied in the form of "expert files" by the different detector groups at HERMES. New productions (main, slow, and uDST) are necessary when a new tracking method is introduced. An example of a production label would be 00d0, which means that it is for the year 2000 and is the first uDST version of the "d" production.

The data acquisition system (DAQ for short) is the online computer system responsible for managing the vast amounts of data obtained by the HERMES experiment. It is the responsibility of the DAQ to record the information to disk for each "good" event (good events decided by the trigger). Events are grouped into 10 second long "bursts," whose purpose is to provide a time scale for the slow control recording. This information is then grouped into runs, which is set of events comprising about 450 MB of storage. These runs are part of the fills defined by the lifetime of the positron beam. These runs are backed up

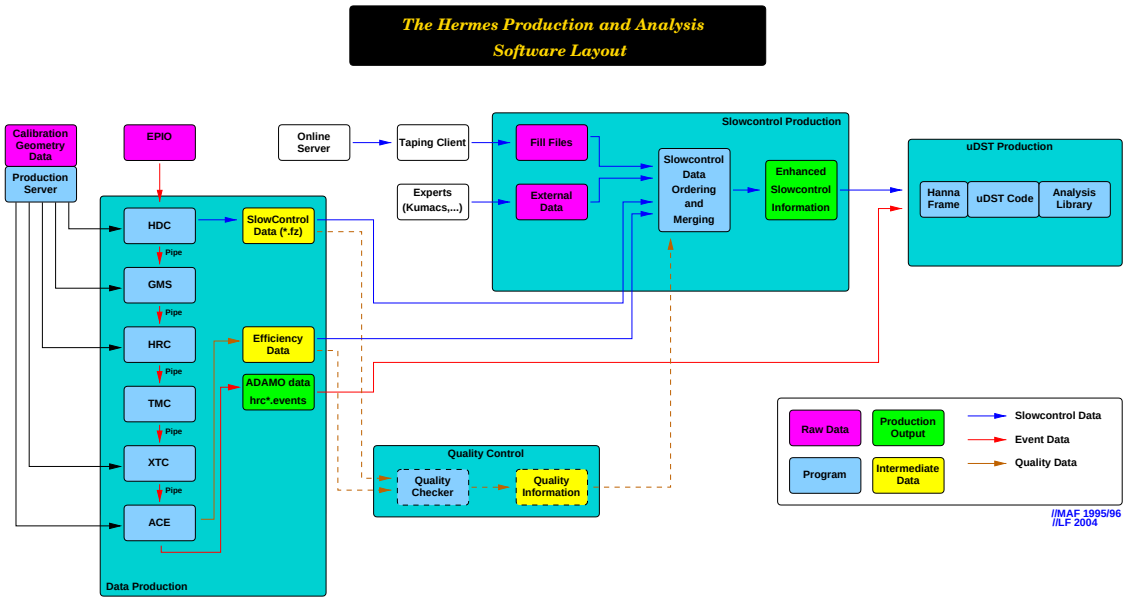

Figure 2.4: HERMES production chain

on disk in the East Hall and also, along with the fill files, are copied to the tape robot at DESY.

The main production mostly involves the HERMES DeCoder (HDC) and the HERMES Reconstruction Code (HRC). HDC takes the raw signals from the hardware components of the HERMES spectrometer. These signals (analog or timing) are identified by channel number and are converted (via calibration, mapping, and geometry) into actual energy signals and signal times as well as spatial positions of these "hits" in the HERMES spectrometer. HRC takes these "hits" and arranges them into straight line tracks in the front and the back of the spectrometer separately by using a simple tree search algorithm. These front and back "partial" tracks are then compared to see if they match up in the middle of the spectrometer magnet. The angular deflection of the front track is then used to determine the particle's momentum. HRC is also responsible for identifying 3×3 block "clusters" of hits in the calorimeter, and computing their location by taking an energy-weighted average of the central positions of each block involved.

and converts them to quantities with physical meaning, i. e. "I hit this wire in the Front Chamber" and "I deposited this much energy in the calorimeter." The HRC takes the spatial

information and tries to determine a particle track through the spectrometer.

The slow control production is named for the fact that the online slow control monitors things that change slowly, and therefore can be measured at a much slower rate than the event trigger rate (about 500 events per second). Such things as temperature, voltage settings for photomultipliers, mirror positions for the longitudinal polarimeter, pressure, etc. are measured by the online slow control software. The slow control information is of two types: data needed for analysis (e. g. luminosity and target polarization) and data indicating the operational status of a detector.

There are three basic inputs to the offline slow control production. These are the raw, unprocessed "fill files" recorded by the online slow software, some text files for each run from the HRC production, and external files from some of the detector experts. The raw slow files basically contain the information listed above and form the backbone of the final, offline slow file.

The files acquired from HRC need to be built into tables, filtered, and sorted. Hardware and software efficiencies files from the ACE (Alignment Calibration and Efficiencies) code, part of the main production, have an excess of information (i. e. some of which no one will use), and so they require filtering to produce smaller files. Also information about the calorimeter threshold and trigger prescale values comes in the form of text files output from the main production. All of this must be included in the final, processed slow file.

Finally, there is the information received from the detector experts. The external files include information about the following:

- luminosity monitor – gain corrected luminosity values and burst by burst fits of the lumi rate.
- longitudinal polarimeter – fits to the polarization per burst.
- transverse polarimeter – corrected polarization value for each burst and smoothed fits to the polarization per burst.

- tracking efficiencies – computed per run, per burst, and per separate target spin states within a burst (when the target spin state changes within a 10 second burst, so called "split bursts" of shorter length are generated).

- target gas information – implemented recently to keep track of which type of gas bottle was connected to which of the four gas stations.

Even if a new data production is requested for a year (and such things as tracking are the same, but maybe there are new target expert files), the slow control might not have to be re-run and only the uDST production may require redoing. Unfortunately, the luminosity burst-by-burst fit is relatively new since the 2000 production. It was then done for all previous years of data production as well. This required some alteration of codes due to the reorganization of the HERMES computer scheme circa the year 2000. In addition, new tracking methods were also implemented in the various main productions that required new tracking efficiencies to be determined. Fortunately, the production is now sufficiently automated to the point where it should be easy to re-run any previous slow productions from 1996 to the present.

The uDST production involves combining the information from the main and the slow control productions along with further "expert files" such as PID information and target information and makes data tables of the smallest possible size to be used by analysers. The uDST production also includes all PID calculations. These tables are time-organized and represent the final product of all the hard work put in by the production and detector groups. The final uDST files are examined by a HERMES subgroup referred to as the datacops. The datacops provide two services. First, they examine a series of plots to look for gaps in data for a production and that these gaps are accounted for. Second, they provide a burstlist indicating the data quality, good or bad, for each burst of data.

Aside from the normal running of the offline slow control, a slow production data-quality code was instituted by Illinois post-doc Maurice Bouwhuis and myself. This was created so

that we could check for missing information in the slowfills and resolve the problem before the uDST production was started. In principle, this would pinpoint a problem before the datacops started to examine the uDST. Thus, it would prevent loss from having to re-do the uDST production due to a problem with the slow control, which takes much less time to complete (although with the new HERMES computing environment mentioned earlier, all the productions run much faster than before so that re-running a production is not as inconvenient as it once was).

The main component of the slow data quality is the program called READSLOW. This program takes an input text file containing the names of all the variables one wishes to measure and the tables in which they are located in (within a processed slow control file) and then creates an ntuple, a type of data file read into PAW (Physics Analysis Workstation). The time stamp assigned to each ntuple record is taken from the "daqBasic" table, where daq refers to Data AQuisition, the backbone of the online software. Feeding this ntuple into PAW, one could then obtain plots of the chosen variables. These plots are constructed versus the respective time from the start of the fill, which made them a little more detailed than the plots generated by the datacops, which are done on a per run basis. As such, there were times when some missing information had been spotted, reported to the detector responsible, and corrected before the slow control was sent off to the uDST production. It also served to indicate if some problem seen in the uDST production originated in the slow control when such problems were identified by the datacops. Some examples of the types of plots created for a fill can be seen in Figure 2.5.

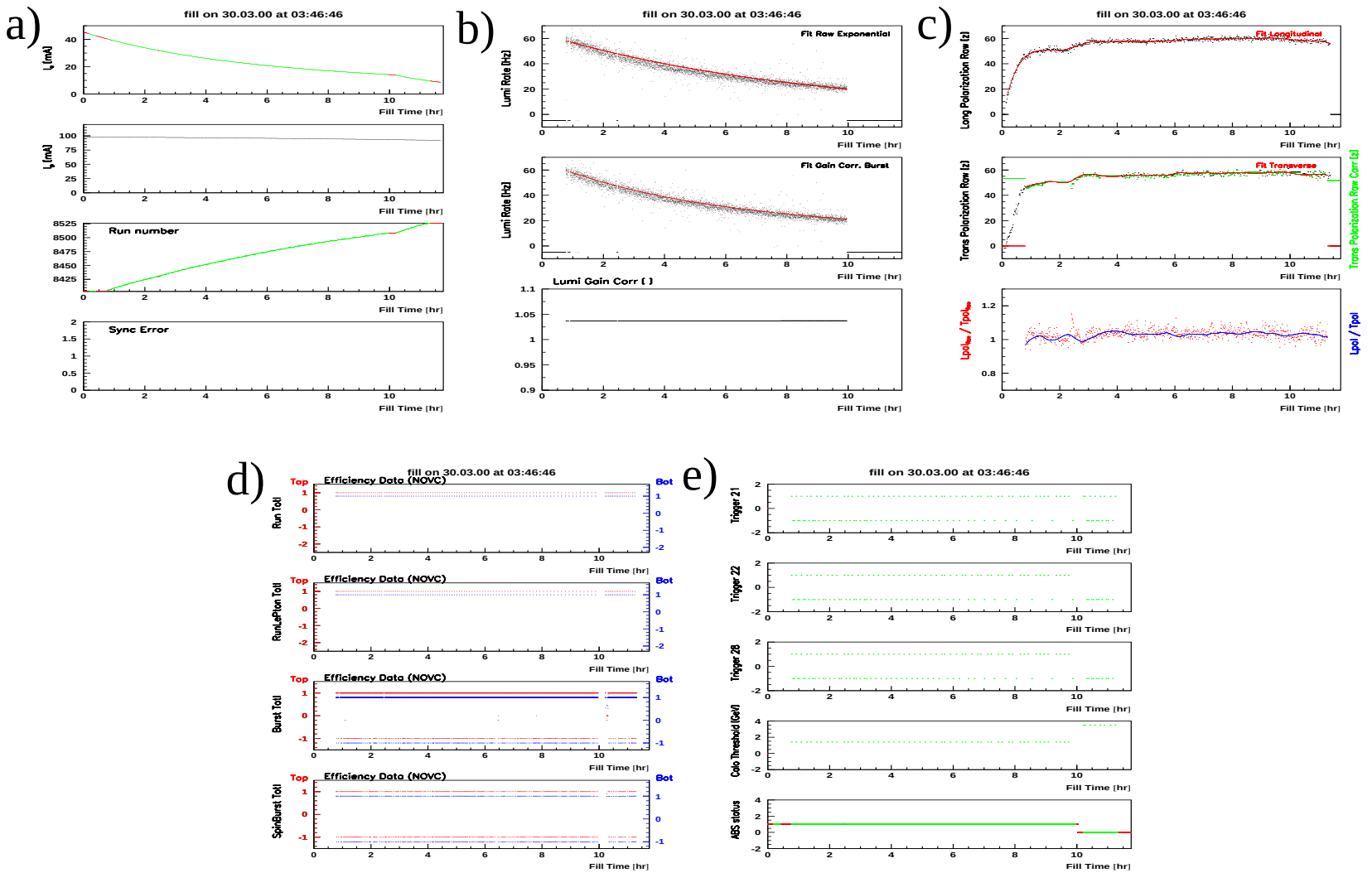

Figure 2.5: Example plots from the slow data quality program. a) HERA beam status, b) luminosity, c) longitudinal and transverse polarimeters, d) tracking efficiencies, e) trigger, calorimeter, and target status.

Chapter 3

Theory

An electron is an example of a fundamental particle as it cannot, to current knowledge, be broken down into anything simpler. A proton, on the other hand, is composed of smaller constituents called quarks. It is part of a large family of quark bound states referred to as hadrons. More specifically, the proton is a baryon: a hadrons with three quarks. Another subset of hadrons are the mesons, particles composed of a quark and an antiquark.

This picture is a little simplistic, however. For example, protons are generally seen as composed of two up quarks and one down quark. These quarks are known as "valence" quarks and determine the proton's quantum numbers. However, the proton also contains "sea" quarks. These come in quark-antiquark pairs and, as their name suggests, form a kind of "sea" about the valence quarks. Gluons, the carriers of the strong force, are also present in abundance. Although many properties of a baryon can be derived from the valence quarks themselves (see Section 3.2), the sea quarks also have a role to play, e. g. in the induced polarization of baryons produced in high-energy collisions, as will be examined further in this chapter.

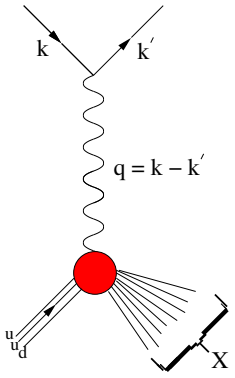

Figure 3.1: Feynman diagram of a simple deep-inelastic scattering experiment.

3.1 Structure, Distribution, and Fragmentation Functions... Oh My!

The cleanest way to examine the proton is to scatter an electron from it. In quantum electrodynamics (QED), a virtual photon mediates the interaction between particles. Essentially, the electron is simply a means to provide this virtual photon to scatter from the proton, as seen in Figure 3.1. The electron has initial 4-momentum k and final 4-momentum k'. A virtual photon of 4-momentum $q = k - k' = (\nu, \vec{q})$ is emitted, where ν is the energy component and $\vec{q}$ is the 3-momentum vector.

We define the quantity $Q^2 \equiv -q^2$, where Q^2 is a positive number that represents the "virtuality" of the photon, *i. e.* how far the photon mass is from that of a real photon (of mass zero). The cross-section for deep inelastic electron-proton scattering is as follows [20]

$$\left.\frac{d\sigma}{dE'd\Omega}\right|_{lab} = \frac{\alpha^2}{4E^2\sin^4\left(\frac{\theta}{2}\right)}\left\{W_2(\nu, Q^2)\cos^2\left(\frac{\theta}{2}\right) + 2W_1(\nu, Q^2)\sin^2\left(\frac{\theta}{2}\right)\right\} \tag{3.1}$$

Here W_1 and W_2 are structure functions that take into account the fact that the proton has some structure and is not a simple point particle, while θ is the angle through which the electron is scattered (in the rest frame of the proton target). It is important to note how the observed substructure of the nucleon changes as one varies Q^2. As one approaches higher Q^2, an interesting phenomenon occurs. With increasing photon energies, the wavelength of the incident photon becomes smaller and smaller, thus being able to resolve smaller structures

within the proton. Generally, the proton structure functions are functions of two independent variables, for example ν and Q^2 in eqn. (3.1). However, in deep inelastic scattering at high Q^2, pointlike constituents within the proton are revealed as one begins to resolve the quark substructure of the nucleon. The structure functions can now be written in terms of a ratio $x \equiv Q^2/2M\nu$ (with M the rest mass of the target proton and ν evaluated in the target's rest frame) of the previously independent variables ν and Q^2, *i. e.*

$$\begin{aligned} \nu W_2(\nu, Q^2) &\rightarrow F_2(x) = \textstyle\sum_i e_q^2 x f_i(x) \\ M W_1(\nu, Q^2) &\rightarrow F_1(x) = \tfrac{1}{2x} F_2(x) \end{aligned} \tag{3.2}$$

The results are said to "scale:" at high enough energies, they lose their dependence on Q^2 and depend only on the fraction x of the proton's momentum carried by the struck quark (in the infinite-momentum frame of the proton). This Deep Inelastic Scattering (DIS) regime is $Q^2 > 1$ GeV^2 and $W^2 > 4$ GeV^2, where W^2 is the invariant mass squared of the final-state hadronic system and is calculated by adding the 4-momentum of the virtual photon with that of the target proton.

The structure functions do retain a weak, logarithmic dependence on Q^2, termed a scaling violation. With increasing Q^2, the structure functions will start to increase at small x and decrease at larger values of x. Whereas at lower Q^2 the virtual photon sees quarks of higher momentum fraction, at higher Q^2 one begins to see quarks at a lower momentum fraction, termed "soft" quarks due to energy being emitted in the form of gluon radiative corrections. One finds, that the gluonic component of the proton is also resolved at higher Q^2.

In the scaling regime of DIS, one thus appears to be scattering from pointlike quarks. The basic semi-inclusive (SIDIS) reaction studied at HERMES is $e^- + p \rightarrow e^{-'} + h + X$ where h is some hadron and X is whatever is left over, within the constraints of conservation of four-momentum. The fraction of the energy of the hadron to the total energy available to it is denoted $z_h \equiv E_h/\nu$. The unpolarized SIDIS cross section factorizes in the following way

in leading order QCD (see [21] and [22]):

$$d\sigma^h \sim \sum_q e_q^2 f_1^q(x, Q^2) D_1^{q/h}(z_h, Q^2) \tag{3.3}$$

Here $d\sigma^h$ represents the differential cross section for producing a hadron h and e_q is the charge of the struck quark. $f_1^q(x, Q^2)$ is the "parton distribution function" (PDF) for a quark of flavor q giving the number density of hadrons of such quarks with momentum fraction x at a certain value of Q^2 in the target nucleon. $D_1^{q/h}(z_h, Q^2)$ is the fragmentation function which describes the number density of hadrons type h with momentum fraction z_h to be produced when a quark of flavor q is struck in the target. The cross section sums over the quark flavors $q = u, d, s$.

Finally, the variable Feynman-x, denoted x_F:

$$x_F \equiv \frac{p_{\parallel,boost}}{p_{\parallel,MAX}} \tag{3.4}$$

where $p_{\parallel,boost}$ is the hadron momentum component along the virtual photon direction evaluated in the γ^*-p frame (i. e. the rest frame of the virtual photon and target proton) and $p_{\parallel,MAX}$ is the maximum value this momentum component can have in this same frame. In general, $x_F > 0$ denotes hadrons produced in the "current-fragmentation" region and $x_F < 0$ is denotes those produced in the target fragmentation region. These limits may not be strict limits, but they basically refer to two different production processes. In target fragmentation, the production of the produced baryon occurs mainly from partons involved from the target remnant left behind after the ejection of the struck quark. In current fragmentation, the process is more "forward", utilizing the momentum of the incident parton in conjuction with interactions with the target valence and/or sea to produce the resultant baryon. It is the current fragmentation regime that will be covered by the theory in this chapter.

3.2 Constituent Quark Model

As already pointed out, high energy scattering experiments have revealed that hadrons have complex substructures involving valence quarks, sea quarks, and gluons. In the simple(constituent) quark model, the contribution of the sea quarks is neglected and the complete wavefunction of baryons differ mostly in their valence and spin components.

The complete wavefunction of bound state fermions was thought to be a product of a spatial term, a flavor term (including the valence quarks of the baryon only), and a spin term (of the valence quarks only). This wavefunction must be anti-symmetric with respect to particle exchange [20]. However, this posed a problem with the apparently symmetric wavefunctions of baryons such as the Δ^{++}. To resolve this puzzle, it was proposed that there existed another property of quarks called "color" to correct for the required symmetry. Thus, there is one more piece to the complete wavefunction, a color term, i. e. [20]

$$|\phi>_{Total} \;=\; |\phi>_{spatial}\,|\phi>_{flavor}\,|\phi>_{spin}\,|\phi>_{color} \tag{3.5}$$

Also, it is a fundamental concept in QCD that the color component of any hadron's wave function be a color singlet. Hence,

$$|\phi>_{color} \;=\; \sqrt{\frac{1}{6}}(RGB - RBG + BRG - BGR + GBR - GRB). \tag{3.6}$$

Combining the three quark flavors (u, d, and s) with the two quark spin states (along or against the baryon's spin direction), one may construct the constituent-quark wavefunctions.

For the Λ, the baryon of interest in this thesis, one obtains:

$$
\begin{aligned}
|\Lambda\uparrow> \;=\; & \frac{1}{3\sqrt{2}}[u(\uparrow)d(\downarrow)s(\uparrow) - d(\uparrow)u(\downarrow)s(\uparrow) - u(\downarrow)d(\uparrow)s(\uparrow) + d(\downarrow)u(\uparrow)s(\uparrow) \\
& + s(\uparrow)u(\uparrow)d(\downarrow) - s(\uparrow)d(\uparrow)u(\downarrow) - s(\uparrow)u(\downarrow)d(\uparrow) + s(\uparrow)d(\downarrow)u(\uparrow) \\
& + u(\uparrow)s(\uparrow)d(\downarrow) - d(\uparrow)s(\uparrow)u(\downarrow) - u(\downarrow)s(\uparrow)d(\uparrow) + d(\downarrow)s(\uparrow)u(\uparrow)]. \qquad (3.7)
\end{aligned}
$$

$$
(3.8)
$$

By applying a constituent quark spin counting-operator to this wavefunction, one obtains $\Delta s = 1$ and $\Delta d = \Delta u = 0$, where $\Delta q =< N_{q\uparrow} > - < N_{q\downarrow} >$. Thus, in the constituent quark model, the spin of the Λ comes solely from the spin of the s quark.

3.3 Lund Model of the Fragmentation Process

In 1979, a phenomenological model was proposed by Bo Andersson, Gösta Gustafson, and Gunnar Ingelman of the University of Lund in Sweden to explain the observed polarization of the Λ particle in proton-proton and proton-nucleus scattering [23]. In this model, a struck proton releases a diquark composed of combinations of the up and down quarks from its valence quark structure. Also, a color dipole field, spatially confined to a flux tube, acts in one dimension extending from the point of collision to the diquark.

The diquark, found in spin/isospin 0 or 1 combinations, fragments in a jet similar to a single quark jet. A quark-antiquark pair comes from the breaking of the force field. If a $(ud)_0$ diquark (the subscript referring to the spin of the diquark) combines with strange quark coming from an $s\bar{s}$ pair, then a Λ results. Since the diquark has spin 0, the total spin of the Λ comes from the spin of the s quark, similar to the naive quark model.

Another assumption of the model is that the total transverse momentum is conserved in the force field. In other words, each quark in the quark-antiquark pair must have an equal, but opposite, transverse momentum. In the case of current fragmentation into a Λ, the diquark transverse momentum is approximately parallel to that of the s quark from the

string break.

The quarks, having a finite mass, must be produced at a certain distance apart from each other in order to have the required energy to form a pair (binding energy argument???). As such, they will have an orbital angular momentum transverse to the string force which must be compensated for by a spin in the opposite direction of the quark-antiquark pair. Making further assumptions about the form of the color field energy per unit length, the polarization of the quarks, and the transverse momentum distributions of the quarks from the string break and the diquark, they arrive at a form for the Λ polarization in good agreement with the experimental results.

This model can possibly be extended to the Ξ^0, but requires a slight modification due to the presence of two s quarks in its valence structure. In this case, a quark pair-antiquark pair must come out of the string break.

3.4 DGM Model of Hadron Polarization

The Degrand and Miettinen (DGM) model of hadron polarization has been around for a little over two decades now and provides a simple phenomenological view of the origin of the hadron spin [24],[25], and [26]. It has been successful in predicting the previously observed Λ and $\bar{\Lambda}$ polarization in proton-proton collider experiments, but has failed in other ways, such as not predicting any polarization in any antiparticle.

The DGM model takes as its premise a parton-recombination approach. When forming a hadron, as many quarks as possible are taken from the high momentum, valence quarks of the incoming beam and the rest are obtained from the sea and valence quarks of the target (see Fig 3.2). A general baryon is pictured as a combination of a quark-diquark pair, with the diquark being composed of the most similar of the quarks found in the proton/target reaction. In the case of the Λ in proton-proton interactions, one has a spin zero (ud)-diquark from the valence quarks of the incident proton beam interacting with a strange quark from

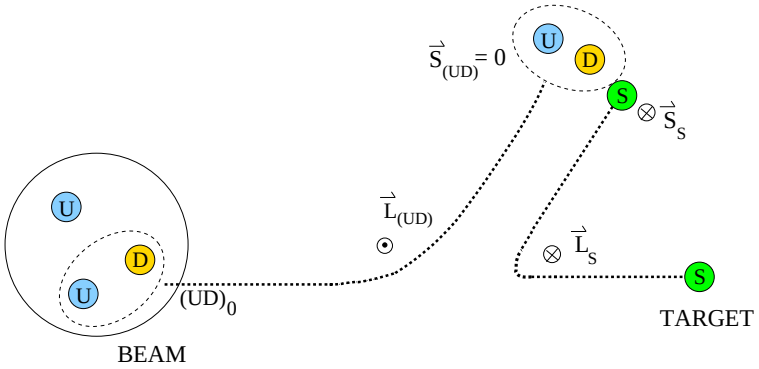

Figure 3.2: Proton incident on some target to create a Λ particle. Also shown are the spin, $\vec{S}$, and angular momentum, $\vec{L}$ of the diquark, (ud), and quark, s, referred to in the DGM model.

the sea of the target (labeled as a VVS recombination for Valence-Valence-Sea). Similar to the naive quark model, the strange quark would, thus, be responsible for the entire spin contribution to the Λ.

The general trend observed in the DGM model is the tendency for fast partons (those coming from the incident beam) to be spin up while slow partons (from the target sea) are spin down. DGM explains this behavior as due to Thomas Precession. Thomas precession is caused by non-collinear boosts and is entirely a relativistic effect. In the case of hadron formation, this precession of the quark spin, ω_T, is caused by the quark velocity, $\vec{V}$, crossed with the force used to combine the constituent quarks into the final hadron state, $\vec{F}$, i. e. $\omega_T \propto \vec{F} \times \vec{V}$. Since the force $\vec{F}$ is mainly along the direction of the incident beam, this precession will mainly be caused by the transverse momentum of the quark.

The contribution to the Hamiltonian from the Thomas Precession is:

$$H_{Prec} = \vec{S} \cdot \vec{\omega_T} \tag{3.9}$$

where $\vec{S}$ is the spin of the quark. Since the force acting on the "fast" quarks works to decelerate them, it will have the opposite sign as that of the force acting on the "slow" quarks. Thus, ω_T will have opposite signs for "fast" and "slow" quarks, requiring that the spin of the quark be adjusted to minimize its effect on the Hamiltonian, or rather causing $\vec{S}$ to be positive for "fast" quarks and negative for "slow" quarks.

The DGM model goes even further in describing the resultant polarization of the Λ. The contribution H_{Prec} written in terms of potential scattering leads to the result that the angular momentum of the the strange quark must be aligned with its spin, as shown in Fig 3.2 wherein both of these vectors are into the page, the s quark getting its angular momentum from accelerating towards the (ud) diquark. However, the spin polarization axis, $n \equiv p_{BEAM} \times p_{\Lambda}$, is out of the page. Thus, the polarization of the Λ, which, as noted earlier, is related to the spin of the strange quark only, will be negative.

This model can also describe the polarization resulting from quarks from jets in fragmentation processes. The polarization is simply that of the corresponding mesons so that, a strange quark from a jet will have the same polarization as that of a K^- when forming a Λ. Since the angular momentum in this case is out of the page, the resulting polarization of the Λ will be positive.

3.5 Quark Recombination Model of Hadron Polarization

When Degrand and Miettinen first proposed their model, they had included an estimate of the x_F and p_T dependence for the Λ only. The Quark Recombination Model (QRC) suggested by Kubo et al is an advancement of the DGM model towards a more quantitative picture of hadron polarization [27][28][29]. In doing this, they will not assume purely Thomas Precession, but will try to operate in the most general fashion allowable.

In the case of the Λ, the production probability, $S_{p\to\Lambda}$, involves the final state wavefunction of the Λ, the initial wavefunction of the s quark, the initial wavefunction of the $(ud)_0$ diquark, and the interaction term representing the probability of the partons to form a final state Λ. Placing the x-axis as the momentum direction parallel to the incident beam, the $(ud)_0$ diquark is composed of a gaussian-momentum distribution along the y and z-axis plus

the momentum distribution of the diquark in the proton along the x-axis, i. e.

$$G_{(ud)^0/p} = q_{(ud)^0/p}(x_1)e^{-(y_1^2+z_1^2)} \tag{3.10}$$

The s quark wavefunction is written as a gaussian of its perpendicular momentum components plus an additional step function used to guarantee that the parallel momentum of the diquark is greater, i. e.

$$f_s = \theta(x_1 - x_2)e^{-(y_2^2+z_2^2)} \tag{3.11}$$

Assuming that the interaction between the two partons can be written as a scalar potential (a vector potential changes a sign and so causes cancellations that will eliminate any spin dependent influences), Kubo et al arrived at the equation:

$$P_N(\Lambda) = R_0 \frac{\int [dx_i dy_i dz_i/x_i] G_\Lambda^2 \sigma_{dep} f_s G_{(ud)^0/p} \Delta^3 \Delta^4}{\int [dx_i dy_i dz_i/x_i] G_\Lambda^2 \sigma_{ind} f_s G_{(ud)^0/p} \Delta^3 \Delta^4} \tag{3.12}$$

where σ_{dep} is the spin dependent cross section, σ_{ind} is the spin independent cross section, and R_0 was fixed to fit the prediction for the Λ to the experimental data. Once this was done, then all the other polarizations involving a spin 0 diquark could be predicted and compared to theory. It should be noted, that the spin dependence was found to come from interference between up to second order and higher terms of the interaction potential.

As mentioned before, there were some polarizations for which the DGM predicted both a wrong sign or a wrong amplitude. An adjustment to this model, denoted DMNM for DeGrand Miettinen New (extended) Mechanism, explained these by exploiting the fact that pions (or ud quark/anti-quark pairs) are easily formed as a precursor to the final state products due to the fact that they are composed of two of the lightest mesons. So, for the Λ, the picture is more or less identical to that in Fig 3.2, but that the diquark is not a remnant of the proton, but rather a pion formed by the proton-proton interaction. Using this mechanism, one would derive the same polarization as before for the Λ, but now there is a mechanism by which anti-hadrons can obtain polarization.

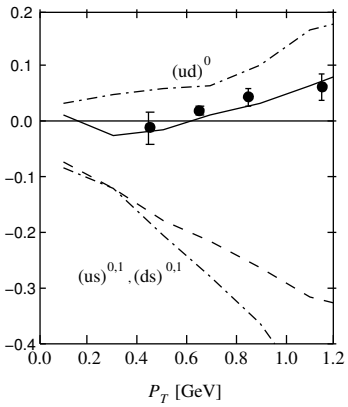

Figure 3.3: Prediction of the Λ polarization of $\gamma p \to \Lambda X$. Data points are taken from previous HERMES preliminary data and the solid line represents the fit to the data with the QMM model. Please see text for reference.

Finally, Kubo et. al. made further predictions with the quark recombination model coupled with their so-called quark masses mechanism (QMM) in the case of photoproduced Λs [30]. This model takes into account the quark distribution of a photon for the valence quark contribution to the Λ and the mass dependence of forming the related sea-diquark from the proton target. It is expected that the probability of forming a particular diquark will decrease with the mass. The results are shown in Figure 3.3[30]. The dashed line represents an older prediction without accounting for the mass differences in the diquarks and the data points are taken from previously released, preliminary HERMES data.

3.6 Anselmino Prediction for HERMES SIDIS Λ Polarization

M. Anselmino et al. have created a model of Λ polarization based on a fragmentation approach and utilizing their own form of a polarized fragmentation function [31]. Affects due to the possible polarizations of the target (and its corresponding quarks) are ignored, largely due to the reason that, at least in the current fragmentation region, the polarization has less to do with the target than with the process by which the hadron is formed. Thus, they

used an unpolarized fragmentation function coupled with their own fragmentation function $\Delta^N D_{h\uparrow/a}$, where the $h\uparrow$ refers to the polarized hadron, the Λ, and the a is in reference to the quark from which the fragmentation occurs.

This new type of fragmentation function is similar to the another T-odd fragmentation function, $D_{1T}^{\perp}$ and the exact relation between the two is given by Anselmino et al. as

$$\Delta^N D_{h\uparrow/a} = 2\frac{k_\perp}{M_h}\sin\phi D_{1T}^{\perp}(z, k_{perp}) \tag{3.13}$$

where $k_\perp$ is the transverse momentum of the Λ and ϕ is the angle between $k_\perp$ and the transverse polarization vector. This function is parametrized and fit to data on $pBe \to \Lambda^\uparrow X$, $pBe \to \bar{\Lambda}^\uparrow X$, and $pp \to \Lambda^\uparrow X$ for both fragmentation from an up and down quark (assumed to be the same) as well as from a strange quark.

Using their fit for the polarized fragmentation function, Amselmino et al. proceeded to make predictions for other processes, such as $e^+p \to e^+\Lambda^\uparrow X$ used at HERMES and $\nu p \to \nu\Lambda^\uparrow X$ as seen at NOMAD [32][33]. It is important to note, that in their formalism the negative contribution from the up/down quark fragmentation functions is expected to overwhelm the positive contribution from the strange quark fragmentation functions due to the greater charge of the up quark (and, thus, contribution to the cross-section). After applying the model over the kinematic region appropriate to HERMES, they arrived at a prediction for the Λ polarization in SIDIS as seen in Figure 3.4[33].

3.7 Formula for Measuring the Λ Polarization

The key to measuring the Λ polarization is always in measuring its decay products, most specifically the proton. Recall in Chapter 1, the formula for angular distribution of the decayed proton was written (Eqn. 1.1)

$$\frac{dN}{d\Omega} = \left(\frac{dN}{d\Omega}\right)_0 \left(1 + \alpha P_n^\Lambda \cos(\theta_p, n)\right)$$

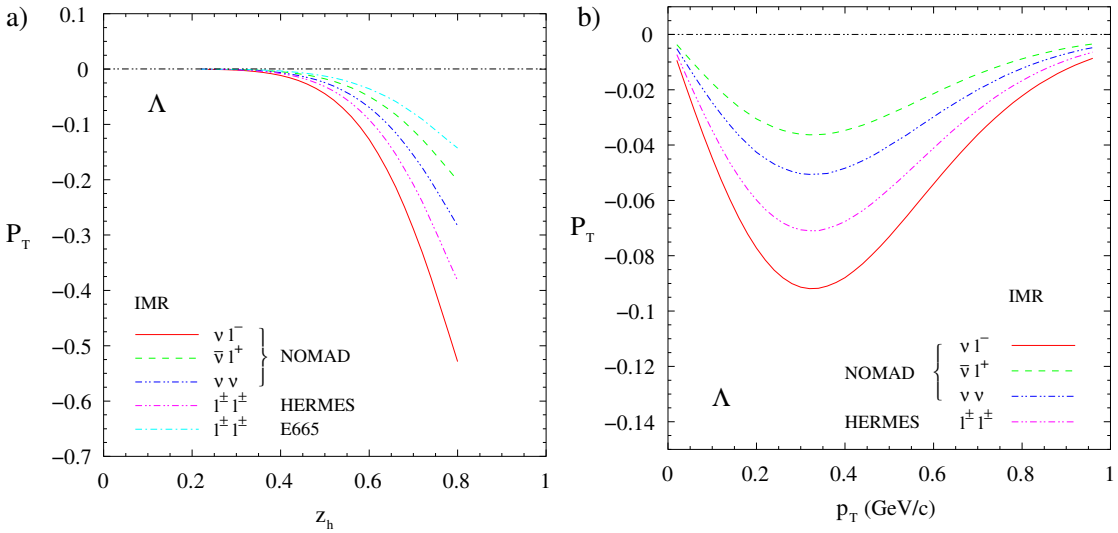

Figure 3.4: a) Transverse Λ polarization as a function of z_h averaged over the transverse Λ momentum. b) Transverse Λ polarization as a function of the transverse Λ momentum when averaged over the range $0.4 < z < 0.8$. Please see text for reference.

The method of moments used in this analysis uses the following moments:

$$\begin{aligned} < \cos\theta_p > &\equiv \frac{\int \cos\theta_p \frac{dN}{d\Omega} d\Omega}{\int \frac{dN}{d\Omega} d\Omega} \\ < \cos\theta_p >_0 &\equiv \frac{\int \cos\theta_p \frac{dN_0}{d\Omega} d\Omega}{\int \frac{dN_0}{d\Omega} d\Omega} \\ < \cos^2\theta_p >_0 &\equiv \frac{\int \cos^2\theta_p \frac{dN_0}{d\Omega} d\Omega}{\int \frac{dN_0}{d\Omega} d\Omega} \end{aligned} \tag{3.14}$$

Using these moments, one can arrive at the equation

$$< \cos\theta_p > \;=\; \frac{< \cos\theta_p >_0 + \alpha P_n^\Lambda < \cos^2\theta_p >_0}{1 + \alpha P_n^\Lambda < \cos\theta_p >_0} \tag{3.15}$$

Experimentally, the cosine moments can be measured as

$$< \cos^m\theta_p > \;=\; \frac{1}{N_\Lambda} \sum_{i=1}^{N_\Lambda} \cos^m\theta_{p,i}. \tag{3.16}$$

where N_Λ is the number of Λ events and $\cos^m\theta_{p,i}$ is the cosine of the angle between the proton momentum and the Λ polarization axis for an event i. Please note that N_Λ will, unfortunately include some background events that will have to be subtracted later. This will also mean that there will be a contribution to the cosine moments from the background

that must also be considered. The details of this background subtraction will be seen later in Section 5.2. The unpolarized moments need a little more thought. Due to the top/bottom symmetry of the HERMES spectrometer, $< \cos\theta_p >_0^{TOP} = - < \cos\theta_p >_0^{BOT}$. This means that $< \cos\theta_p >_0 = < \cos\theta_p >_0^{TOP} + < \cos\theta_p >_0^{BOT} = 0$. Also, due to the cosine dependence in the the proton angular distribution, the unpolarized, second cosine moment is equal to the polarized, cosine moment, i. e. $< \cos^2\theta_p >_0 = < \cos^2\theta_p >$. It can be shown, after some work, that any higher moments due to the HERMES spectrometer acceptance will cancel due to the top/bottom symmetry. The final result of all this is the following:

$$P_n^\Lambda = \frac{1}{\alpha} \frac{< \cos\theta_p >}{< \cos^2\theta_p >} \tag{3.17}$$

From this point, there were four different approaches to determining the cosine moments. The first approach involves taking the second cosine moment as in Eqn. 3.16. The first cosine moment is taken to be

$$< \cos\theta_p > = 0.5 * \left[\frac{1}{N_\Lambda^{TOP}} \sum_{i=1}^{N_\Lambda^{TOP}} \cos\theta_{p,i} + \frac{1}{N_\Lambda^{BOT}} \sum_{j=1}^{N_\Lambda^{BOT}} \cos\theta_{p,j} \right] \tag{3.18}$$

where N_Λ^{TOP} is the number of Λ events in the top of the spectrometer and N_Λ^{BOT} is the number of Λ events in the bottom of the spectrometer. This was used as the measured first cosine moment for which the background was subtracted. It was separated into the top and bottom moments to account for any possible inefficiencies in the spectrometer. The polarization is determined by taking this expression for the first cosine moment and substituting it into Eqn. 3.17

The second approach is very similar, except that the first and second moments in the top and bottom of the spectrometer are computed individually and background subtracted individually to give the *true* first and second cosine moments. The equation for the polarization in this case is then

$$\alpha P_n^\Lambda = \frac{< \cos\theta >_{TOP}^{TRUE} + < \cos\theta >_{BOT}^{TRUE}}{< \cos^2\theta >_{TOP}^{TRUE} + < \cos^2\theta >_{BOT}^{TRUE}} \tag{3.19}$$

It must be considered that an even weighting of events in the top and the bottom of the spectrometer may be inappropriate in the case of large discrepancies in the number of events in the top and in the bottom. In this case, a weighted average of the *true* moments in the top and bottom should perhaps be used as follows

$$\alpha P_n^{\Lambda} = \frac{< \cos\theta >_{TOP}^{TRUE} + \beta < \cos\theta >_{BOT}^{TRUE}}{< \cos^2\theta >_{TOP}^{TRUE} + \beta < \cos^2\theta >_{BOT}^{TRUE}} \tag{3.20}$$

where $\beta \equiv N_{BOT}/N_{TOP}$.

Finally, there is a method constructed by the St. Petersburg group in HERMES called the iterative method. This is a modification of the even weighting formula meant to correct for some acceptance effects seen in the first cosine moment. The formula using this iterative correction is as follows:

$$\alpha P_n^{\Lambda} = \frac{\frac{<\cos\theta>_{TOP}^{TRUE} + <\cos\theta>_{BOT}^{TRUE}}{<\cos^2\theta>_{TOP}^{TRUE} + <\cos^2\theta>_{BOT}^{TRUE}}}{1 - \frac{(<\cos\theta>_{TOP}^{TRUE} - <\cos\theta>_{BOT}^{TRUE})^2}{<\cos^2\theta>_{TOP}^{TRUE} + <\cos^2\theta>_{BOT}^{TRUE}}} \tag{3.21}$$

However, it is not exactly clear as to which formula one should use. Should there be a difference in the number of events in the top of the spectrometer and the bottom? Are there other reasons to support the use of the even averaging formula in place of one of the others? These questions are studied further in Chapter 4.

Chapter 4

Monte Carlo Studies

4.1 GMC_LPOL – A Polarized Λ Generator

GMC_LPOL is a polarized Λ Monte Carlo generator based on GMC_DISNG and written in order to cross check my Λ-polarization analysis code. In its original form, it was used specifically for semi-inclusive Λ analysis. In this regime, the Λ polarization axes could be defined in the Λ CM frame or the γ^*-Proton frame, where γ^* refers to the virtual photon. The inclusion of the γ^*-Proton frame was due to the fact that this frame might be more suited to comparison with models proposed by theorists. To see a comparison between these two Monte Carlo generators, please see Figure 4.1, which are plots prepared by Professor N. C. R. Makins.

As the study of the Λ evolved, it became necessary to study the inclusive regime of Λ production. The option to study this regime was added to GMC_LPOL in a clever way. If $|\vec{Q}|$ is set equal to *zero*, then the scattering angle of the lepton will also be *zero*, aligning $\vec{Q}$ with the incoming beam axis and providing the definition of the photoproduction polarization

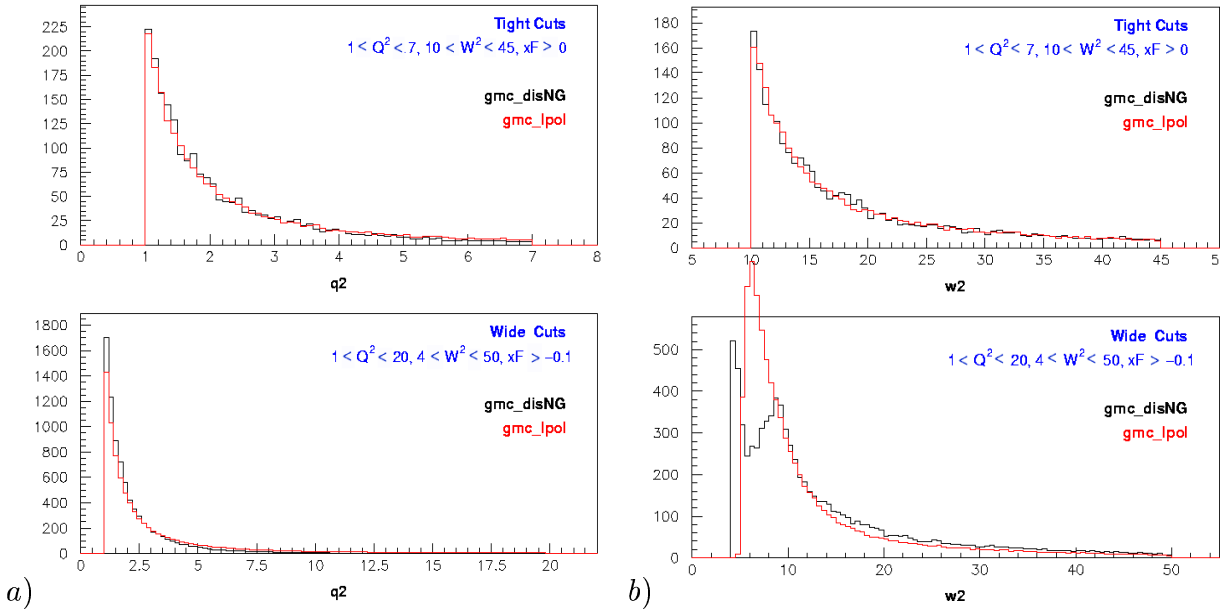

Figure 4.1: Comparison of a GMC_LPOL to GMC_DISNG for some sample kinematics.

axis using the existing Monte Carlo code for SIDIS, or, in equation form:

$$\begin{aligned} \vec{n}_{SIDIS} &= \hat{Q} \times \vec{p}_{\Lambda} \\ &= \hat{p}_{BEAM} \times \vec{p}_{\Lambda} \\ &= \vec{n}_{incl} \end{aligned}$$

where $\vec{n}_{SIDIS}$ is the polarization axis for the semi-inclusive Λ, $\vec{p}_{\Lambda}$ is the momentum of the Λ, and $\vec{n}_{incl}$ is the polarization axis for the inclusive Λ. This direction is defined in all the Monte Carlo studies shown here to be along the y-axis. The direction of the Λ momentum is chosen to be along the z-axis and the x-axis is chosen so as to form a right handed coordinate system.

The standard Monte Carlo chain used starts with GMC_LPOL. Events are produced in 4π, but a selector file is used to constrain those events written to disk to those events within a more confined region about the HERMES spectrometer, although liberal enough to not introduce an artificial acceptance into the next step. These events are then piped into the HERMES Monte Carlo, HMC. This is a GEANT based Monte Carlo with a thorough reconstruction of the HERMES spectrometer and its detector responses. This can unfortunately

have the affect of *re-decaying* the Λ in the spectrometer if one is not careful to turn this feature off. If the Λ was re-decayed in this Monte Carlo, the input polarization would be lost. The resulting events are then put through the HERMES Reconstruction Code, HRC, and, finally, through the udst-writer, where the results are written in a form that can be read by my Λ analysis code.

Some results for the photoproduction (inclusive) case using Eqn 3.18 are shown in Table 4.1. In trial one, the polarization along the x, z-axes are computed in the same fashion as that along the y-axis. This is expected to fail since the only reason why the polarization determination along the y-axis is possible is due to the top/bottom symmetry of the spectrometer (the magnet ruining left/right symmetry). In trial two, a smaller polarization is attempted and the x, z-components are properly ignored. In trial three, a completely unphysical test was conducted showing that, if there *did* exist a polarization along an axis that was not along the y-axis (which is, again, impossible due to the required pseudovector nature of the Λ spin polarization), then the ability to measure the Λ polarization would be impaired. Also shown, for the sake of completeness, is a test of the ability to measure the Λ polarization in the case of high Q^2, the semi-inclusive regime (again using Eqn 3.18), in Table 4.2.

4.2 Λ Kinematics Study

The lack of $\vec{Q}$ in the inclusive Λ studies presents a problem for theoretical interpretation in that x_F cannot be determined. A suitable alternative needed to be found. For this purpose, the variable ζ was used. By definition,

$$\zeta \equiv \frac{E^\Lambda + p_z^\Lambda}{E^k + k} \tag{4.1}$$

where E^Λ is the energy of the Λ particle, p_z^Λ is the z-component of the Λ momentum, E^k is the energy of the incoming positron, and k is the momentum of the positron, all measured

	Polarization Component	Set Value	Extracted Value	Uncert.
trial 1	x-axis	0	1.551	0.062
	y-axis	1	0.992	0.034
	z-axis	0	-1.648	0.016
trial 2	x-axis	0	—	—
	y-axis	0.47	0.468	0.025
	z-axis	0	—	—
trial 3	x-axis	1	—	—
	y-axis	0	0.033	0.015
	z-axis	0	—	—

Table 4.1: Monte Carlo results from GMC_LPOL using the photoproduction (inclusive) option and defining the Λ polarization axes in the Λ CM frame.

	Polarization Component	Set Value	Extracted Value	Uncert.
trial 1	x-axis	0	—	—
	y-axis	1	0.992	0.041
	z-axis	0	—	—

Table 4.2: Monte Carlo results from GMC_LPOL using the standard high Q^2 (semi-inclusive) option and defining the Λ polarization axes in the γ^*-proton CM frame.

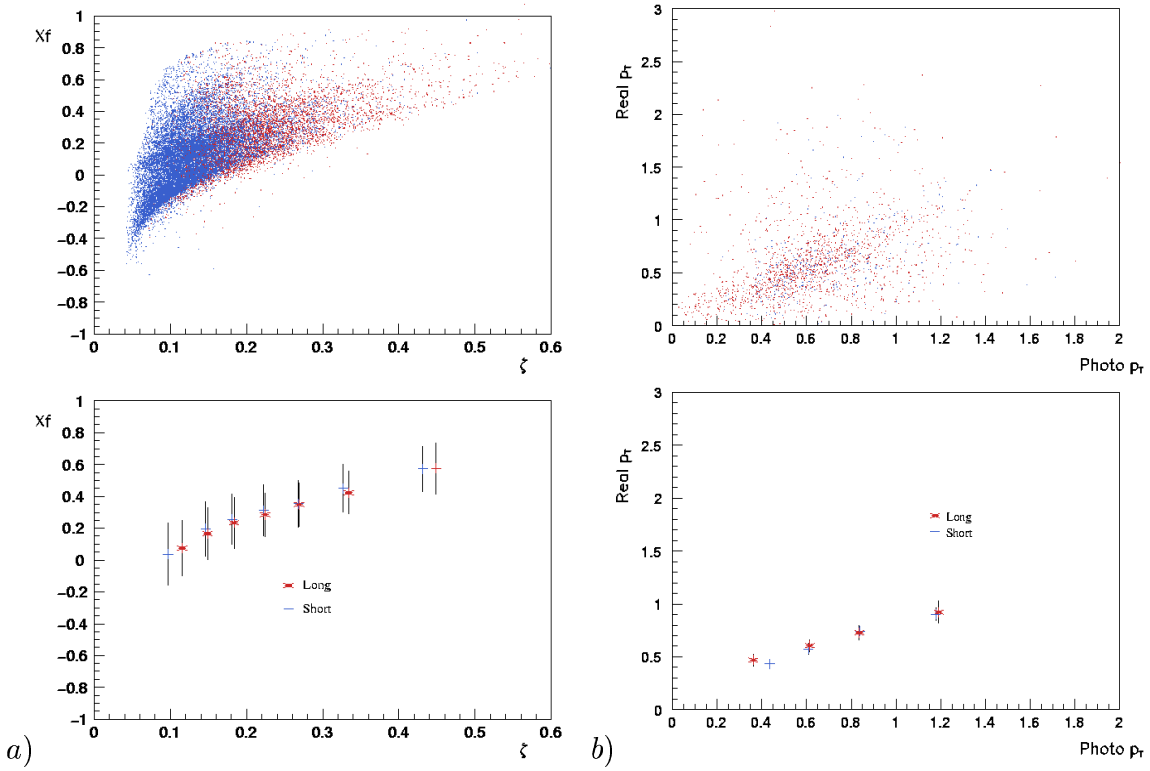

Figure 4.2: Monte Carlo plots of a) x_F vs. ζ and b) the "real" p_T vs the "photoproduction" p_Ti for $\zeta > 0.25$. The lower panel of each plot shows the standard deviation from the average value in each bin. Long tracks are represented in red and short tracks in blue.

in the positron-proton CM frame.

A plot of the relationship between ζ and x_F is shown in Figure 4.2(a). The long tracks are in red and the short tracks are in blue. This shows that $\zeta > 0.25$ implies $x_F > 0$, meaning that this is the current (forward) fragmentation region. The lower panel shows the standard deviation from the mean in each bin. In Figure 4.2(b), a comparison between "real" p_T, defined with respect to $\vec{Q}$ (which is known in the Monte Carlo), and the photoproduction p_T, defined with respect to the incoming positron beam axis, is shown for $\zeta > 0.25$. A plot of the comparison of the "real" and the photo transverse momentums for $\zeta < 0.25$ is not shown, but is very similar.

Finally, plots of x_F vs. the photoproduction p_T are shown in Figure 4.3 for (a) $\zeta < 0.25$ and for (b) $\zeta > 0.25$. The $\zeta < 0.25$ region is supposed to represent the target fragmentation region ($x_F < 0$), however the main exploration of the x_F region occurs *mainly* in the first

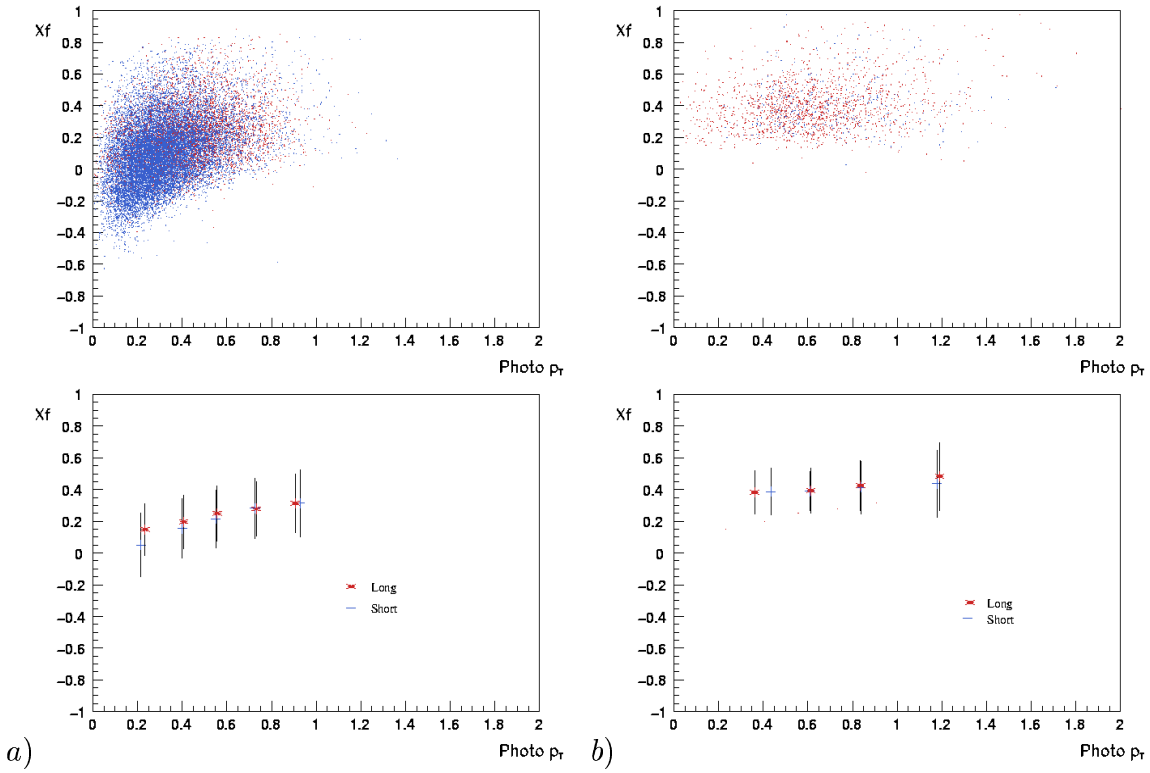

Figure 4.3: Monte Carlo plots of a) x_F vs. the photoproduction p_T for $zeta < 0.25$ and b) x_F vs. the photoproduction p_T for $zeta < 0.25$. The lower panel of each plot shows the standard deviation from the average value in each bin. Long tracks are represented in red and short tracks in blue.

transverse momentum, p_T, bin for the short tracks by examining the standard deviation (shown in the lower panels). This means that the region $\zeta < 0.25$ represents a mixture of target fragmentation and current fragmentation and will be hard to interpret in the data. Nevertheless, one would expect some evidence of the polarization of the Λ from the target remnant in this region.

4.3 Study of Top/Bottom Asymmetry

The formula derived for the transverse Λ polarization in the previous chapter, Eqn. 3.17, is dependent on the first and second cosine moments of the angle between the proton's momentum and the transverse polarization axis. This first moment, $< \cos\theta_P >$, presents a slight problem in the HERMES spectrometer. Ideally, one should be able to simply take the

average of $< \cos\theta_P >$ in the top with the same moment in the bottom to obtain the total cosine moment. However, when actually examining the data, it was found that there was often a discrepancy in the number of counts in the top and the bottom of the spectrometer that, at times, grew to the order of 8%. As such, it is reasonable to suggest either a weighted average of the top and bottom cosine moments using the number of counts in each half or to adjust the estimate of the systematic error. There are three possible sources of this top/bottom asymmetry in the data: the polarization of the Λ itself, an inefficiency in one or both of the spectrometer halves, and a misalignment of one or both of the spectrometer halves. These three cases will be studied in the following sections for obtaining the total cosine moment using the even weighting of the cosine moments in the top and bottom (Eqn 3.19), the weighted average of the cosine moments in the top and bottom (Eqn 3.20), and the iterative method (Eqn 3.21).

Before starting this study, it was desirable to implement a quicker method of generating Monte Carlo than that used above due to HMC being so slow and that will also allow us to similate long and short tracks. To accomplish all of this, the spectrometer "acceptance" was determined by using an ntuple of $\approx 45,000$ Λ candidates created from the 00d0 production data set. This "acceptance" was used to limit the events in the Monte Carlo appropriately. In Figure 4.4, a plot of the momentum, p, versus $\theta_x \equiv \arctan(p_x/p_z)$ for protons in the data (a) and the Monte Carlo (b) are shown along with some selected data points used to fit the boundary region for the long tracks also shown together with the fit to the boundary used to limit the Monte Carlo. Also, in Figure 4.5, p is plotted against θ_x for long and short track π^- in the data (a) and in the Monte Carlo (b). Again, the data points to fit the long and short track boundary regions are shown together with the corresponding fits. A momentum cut for the reconstructed Λ mass was added to both plots such that 1.08 GeV $< M_\Lambda <$ 1.16 GeV to better compare to the more limited range of Λ masses in the Monte Carlo.

Furthermore, to better simulate the data and the smearing of the detector, more features

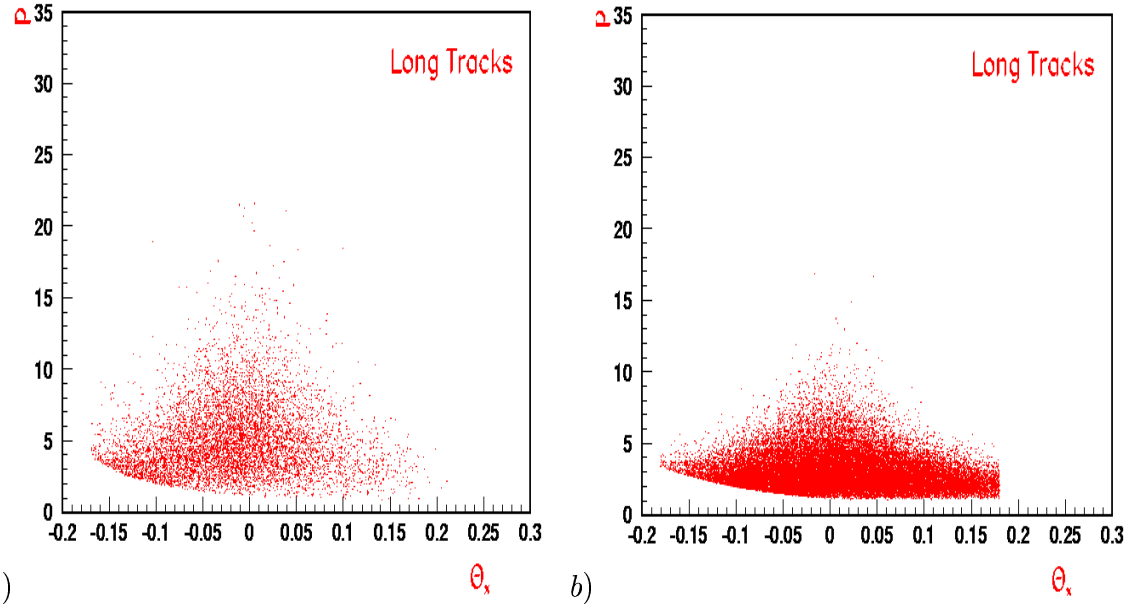

Figure 4.4: Plot of momentum vs. θ_x for proton long tracks in a) data and b) Monte Carlo. A momentum cut of 1.08 GeV $< M_\Lambda <$ 1.16 GeV was used.

were added to GMC_LPOL. First, the Λ mass peak can be assigned a gaussian width in the input to the Monte Carlo. Secondly, a *polarized* background can be added of a fixed background to signal ratio. The mass modulation of a background event, M^{BG}_{event}, is given by

$$M^{BG}_{event} = M_\Lambda + (1 + M_1 x + M_2 x^2) \tag{4.2}$$

where M_Λ is the actual value of the Λ mass, M_1 and M_2 are input parameters set equal to 2 for the coming studies, and x is a random number such that $1.08 - M_\Lambda < x < 1.16 - M_\Lambda$. The polarization modulation of a background event, P^{BG}_{event}, used in the following Monte Carlo studies is given by

$$P^{BG}_{event} = P^{BG}_{set}(1 + P_1(M^{BG}_{event} - M_\Lambda)) \tag{4.3}$$

where P^{BG}_{set} is the set value of the background polarization in the Monte Carlo and P_1 is an input parameter set equal to 2 for the coming studies. Examples of the mass peaks for the top (a) and bottom (b) halves of the spectrometer are shown in Figure 4.6.

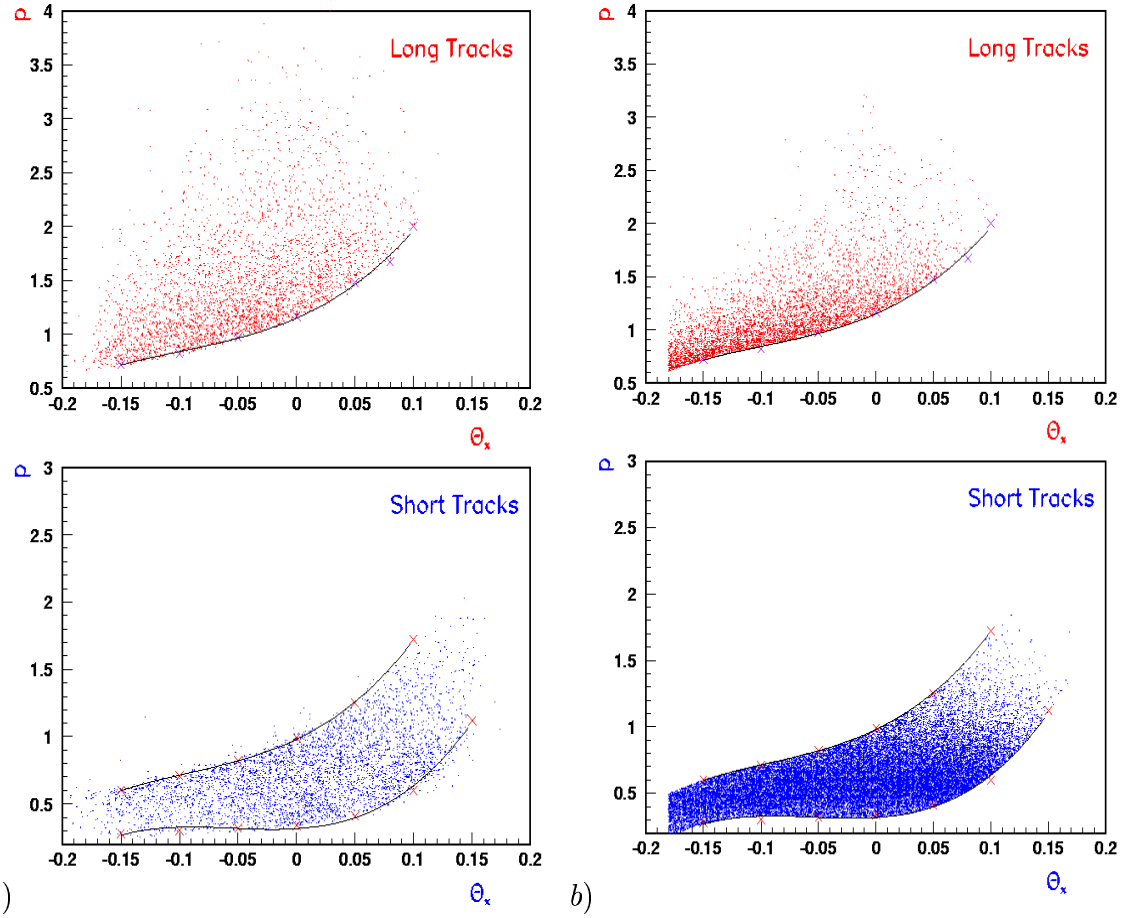

Figure 4.5: Plot of momentum vs. θ_x for π^- tracks in a) data and b) Monte Carlo. A momentum cut of 1.08 GeV $< M_\Lambda <$ 1.16 GeV was used. The long tracks are shown in the top panel and the short tracks are shown in the bottom.

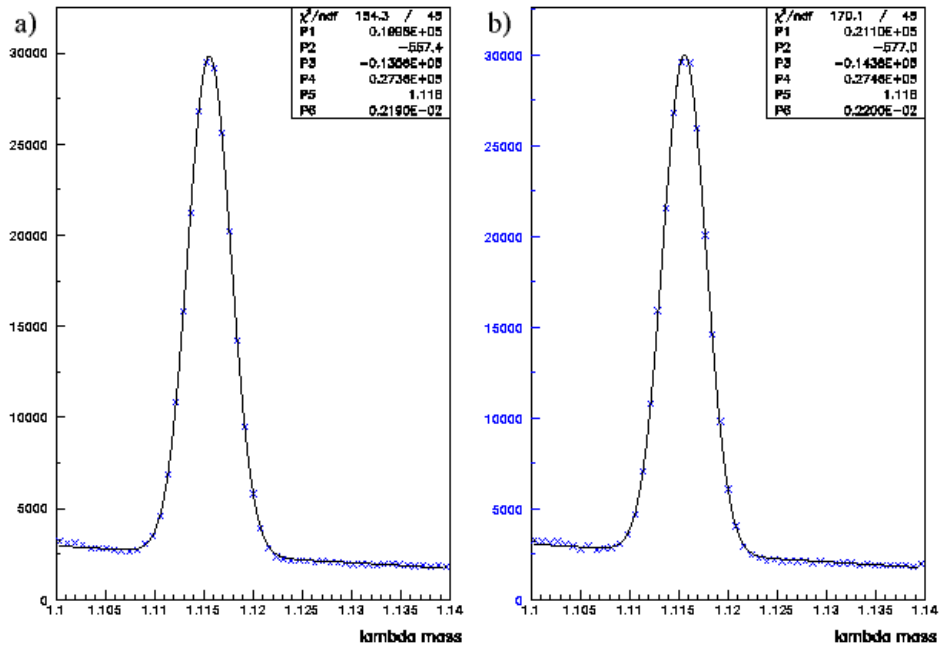

Figure 4.6: Monte Carlo Λ mass peaks with background fraction of 17%, a mass width of 0.0022 GeV. Λ polarization of 10%, and a background polarization of 15% for a) the top half of the spectrometer and b) the bottom half of the spectrometer.

4.3.1 Effect of Polarization on Top/Bottom Asymmetry

It has been hypothesized that the Λ polarization itself could provide a difference in the number of counts between the top half and the bottom half of the spectrometer. This is entirely due to the presence of the magnet, which will give a preference to charged particles to be accepted towards one side of the spectrometer over the other.

To study this effect, a large polarization was put into the Monte Carlo and the different formulas for the cosine moments (even weighting versus weighted average versus the iterera-tion method) were applied. The results on the top/bottom symmetry are seen in Table 4.3 as well as the ability of each formula to correctly determine the input polarization.

These results indicate that the Λ polarization does indeed cause a difference in the number of counts in the top and the bottom of the spectrometer. Also, the polarization using the weighted average of the top and the bottom cosine moments and the iterated formula seem

	long	short	both
P^{Λ}_{Even}	0.678 ± 0.015	0.880 ± 0.010	0.862 ± 0.008
$P^{\Lambda}_{Weighted}$	0.911 ± 0.016	0.904 ± 0.010	0.912 ± 0.008
N^{Top}_{total}	18480	75188	83623
N^{Bot}_{total}	24928	81852	106784
N^{Bot}/N^{Top}	1.35	1.09	1.14
$P^{\Lambda}_{iterate}$	0.918 ± 0.021	0.908 ± 0.010	0.912 ± 0.009

Table 4.3: Table of Monte Carlo results for an input Λ polarization of 0.90. In the case of the iterated formula, the cuts are slightly different, mainly cutting out low transverse momentum Λ particles.

to be preferred when there is a significant difference in the number of counts in the top and the bottom caused by the Λ polarization alone. However, a large polarization would be required to produce a top/bottom asymmetry of the order seen in some of the bins seen in the data. Thus, further tests are required before the declaration of the proper formula for the first cosine moment.

4.3.2 Effect of Inefficiencies in the Spectrometer

An inefficiency in one or both halves of the spectrometer could potentially cause a large error in weighting the cosine moments of the top and bottom of the spectrometer. This is a consequence of the loss of real events that are not measured by the spectrometer and whose contribution is not included in the appropriate cosine moment (top/bottom). This would tend to weight events more heavily in one half of the spectrometer for no physics reason whatsoever.

For a test of the effect of inefficiencies, a large 30% inefficiency was placed in the top half of the spectrometer. This was done by generating a random number between 0 and 1

P^{Λ}_{True}		long	short	both
0.10	P^{Λ}_{Even}	0.085 ± 0.010	0.104 ± 0.007	0.099 ± 0.006
	$P^{\Lambda}_{Weighted}$	0.366 ± 0.012	0.200 ± 0.007	0.235 ± 0.006
	N^{Top}_{total}	35352	127760	163187
	N^{Bot}_{total}	51733	184250	236112
	N^{Bot}/N^{Top}	1.46	1.44	1.45
	$P^{\Lambda}_{Iterate}$	0.120 ± 0.014	0.108 ± 0.007	0.107 ± 0.006
0.90	P^{Λ}_{Even}	0.679 ± 0.017	0.882 ± 0.011	0.864 ± 0.009
	$P^{\Lambda}_{Weighted}$	1.121 ± 0.017	0.990 ± 0.010	1.024 ± 0.009
	N^{Top}_{total}	12908	52787	65713
	N^{Bot}_{total}	24928	81852	106784
	N^{Bot}/N^{Top}	1.93	1.55	1.63

Table 4.4: Table of Monte Carlo results for an input Λ polarization of 0.10 and 0.90 with an inefficiency of 30% in the top half of the spectrometer. In the case of the 0.10 polarization, the iterative procedure has slightly different cuts, mainly cutting out low transverse momentum Λ particles.

and throwing the event out if the random number is greater than 0.70 for events in the top half of the spectrometer. This test was performed at the same, high polarization as in the previous section and at 10%. These results are presented in Table 4.4.

In this case of a 30% inefficiency of the top half of the spectrometer, it is seen that the even weighting of the cosine moments in the top and the bottom of the spectrometer does not cause and significant deviation from the values listed in Table 4.3 in the case of 90% polarization. The weighted averaging of these moments, however, causes a severe difference. This is also noticeable at a more reasonable polarization of 10%, where one would expect the weighted averaging technique to be similar, if not better still, to the even weighting technique were there no inefficiency. Finally, the iterative procedure, being similar to the

even averaging technique, but being corrected to take into account the asymmetry caused by the Λ polarization, predicts the polarization correctly and, thus, accounts for the inefficiency. Note, as a cross check, that the number of counts in the bottom half of the spectrometer is identical in both tables, as is expected since there was no change of efficiency there.

4.3.3 Effects of Misalignment in the Spectrometer

Finally, the effects of a misalignment of the spectrometer on the top/bottom asymmetry was also be studied. To conduct this test, a misalignment in the θ_x and $\theta_y \equiv \arctan(p_y/p_z)$ variables was purposefully inserted into the Monte Carlo results for the top and the bottom of the spectrometer separately. The amount of the misalignment was taken from a thorough study of the spectrometer misalignment performed by Alexander Kisselev and Antje Bruell of the HERMES collaboration. The following misalignments were determined:

	TOP	$BOTTOM$
$xslope:$	$0.44\ mrad$	$0.24\ mrad$
$yslope:$	$-1.20\ mrad$	$0.02\ mrad$

To introduce an xslope, for instance, of 0.44 mrad, the value of θ_x obtained from Monte Carlo needs to be shifted by an amount -0.44 mrad, i. e. opposite the physical slope of the spectrometer piece.

A large inefficiency, such as that used in the last section, is not expected so, for this test, perfect efficiency in both the top and the bottom of the spectrometer was used. Also, the results have been examined over a range of polarizations. In Table 4.5, Λ polarizations have been measured for input polarizations of 10% and 20% and NO misalignments for comparison. In the case of no misalignments, it is seen that the weighted averaging of the top and bottom moments and the iterative procedure are more desirable. However, once misalignments are introduced, as seen in Table 4.6, the advantages of the weighted averaging are not as obvious.

P^{Λ}_{True}		long	short	both
0.10	P^{Λ}_{Even}	0.079 ± 0.009	0.103 ± 0.006	0.098 ± 0.005
	$P^{\Lambda}_{Weighted}$	0.094 ± 0.011	0.104 ± 0.006	0.101 ± 0.005
	N^{Top}_{total}	50250	182795	232921
	N^{Bot}_{total}	51733	184250	236112
	N^{Bot}/N^{Top}	1.03	1.01	1.01
	$P^{\Lambda}_{Iterate}$	0.111 ± 0.013	0.108 ± 0.007	0.106 ± 0.006
0.20	P^{Λ}_{Even}	0.152 ± 0.009	0.202 ± 0.006	0.194 ± 0.005
	$P^{\Lambda}_{Weighted}$	0.198 ± 0.011	0.206 ± 0.006	0.203 ± 0.005
	N^{Top}_{total}	49406	181741	231174
	N^{Bot}_{total}	52598	184953	237535
	N^{Bot}/N^{Top}	1.07	1.02	1.03
	$P^{\Lambda}_{Iterate}$	0.214 ± 0.013	0.209 ± 0.007	0.208 ± 0.006

Table 4.5: Table of Monte Carlo results for an input Λ polarization of 0.10 and 0.20 with NO misalignments.

P^{Λ}_{True}		long	short	both
0.05	P^{Λ}_{Even}	0.043 ± 0.009	0.058 ± 0.006	0.052 ± 0.005
	$P^{\Lambda}_{Weighted}$	0.019 ± 0.011	0.054 ± 0.006	0.045 ± 0.005
	N^{Top}_{total}	52489	185544	237859
	N^{Bot}_{total}	51506	183659	235180
	N^{Bot}/N^{Top}	0.98	0.99	0.99
	$P^{\Lambda}_{Iterate}$	0.061 ± 0.013	0.063 ± 0.007	0.057 ± 0.006
0.10	P^{Λ}_{Even}	0.081 ± 0.009	0.107 ± 0.006	0.099 ± 0.005
	$P^{\Lambda}_{Weighted}$	0.071 ± 0.011	0.104 ± 0.006	0.096 ± 0.005
	N^{Top}_{total}	52115	185361	237133
	N^{Bot}_{total}	51923	184330	236196
	N^{Bot}/N^{Top}	1.00	0.99	1.00
	$P^{\Lambda}_{Iterate}$	0.114 ± 0.013	0.112 ± 0.007	0.107 ± 0.006
0.20	P^{Λ}_{Even}	0.154 ± 0.009	0.205 ± 0.006	0.196 ± 0.005
	$P^{\Lambda}_{Weighted}$	0.174 ± 0.011	0.205 ± 0.006	0.199 ± 0.005
	N^{Top}_{total}	51270	184219	235379
	N^{Bot}_{total}	52768	184849	237795
	N^{Bot}/N^{Top}	1.03	1.00	1.01
	$P^{\Lambda}_{Iterate}$	0.217 ± 0.013	0.213 ± 0.007	0.209 ± 0.006

Table 4.6: Table of Monte Carlo results for an input Λ polarization of 0.05, 0.10, and 0.20 with θ_x and θ_y misalignments.

4.4 Conclusions From Monte Carlo

Three possible causes of the asymmetry in the number of counts in the top and the bottom of the spectrometer have been examined: the polarization of the Λ, an inefficiency in the spectrometer, and a misaligment of the spectrometer. The first, the polarization of the Λ itself, favors using a weighted average of the cosine moments of the top and the bottom of the spectrometer or an iterative procedure. However, some of the asymmetries are too large in the data to in comparison to that given in the Monte Carlo at a similar polarizations. This would tend to indicate that the polarization of the Λ is not completely responsible for the top/bottom asymmetry observed in the data.

Thus, in any case of a misalignment or inefficiency, the even averaging of the top and bottom cosine moments of the spectrometer must be favored over the weighted averaging. It should be noted that, in cases where there is little to no asymmetry in the top and bottom, both the weighted average and the even averaging technique are practically identical. Unfortunately, for bins showing a large Λ polarization, the effect of this polarization is not properly accounted for with the even averaging technique.

However, in *all* cases, the iterative procedure works in predicting the input polarization in the Monte Carlo. To get a better estimate of any corrections in addition to the K^0_S polarization, covered in Chapter 5, more statistics are needed. The plots for an input polarization of 0.05 for P_Λ vs. *zeta*, P_Λ vs. p_T ($\zeta < 0.25$), and P_Λ vs. p_T ($\zeta > 0.25$) are shown in Figures 4.7,4.8,4.9, respectively. In these plots, the closed, red circles are the long tracks using the iteration method and the triangles represent the even weighting method. The long tracks and short tracks are distinguished by being filled points or open points, respectively. The same plots are also made for the input polarization of 0.10 (Figures 4.10,4.11,4.12) and 0.20 (Figures 4.13,4.14,4.15). These values of input polarization sufficiently cover the range of polarizations seen in the experiment, as will be seen in the next chapter.

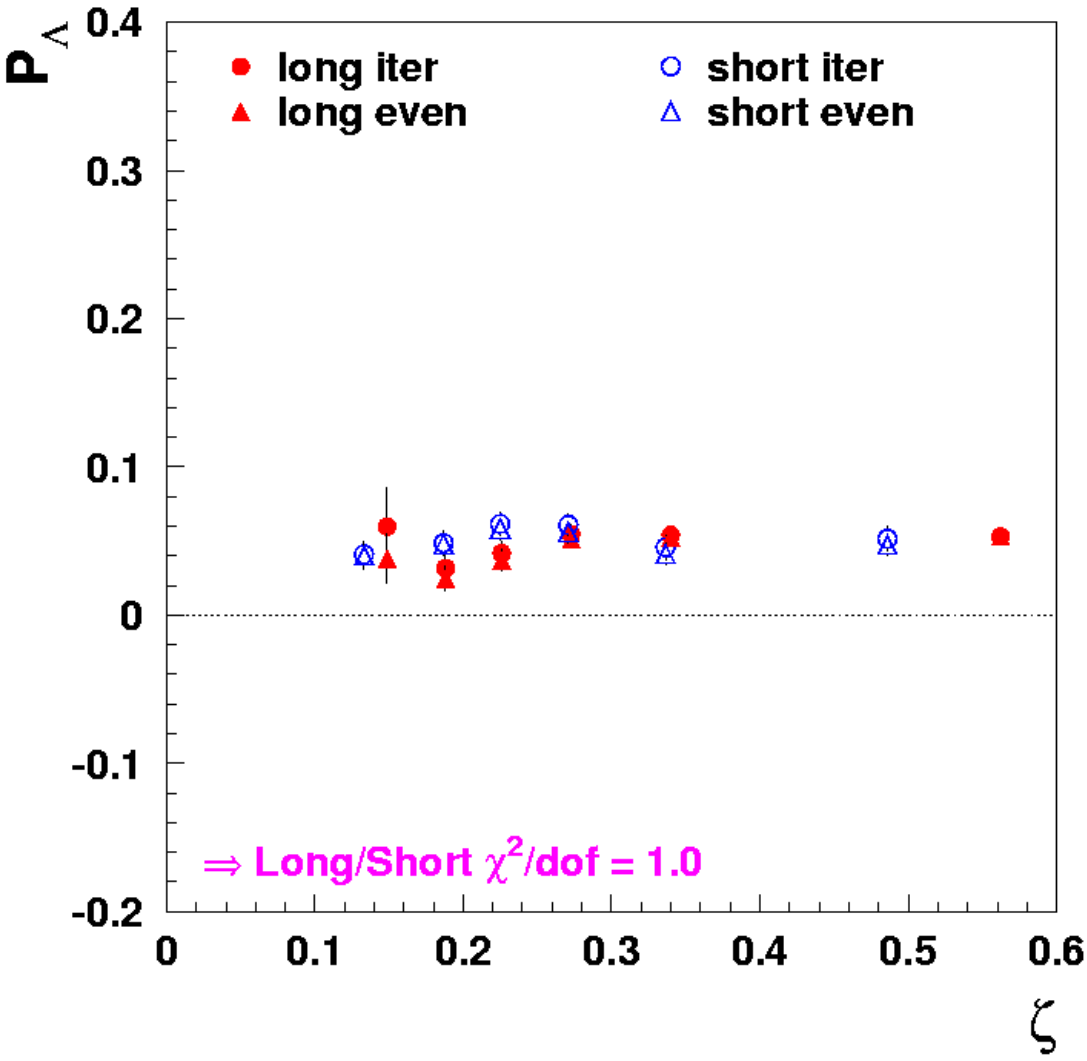

Figure 4.7: Λ polarization versus ζ for long and short tracks in a large statistics set of Monte Carlo for an input polarization of 0.05 and comparing the iteration technique and the even weighting formula.

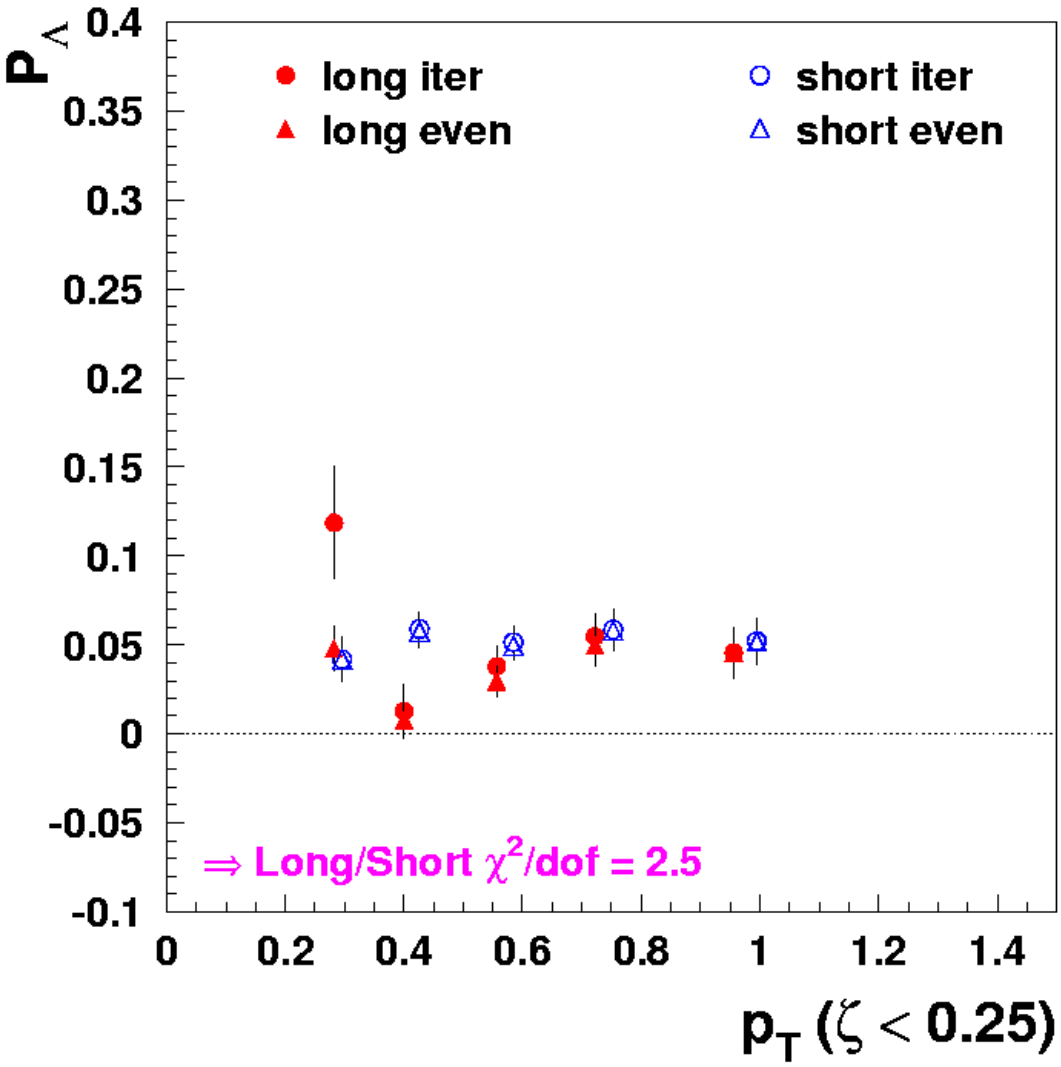

Figure 4.8: Λ polarization versus p_T in the region $\zeta < 0.25$ for long and short tracks in a large statistics set of Monte Carlo for an input polarization of 0.05 and comparing the iteration technique with the even weighting formula.

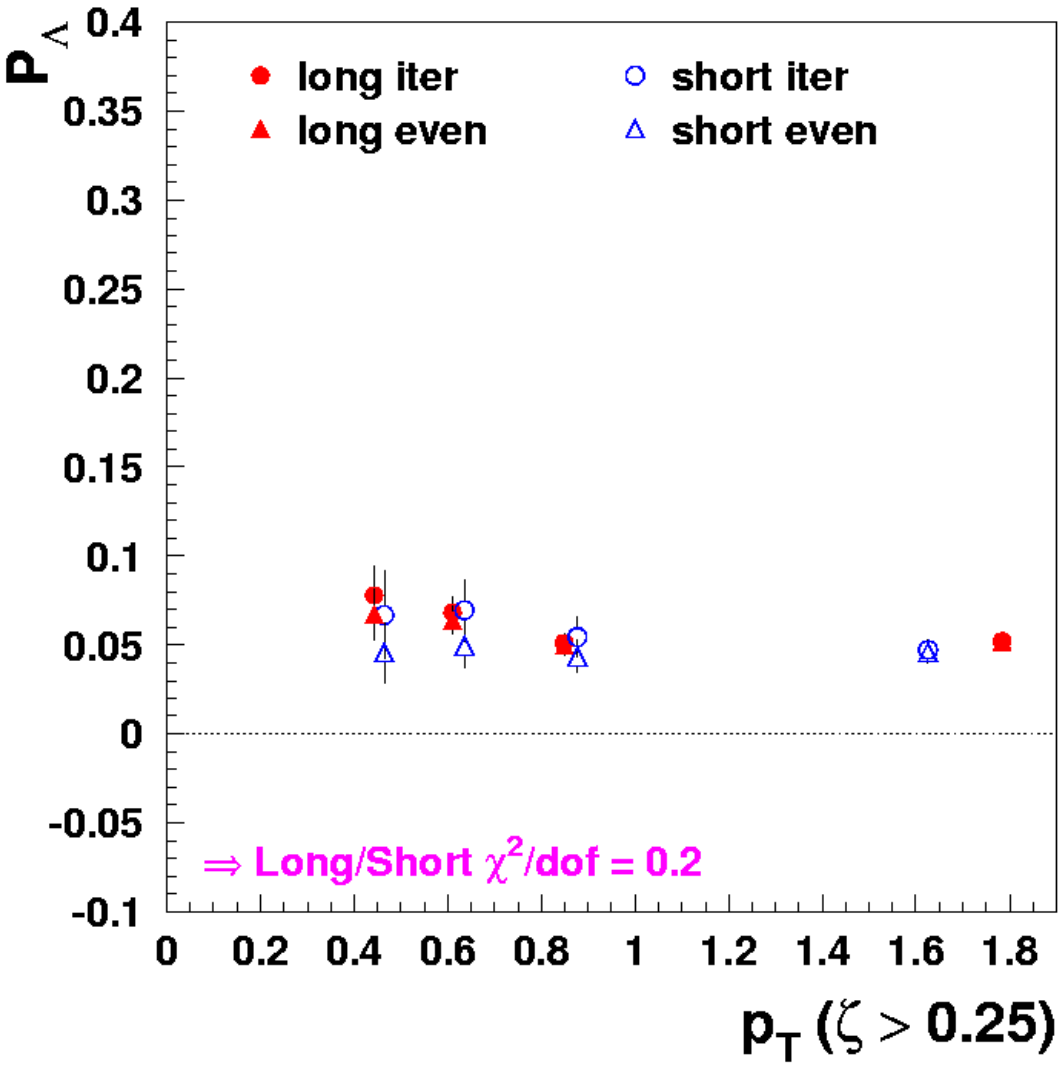

Figure 4.9: Λ polarization versus p_T in the region $\zeta > 0.25$ for long and short tracks in a large statistics set of Monte Carlo for an input polarization of 0.05 and comparing the iteration technique with the even weighting formula.

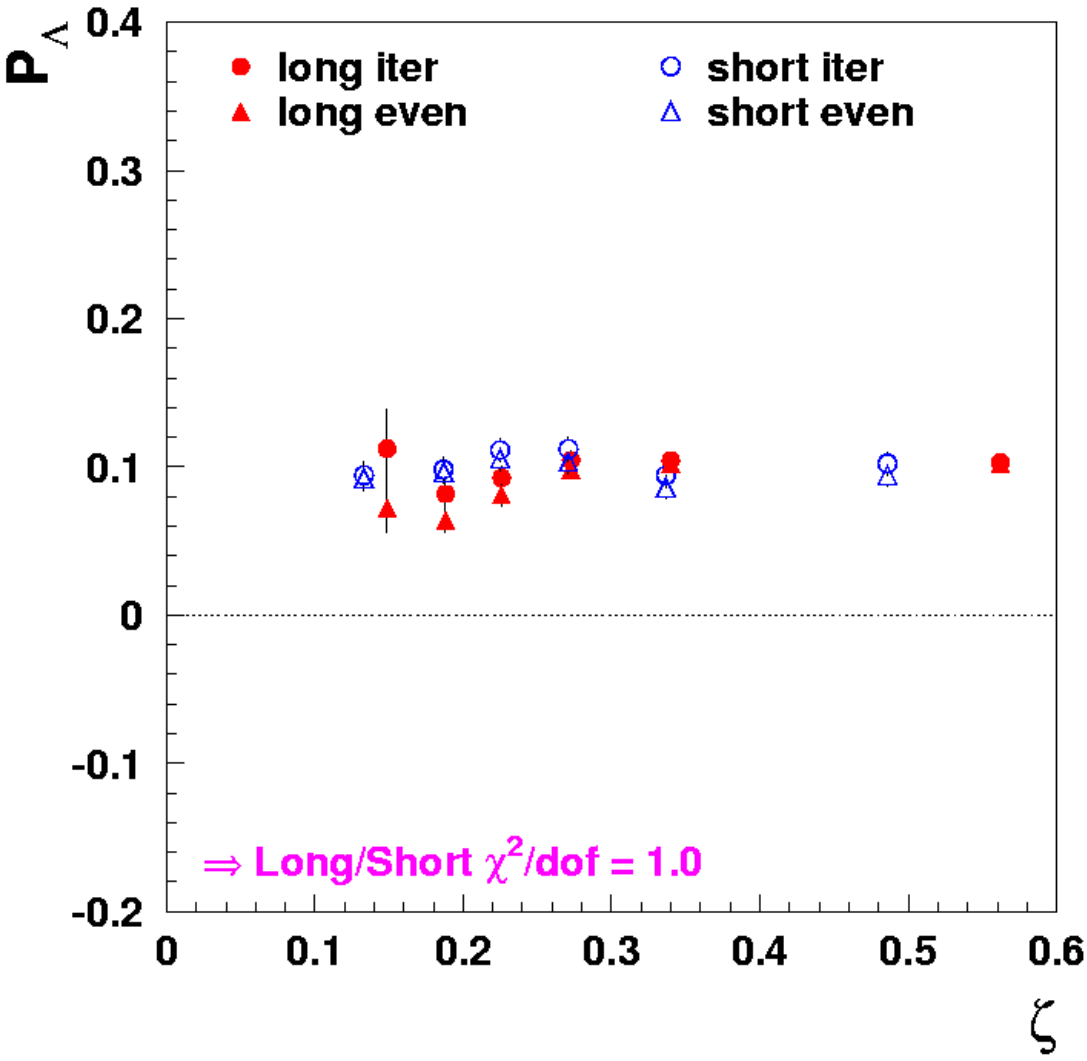

Figure 4.10: Λ polarization versus ζ for long and short tracks in a large statistics set of Monte Carlo for an input polarization of 0.10 and comparing the iteration technique and the even weighting formula.

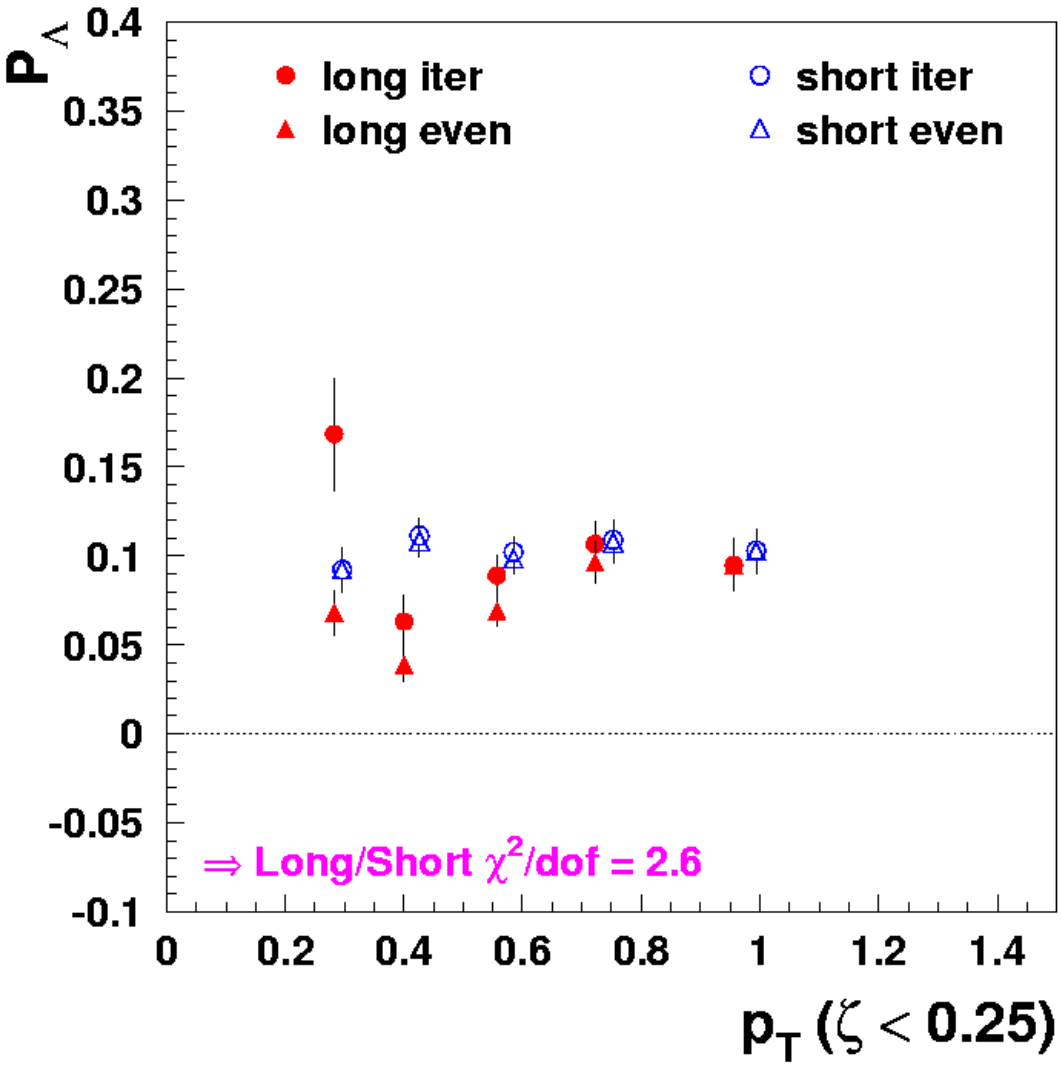

Figure 4.11: Λ polarization versus p_T in the region $\zeta < 0.25$ for long and short tracks in a large statistics set of Monte Carlo for an input polarization of 0.10 and comparing the iteration technique with the even weighting formula.

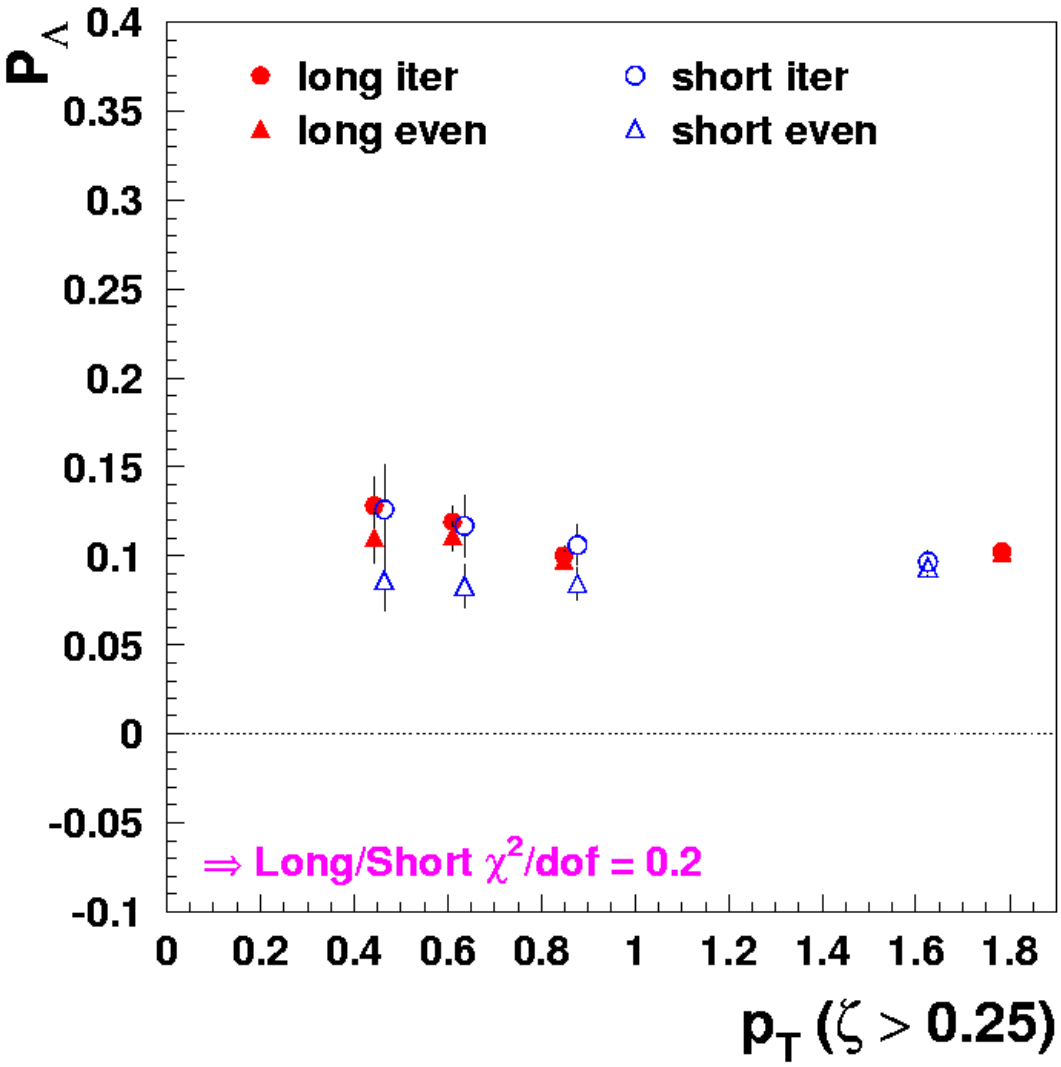

Figure 4.12: Λ polarization versus p_T in the region $\zeta > 0.25$ for long and short tracks in a large statistics set of Monte Carlo for an input polarization of 0.10 and comparing the iteration technique with the even weighting formula.

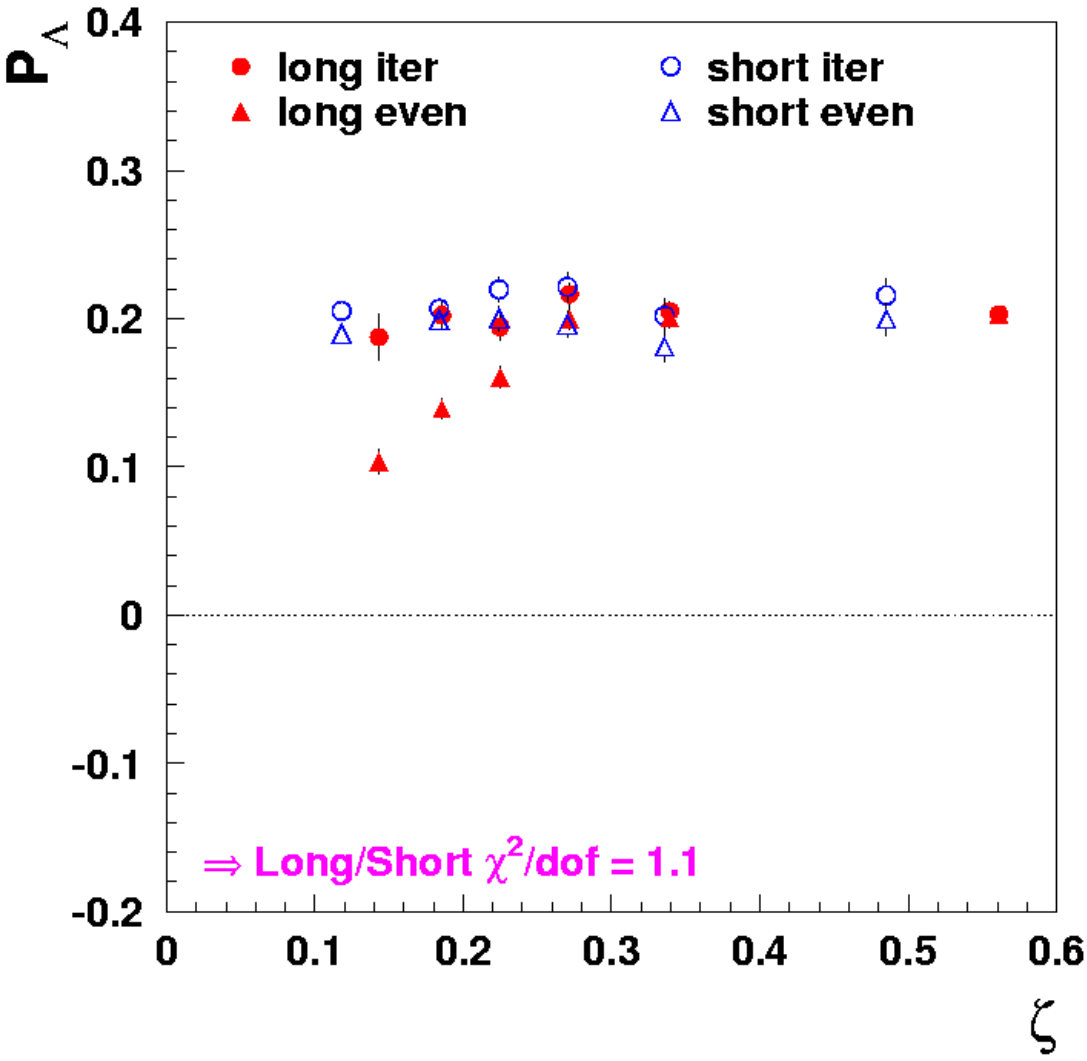

Figure 4.13: Λ polarization versus ζ for long and short tracks in a large statistics set of Monte Carlo for an input polarization of 0.20 and comparing the iteration technique and the even weighting formula.

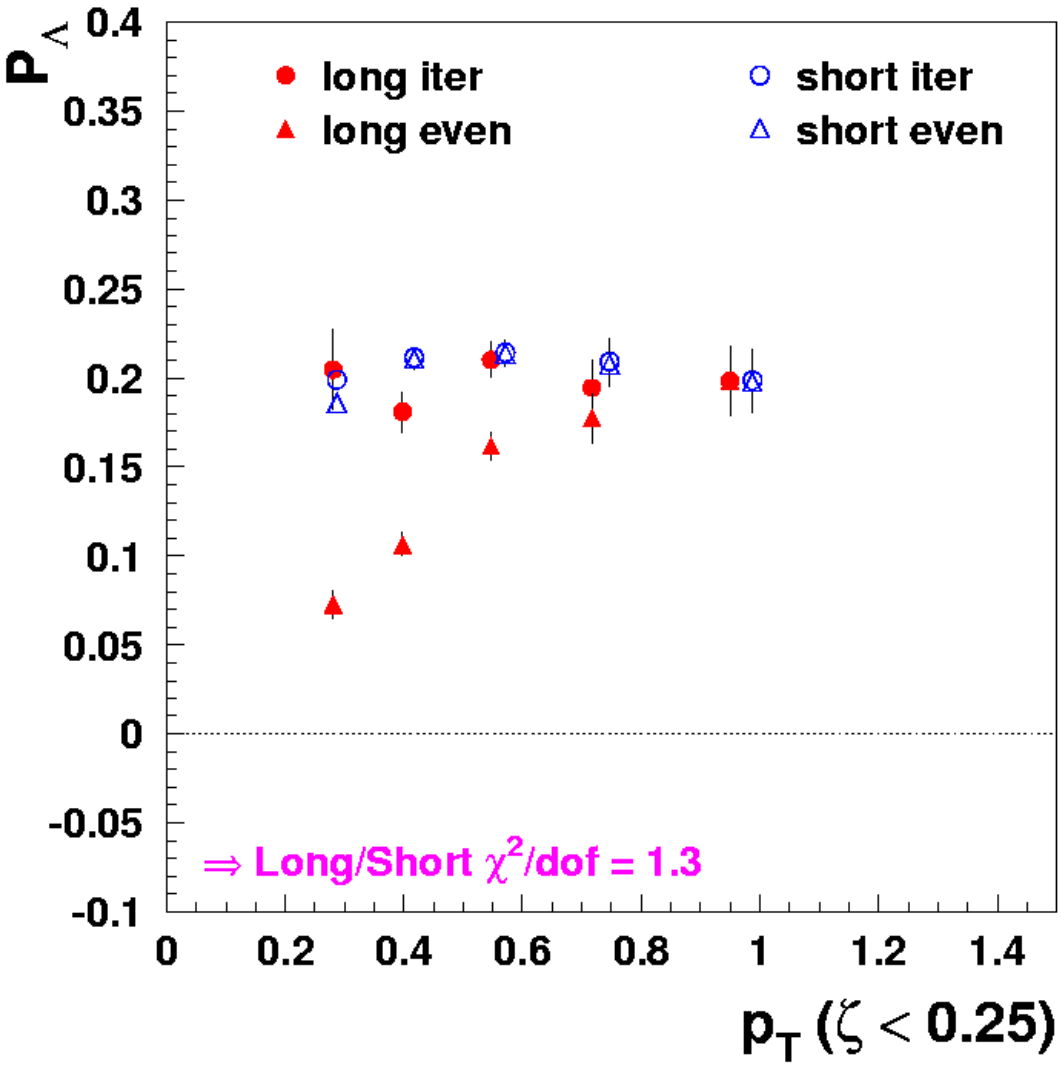

Figure 4.14: Λ polarization versus p_T in the region $\zeta < 0.25$ for long and short tracks in a large statistics set of Monte Carlo for an input polarization of 0.20 and comparing the iteration technique with the even weighting formula.

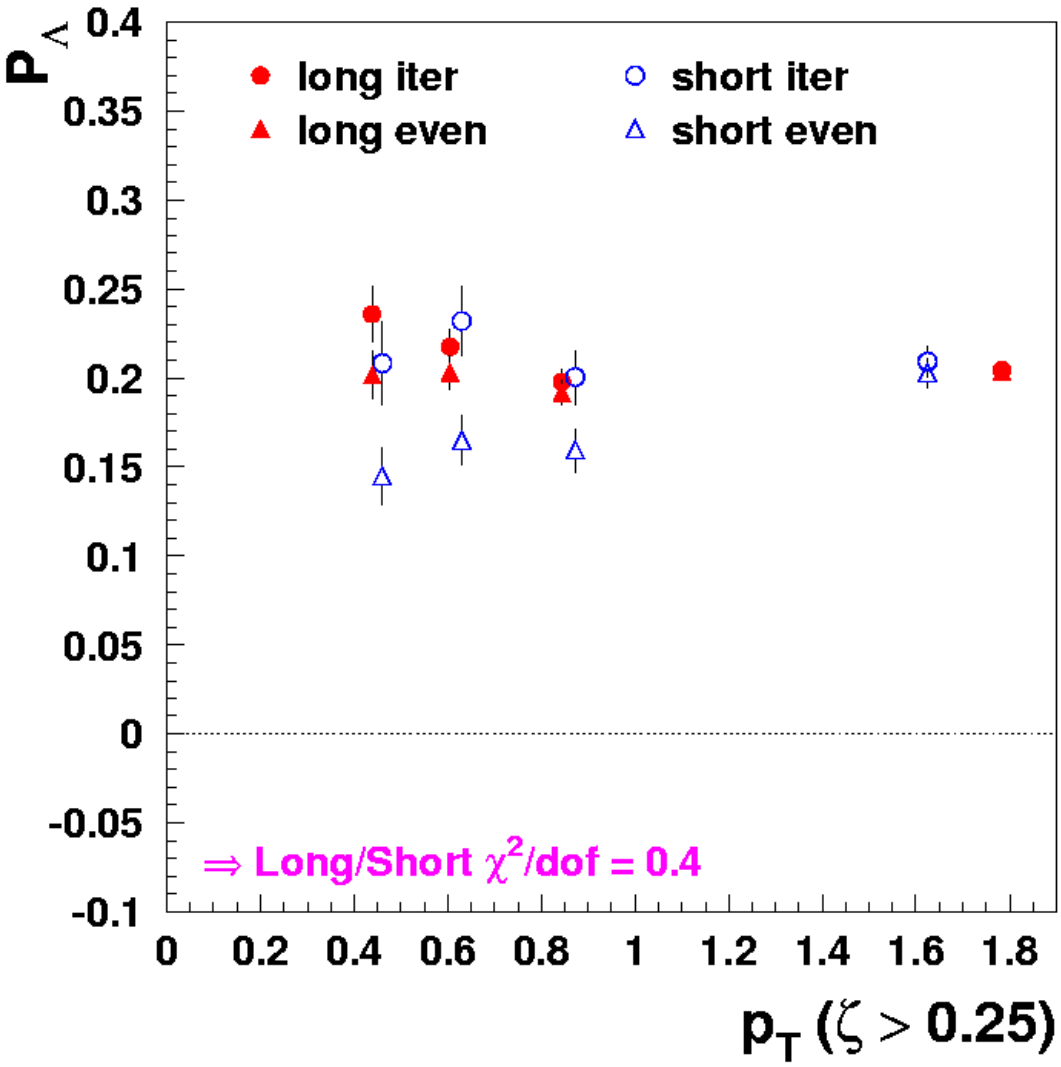

Figure 4.15: Λ polarization versus p_T in the region $\zeta > 0.25$ for long and short tracks in a large statistics set of Monte Carlo for an input polarization of 0.20 and comparing the iteration technique with the even weighting formula.

Chapter 5

The Spin of the Λ at HERMES

5.1 The Extraction of the Λ from the Data

The Λ is a neutral particle and, as such, can not be measured by the HERMES spectrometer. However, it can be reconstructed from its decay products, the proton and π^-. To insure a clean Λ sample, a series of cuts are made to reduce the background (without significantly decreasing the true Λ signal). These cuts will be slightly different depending on whether one is reconstructing the Λ in the low Q^2 (photoproduction) regime or the high Q^2 (SIDIS regime). These cuts will be described in the following sections.

Please note that cuts involving particle ID, burst cuts, fiducial volume cuts, and the separation of the proton and pion tracks used to reconstruct the Λ are used to create an ntuple of possible Λ candidates. The background is subtracted using the remaining cuts in a combination of C and PAW programs. The cuts listed are for the Λ. For $\bar{\Lambda}$, simply replace the proton with an anti-proton and the π^- with a π^+.

Also of note is the x, y, z coordinate system defined by HERMES. The $z-axis$ is defined as the axis directly along the beam pipe. It is assumed that the incident beam lies directly along this axis and, except for some small angle deviations, this is more or less true. The $y-axis$ is defined to point up (toward the upper half of the spectrometer from the lower

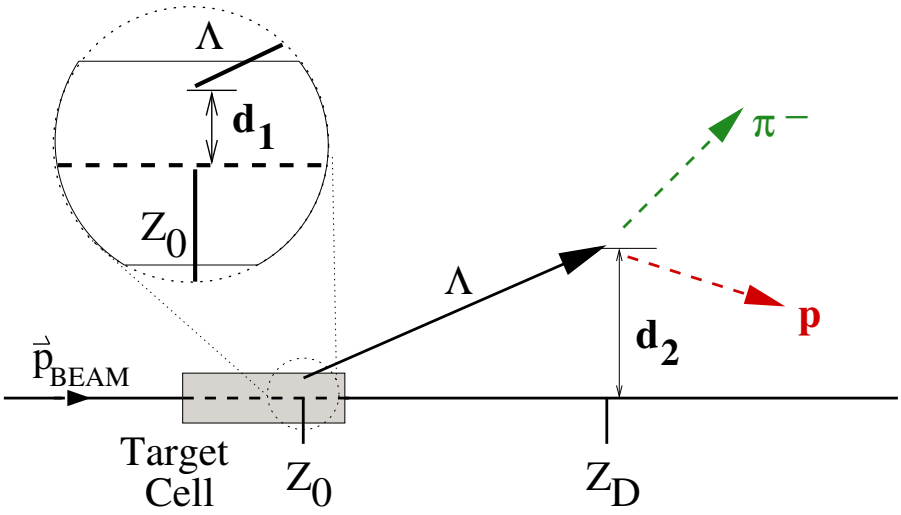

Figure 5.1: Figure (not shown to scale) depicting the various vertex and distances used in some of the cuts.

half). Finally, the $x - axis$ is defined to make a regular right handed coordinate system. Please note that this coordinate system is not the same as that used to define the polarization axes of the Λ.

Furthermore, a picture to reference the different vertices and distances involved in the cuts will hopefully clarify the geometry of some of the cuts used. Such a picture can be found Figure 5.1.

5.1.1 Cuts Common to both Q^2 Regimes

This section will list the cuts that are common to both the photoproduction and the semi-inclusive deep inelastic scattering regime. These cuts are as follows.

- PID cuts (for a description of PID, see Section 2.4).
  - hadron identification requires that the $PID3 + 5 < pid\_cut\_hadron = -1$
  - lepton identification requires that the $PID3 + 5 > pid\_cut\_lepton = 1$
- Burst cuts
  - Burst list mask of 0x0208138C (see Section A.2)

- Require the energy of the positron beam to be 27.57 GeV for the burst to ensure that the polarization of the Λ is being calculated for the same kinematic region.
- Bursts where the spin of the target flips, denoted as split bursts, are skipped since the data quality of each spin state can be different and the hanna code used for the analysis has trouble differentiating between the "sub"-bursts of each split burst in a convenient fashion.

- RICH cuts (long tracks only)
  - $RICH\_pid = 3$ is identified as a pion.
  - $RICH\_pid = 5$ is identified as a proton.
  - $RICH\_pid = 4$ is generally identified as a kaon at HERMES. However, since there is an issue with RICH misidentification of kaons and protons, it is assumed that this particle is also a proton. This is usually accompanied with an extra vertex cut (of 10 cm for Λ's and 20 cm for $\bar{\Lambda}$'s), but with the addition of a vertex cut over all tracks, it becomes unnecessary to make an additional cut in this particular case.
  - All protons must be long tracks.
  - Must have both a proton and a π^- (long or short) to continue.

- Non-RICH cuts (long tracks only)
  - For the 96 and 97 production years, the RICH was not installed. As such, the original intent in the Λ analysis was to use the Ĉerenkov detector as a pion rejector and an extra vertex cut (of 10 cm for Λ's and 20 cm for $\bar{\Lambda}$'s) was made, similar to the case of the RICH for the case of $RICH\_pid = 4$. As in that case, this cut is not needed specifically for the 96 and 97 years since a vertex cut has been placed in all tracks making this cut irrelevant.

- The protons shouldn't fire the Ĉerenkov detector. Thus, if smTrack.rCer < 0.25 GeV and the charge is positive, then a particle is labeled a proton.
- Regardless of the Ĉerenkov firing or not, a negatively charged particle is assumed to be a π^-.

- Short track cuts
  - All short tracks are assumed to be pions.
  - Short track correction needed to correct for error in HRC for short tracks

    For $0.2 < p_\pi < 2.1$ GeV:

$$\theta_x^{NEW} = \theta_x^{OLD} \pm (0.0087376 - 0.0099544 p_\pi + 0.0041928 p_\pi^2) \tag{5.1}$$

    For $2.1 < p_\pi < 2.4$ GeV:

$$\theta_x^{NEW} = \theta_x^{OLD} \pm (0.0073616 - 0.0030936 p_\pi) \tag{5.2}$$

    where the "+" sign is used for the $\bar{\Lambda}$ and the "$-$" sign is used for the Λ.
  - Ghost track identification. A "ghost" track is a short track in which the HRC has taken one actual track and reconstructed it into two. It is not a common occurrence, but must be corrected for by eliminating any two tracks that satisfy the following conditions:
    - The difference in the x-offset at $z = 0$ for each track is ≤ 0.0001 cm **OR**
    - differences in: the momentum of each track is ≤ 0.1, theta of each track is ≤ 0.3, AND phi of each track is ≤ 0.03 **OR**
    - differences in: the momentum of each track is ≤ 0.75, theta of each track is ≤ 0.03, AND phi of each track is ≤ 0.005.
  - $p_\pi > 0.45$ GeV.

- $p_\pi > 0.60$ GeV for long tracks.
- $p_\Lambda > 0.2$ GeV.
- Fiducial volume cuts
  - For short and long tracks, a track must satisfy:
    * $\mid x_{Off} + 172 \tan\theta_x \mid < 31$ cm **AND**
    * $\mid y_{Off} + 181 \tan\theta_y \mid > 7$ cm **AND**
    * $\mid y_{Off} + 383 \tan\theta_y \mid < 54$ cm **AND**
    * passes fiducial volume cut built into the udst production; the additional cuts listed here are stricter cuts brought about during the HERMES pentaquark analysis. This cut should only affect long tracks, but is included for both.

    where the x/y_{Off} refers to the x/y offset at $z = 0$ cm and $\theta_i = p_i/p_z$.
  - Additional fiducial volume cuts for long tracks only
    * $\mid x_{pos} + 108 x_{slope} \mid \leq 100$ cm **AND**
    * $\mid y_{pos} + 108 y_{slope} \mid \leq 54$ cm **AND**
    * $\mid y_{pos} + 463 y_{slope} \mid \leq 108$ cm.

    where the x/y_{pos} refers to the x/y offset at the center of the magnet and the x/y_{slope} refers to the x/y slope at the center of the magnet.
- Other cuts
  - The proton momentum must be greater than the pion momentum.
  - The proton and pion track separation must not be greater than 1.5 cm at the distance of closest approach. The midpoint of the line connecting the pion and proton tracks at this distance of closest approach is identified as the z component of the Λ decay vertex, Z_D.

- -18 cm $< Z_D <$ 130 cm. After 130 cm there is a drop in the number of Λ's found in the spectrometer.
- The z component of the production vertex for the Λ, Z_0, must satisfy -18 cm $< Z_0 <$ 25 cm to insure that the Λ is produced in the target cell.
- A track is considered to be in the top half of the spectrometer if the y component of its momentum is positive, i. e. $p_y > 0$. Likewise, a track is considered to be in the bottom half of the spectrometer if $p_y < 0$.
- Both the pion and proton tracks are required to be "horizontal" tracks. This simply means that both tracks occur in the same half of the spectrometer and is used to be extra cautious against misalignments in the top and bottom half of the spectrometer.
- the Λ mass spectrum is fit with a Gaussian plus a second order polynomial. To avoid skewing the true Λ signal from that of the background sidebands, this fit is done in the mass region from 1.1 GeV to 1.4 GeV only.
- The background cosine moment is determined from four side bands of width 6σ where σ is taken from the Gaussian fit. There are two sidebands used to either side of the central mass bin centered on the Λ peak taken from the Gaussian fit. To determine the value of the background in the central mass bin, a linear fit to the four sideband mass bins is taken and extrapolated to the central bin. This will be covered in better detail later when the data is examined.

5.1.2 Cuts Exclusive to the Photoproduction Regime

These cuts are used in the photoproduction regime mainly due to the fact that there is no measured scattered lepton such that we are missing information such as the Λ production vertex and $\vec{Q}$. However, there are greater statistics for Λ's in the case of photoproduction (as compared to SIDIS) so that the vertex cuts will not significantly affect the end result.

The z component of the production vertex for the Λ is usually take to be the distance along the $z - axis$ at which the scattered lepton crosses the beam axis. However, since there is no scattered lepton information in photoproduction, the production vertex must be determined by using the distance of closest approach between the Λ trajectory (determined from the Λ momentum and the decay vertex of the Λ) and the beam axis.

There are two other separations that are used in the cuts. The first is labeled d_1. This is the distance of the reconstructed production vertex from the beam axis, i. e. the actual distance of closest approach of the Λ track from the beam axis. The second separation of interest is d_2. This is the distance of closest approach from the beam axis to the decay vertex.

With all the aforementioned definitions of the separations and vertices, the following are the cuts exclusive to photoproduction:

- $Z_0 < Z_d$; this requires that the decay of the Λ happen downstream of the Λ production. This cut is necessitated by the fact that the reconstruction of the production vertex using the distance of closest approach does sometimes reconstruct the production vertex after the decay vertex and is merely a consequence of the geometry of the situation. In these cases, the reconstructed production vertex information should not be trusted.

- $d_1 < 1$ cm to ensure that the production vertex is in the target cell.

- $d_2 > 1$ cm to ensure that the decay happens outside the target cell region.

- $d_2 < 18$ cm since Λ's beyond this point may have bad reconstruction.

- $Z_D - Z_0 > 15$ cm is a type of "lifetime" cut (Λ is long lived as a weakly decaying particle). For more details, please see Section A.3 of the Appendix.

The bins used in the Λ polarization analysis for photoproduction are as follows:

- For the P_Λ vs. ζ plot ($0.2 < p_T \leq 3.0$GeV):

  $0.0 < \zeta < 0.164$, $0.164 < \zeta < 0.206$, $0.206 < \zeta < 0.245$, $0.245 < \zeta < 0.3$, $0.3 < \zeta < 0.38$, and $0.38 < \zeta < 1.0$.

- For the P_Λ vs. p_T plots ($0.0 < \zeta < 0.25$):

  $0.2 < p_T \leq 0.34$, $0.34 < p_T \leq 0.48$, $0.48 < p_T \leq 0.664$, $0.664 < p_T \leq 0.82$, and $0.82 < p_T \leq 3.0$ GeV.

- For the P_Λ vs. p_T plots ($0.25 < \zeta < 1.0$):

  $0.2 < p_T \leq 0.52$, $0.52 < p_T \leq 0.71$, $0.71 < p_T \leq 1.0$, and $1.0 < p_T \leq 3.0$ GeV.

The bins used in the $\bar{\Lambda}$ polarization analysis for photoproduction are as follows:

- For the P_Λ vs. ζ plot ($0.2 < p_T \leq 3.0$GeV):

  $0.0 < \zeta < 0.181$, $0.181 < \zeta < 0.241$, $0.241 < \zeta < 0.32$, and $0.32 < \zeta < 1.0$.

- For the P_Λ vs. p_T plots ($0.0 < \zeta < 0.25$):

  $0.2 < p_T \leq 0.453$ and $0.453 < p_T \leq 3.0$ GeV.

- For the P_Λ vs. p_T plots ($0.25 < \zeta < 1.0$):

  $0.2 < p_T \leq 0.739$ and $0.739 < p_T \leq 3.0$ GeV.

The bins used in the Λ polarization analysis for SIDIS are as follows:

- For the P_Λ vs. x_F plot ($0.2 < p_T \leq 3.0$GeV):

  $0.0 < x_F < 0.65$ and $0.65 < x_F < 1.0$

- For the P_Λ vs. p_T plot ($x_F > 0$):

  $0.2 < p_T \leq 0.38$ and $0.38 < p_T \leq 3.0$ GeV.

5.1.3 Cuts Exclusive to the SIDIS Regime

There are also a set of cuts exclusive to the semi-inclusive deep inelastic scattering regime. These cuts are made possible by the measurement of the scattered positron beam. These cuts are as follows:

- require the scattered lepton to be identified in the spectrometer.
- $1 < Q^2 < 24$ GeV^2
- $W^2 > 4$ GeV^2 where W^2 is the square of the missing mass of the proton-lepton system.
- $y = \nu / E_{Beam} < 0.85$ to avoid radiative corrections (where ν is the energy of the q four vector and E_{Beam} is the energy of the lepton beam, 27.57 GeV).
- Trigger 21 in the data is present.
- Energy deposited in the calorimeter for the lepton ¿ 4.0 GeV
- $-18 < Z_0 < 20$ cm
- d_1 ¡ 0.75 cm
- require the angle of the cosine between the Λ momentum vector and the vector connecting the Λ production vertex to the Λ decay vertex to be greater than 0.9995. This is known as a "collinearity" cut.

Due to the collinearity cut, no vertex cut was used. This helps to keep the statistics in the small SIDIS data set for these production years.

5.1.4 Brief Mention of the K^0_S and Related Cuts

The K^0 particle is another particle that, like the Λ, is produced by a strong interaction, and, also like the Λ, decays via a weak interaction. However, the K^0 has a dual nature when it comes to its decay modes:

- $K^0_S \rightarrow 2\pi$; $\tau = 0.9 \times 10^{-10}$ sec.
- $K^0_L \rightarrow 3\pi$; $\tau = 0.5 \times 10^{-7}$ sec.

The K^0_S is interesting for two reasons. First, one can use its decay products to simulate the response of a Λ in the spectrometer. Second, and most important, is that that the K^0_S is a spin zero particle. Any measurement of the spin of the K^0_S must result in zero. Any deviation from zero can be used as an estimate of the systematic error of the Λ polarization.

Most of the cuts for the $K^0_S \rightarrow 2\pi$ are the same as those for the Λ listed in the previous subsection. However, there are a couple more to note:

- Both a π^+ and a π^- are now required to be found in the event. The π^+ simply takes the place of the proton in the aforementioned cuts.
- Although there could be short track π^+'s in an event, to keep the result consistent with that of the Λ, only LONG track π^+'s should be used to determine the polarization of the K^0_S. These are what are referred to as Λ-like K^0_S's.
- For non-RICH production years, any positively charged particle is assumed to be a π^+.

5.2 Mass Peaks for Both Inclusive and Semi-inclusive Regions

Another nice feature of the weak decay of the Λ is that it's lifetime is long compared to other types of decay processes. This means that the reconstructed Λ mass peak should be relatively narrow (the width being the result of the spectrometer resolution). It is important to obtain a nice fit to the Λ in order to get an estimate of the background signal to the true Λ signal. As mentioned earlier in the chapter, a Gaussian plus a second order polynomial fit was applied to the Λ mass peak. The results for a sample bin of data is shown in Figure 5.2 for

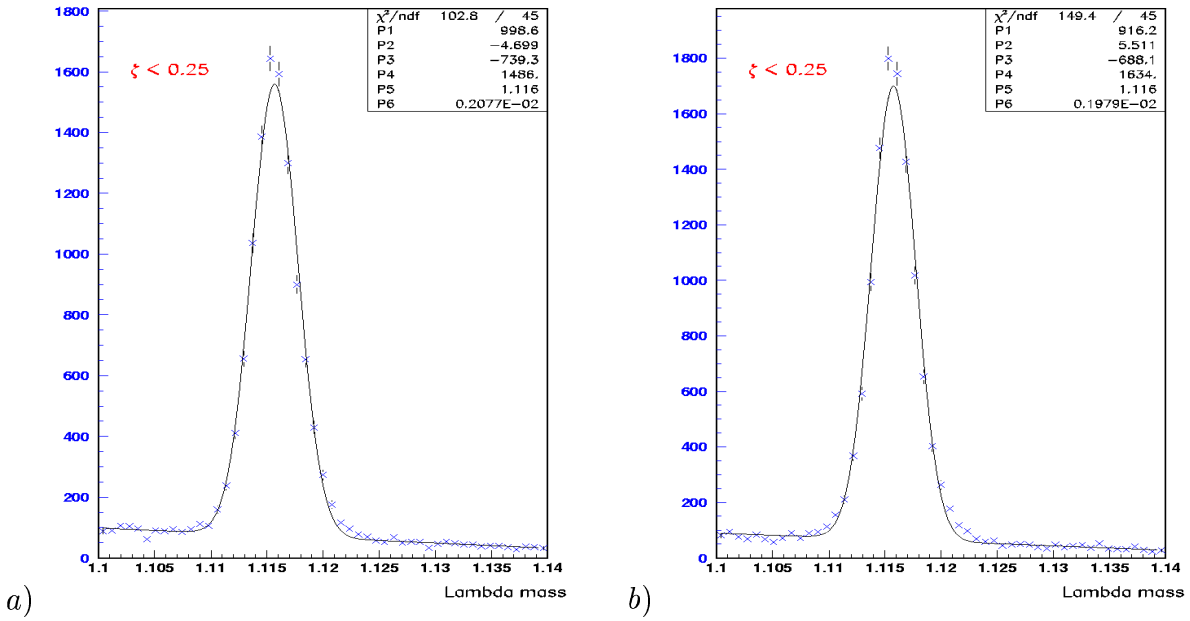

a) *b)*

Figure 5.2: Gaussian plus second order polynomial fit to the Λ mass peak for a) the top and b) the bottom half of the spectrometer. The selected bin is $0 < \zeta < 0.25$ and $0.48 < p_T \leq 0.664$ GeV and these are short tracks only.

both the top and bottom halves of the spectrometer in the case of the Λ in photoproduction. A sample mass peak can be seen for the top and bottom halves of the spectrometer for the K^0_S (Figure 5.3), $\bar{\Lambda}$ (Figure 5.4), and $\bar{K^0_S}$ (Figure 5.5) in the case of photoproduction. In all these cases, only the short tracks are shown, but the long tracks are similar. Also, the mass peaks in the case of semi-inclusive deep inelastic scattering for the Λ (Figure 5.6) and the K^0_S are shown as well (Figure 5.7). These peaks are done for every bin used in this study and separately for the top and the bottom halves of the spectrometer.

From the Gaussian fits to these mass peaks, one obtains a value σ, the width of the peak, and a value upon which the peak is centered, i. e. the best value of the Λ mass. The mass regions in each of the plots are split into five regions centered about the mass peak, each of width 6σ. Thus, there is the central mass bin $[peak - 3\sigma, peak + 3\sigma]$, and four side bins, two to each side of the central mass bin. These side bins will be helpful in determining the background contribution to the Λ, as will be seen in the next section.

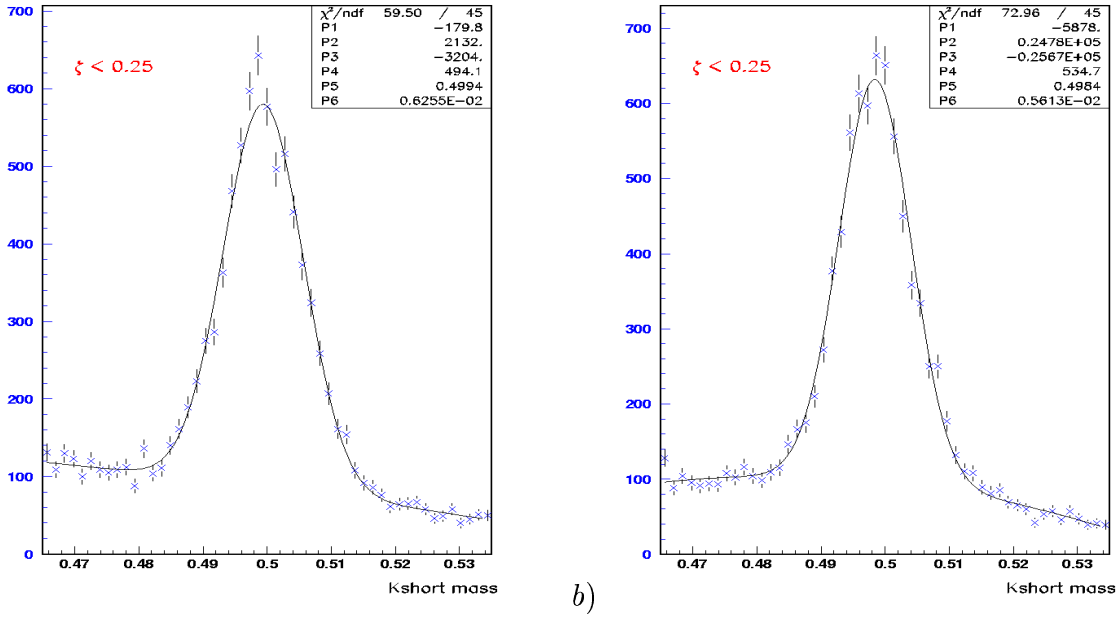

a) *b)*

Figure 5.3: Gaussian plus second order polynomial fit to the K^0_S mass peak for a) the top and b) the bottom half of the spectrometer. The selected bin is $0 < \zeta < 0.25$ and $0.48 < p_T \leq 0.664$ GeV and these are short tracks only.

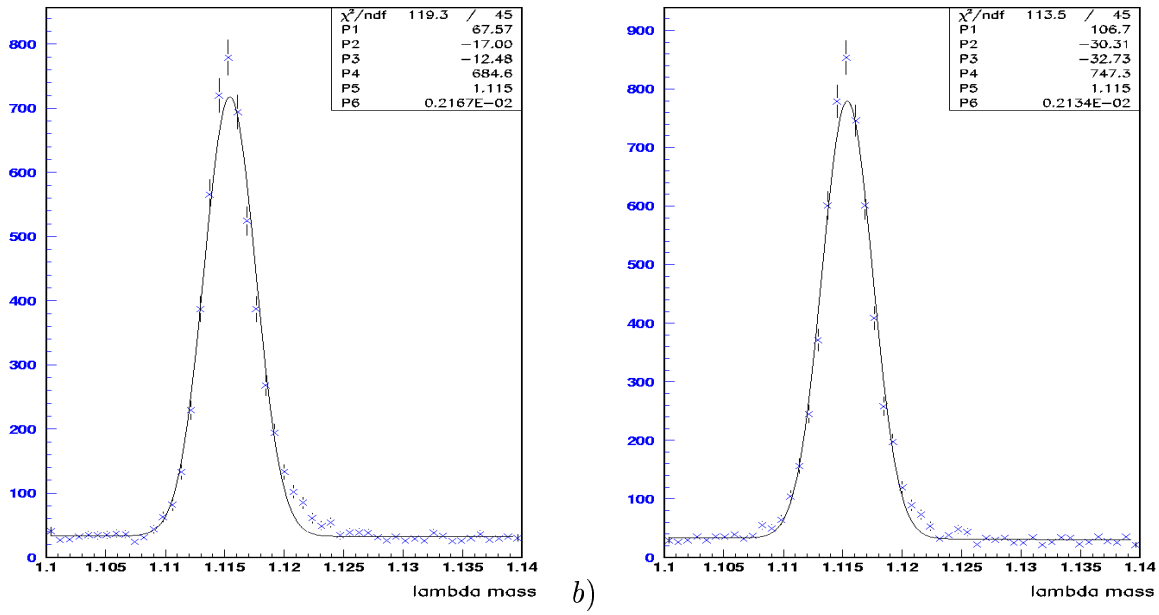

a) *b)*

Figure 5.4: Gaussian plus second order polynomial fit to the $\bar{\Lambda}$ mass peak for a) the top and b) the bottom half of the spectrometer. The selected bin is $0.241 < \zeta < 0.32$ and $0.2 < p_T \leq 3.00$ GeV and these are long tracks only.

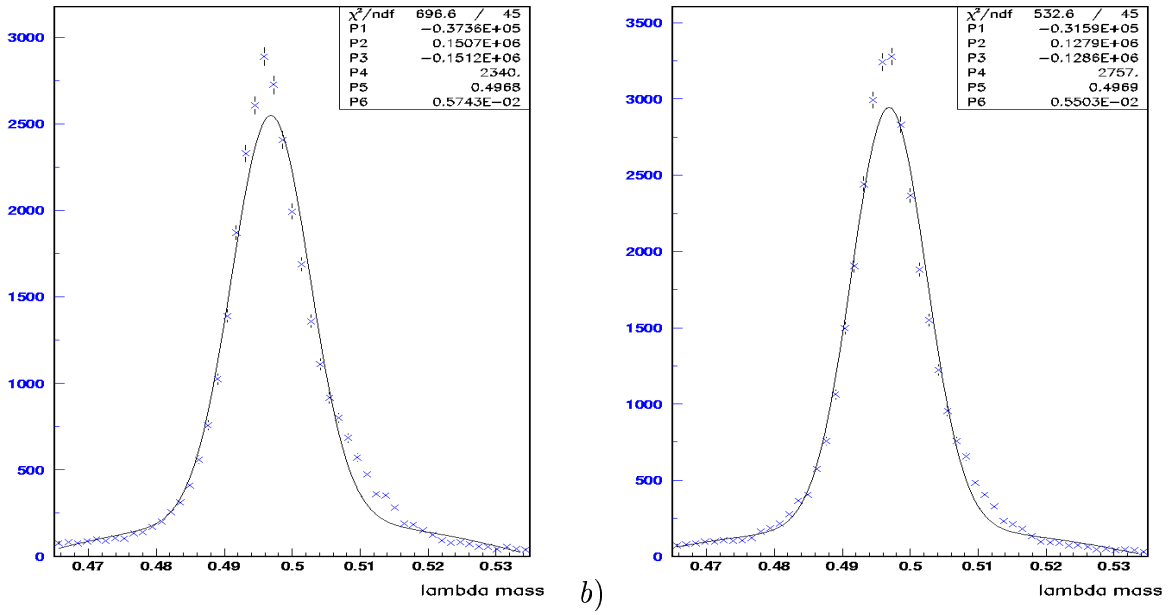

a) *b)*

Figure 5.5: Gaussian plus second order polynomial fit to the $\bar{K}^0_S$ mass peak for a) the top and b) the bottom half of the spectrometer. The selected bin is $0.241 < \zeta < 0.32$ and $0.2 < p_T \leq 3.00$ GeV and these are long tracks only.

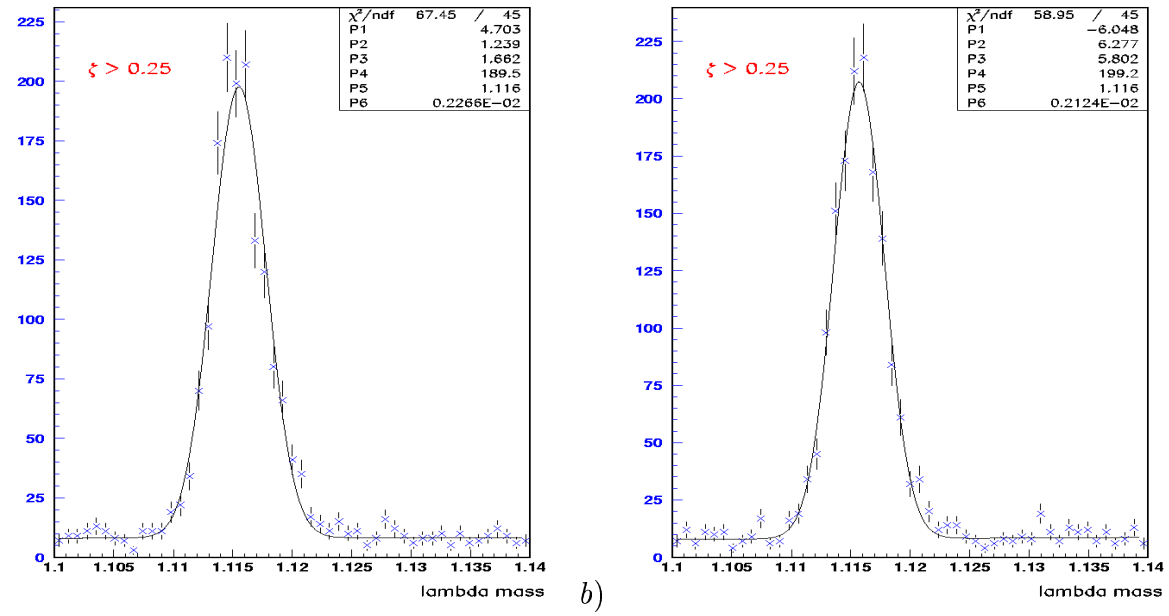

a) *b)*

Figure 5.6: Gaussian plus second order polynomial fit to the Λ mass peak (SIDIS) for a) the top and b) the bottom half of the spectrometer. The selected bin is $0.0 < x_F < 1.00$ and $0.38 < p_T \leq 3.00$ GeV and these are long tracks only.

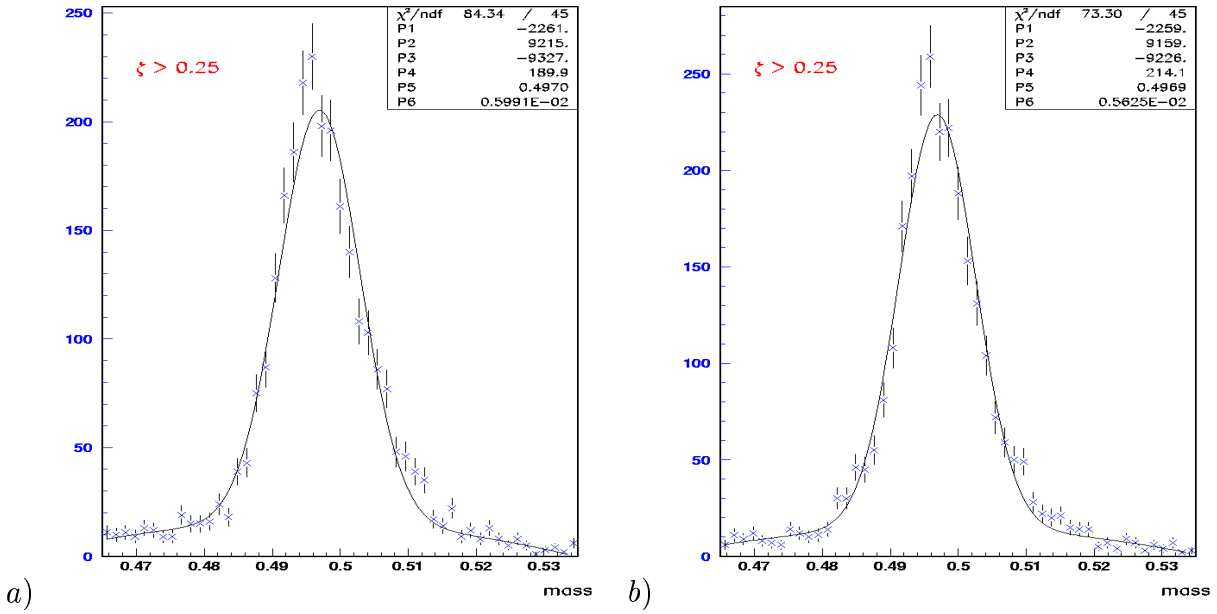

Figure 5.7: Gaussian plus second order polynomial fit to the K^0_S mass peak (SIDIS)for a) the top and b) the bottom half of the spectrometer. The selected bin is $0.0 < x_F < 1.00$ and $0.38 < p_T \leq 3.00$ GeV and these are long tracks only.

5.3 Background Subtraction Procedure

The presence of background in the data was an unfortunate necessity. Had the vertex cut been increased, or other cuts intensified, then the Λ signal would have been reduced too much. However, a background subtraction procedure was used to correct for any influence this background may have had on the polarization.

The central mass region has both true Λ events and background events, while the sidebands are mostly, if not all, background events. The cosine moments in the sidebands are fit with a first order polynomial and the value of the fit at the Λ mass peak is take to be the value of the corresponding background cosine moment in the central mass bin. The formula for the *true* cosine moment is then

$$< \cos^n \theta >_{True} \quad = \quad < \cos^n \theta >_{Meas} - \beta < \cos^n \theta >_{BG} \tag{5.3}$$

where $n = 1, 2$ refers to the first or second cosine moment, $< \cos^n \theta >_{True}$ is the true cosine moment, $< \cos^n \theta >_{Meas}$ is the measured cosine moment (Equation 3.16), $< \cos^n \theta >_{BG}$ is

the extrapolated background cosine moment, and β is the ratio of the background number of events in the central mass region (found by integrating the fitted polynomial) to the true number of background events in the central mass region (found by integrating the fitted Gaussian). An example plot of the cosine moments is shown in Figure 5.8.

To see the values of the background fits, measured cosine moments, and background cosine moments, please see the tables in Section C of the Appendix. This includes an extensive set of tables for all the data and Monte Carlo used for the final results, the next section of this thesis.

5.4 The Final Results

The final results are presented with both a statistical and systematic error for each bin. In the case of the inclusive Λ, the systematic error is a combination of the measured polarization of the Monte Carlo results from Chapter 4 and the results from $K^0_S/\bar{K^0_S}$. For the $\bar{\Lambda}$ polarization, the Monte Carlo values from the Λ studies are used, but are rebinned to match the bins used in the $\bar{\Lambda}$ studies. The main contribution to the systematic error is from the K^0_S, as seen in the case of the inclusive Λ systematic error in Figure 5.9 and in the case of the inclusive $\bar{\Lambda}$ systematic error in Figure 5.10. Taking the central value of the K^0_S will likely result in overestimating the systematic error, but it will be a worst case estimate. The statistical error is represented by the error bar up to the horizontal mark. The rest of the error bar represents the total statistical and systematic error combined.

The final results for the inclusive Λ are shown in Figure 5.11 for long and short tracks separately and Figure 5.12 for the both long and short tracks together. The systematic error estimate due to the Monte Carlo was chosen somewhat arbitrarily from the available Monte Carlo polarization values based on the Λ polarization values as follows:

- use $P_{MC} = 0$ if $\mid P_\Lambda \mid < 0.025$;

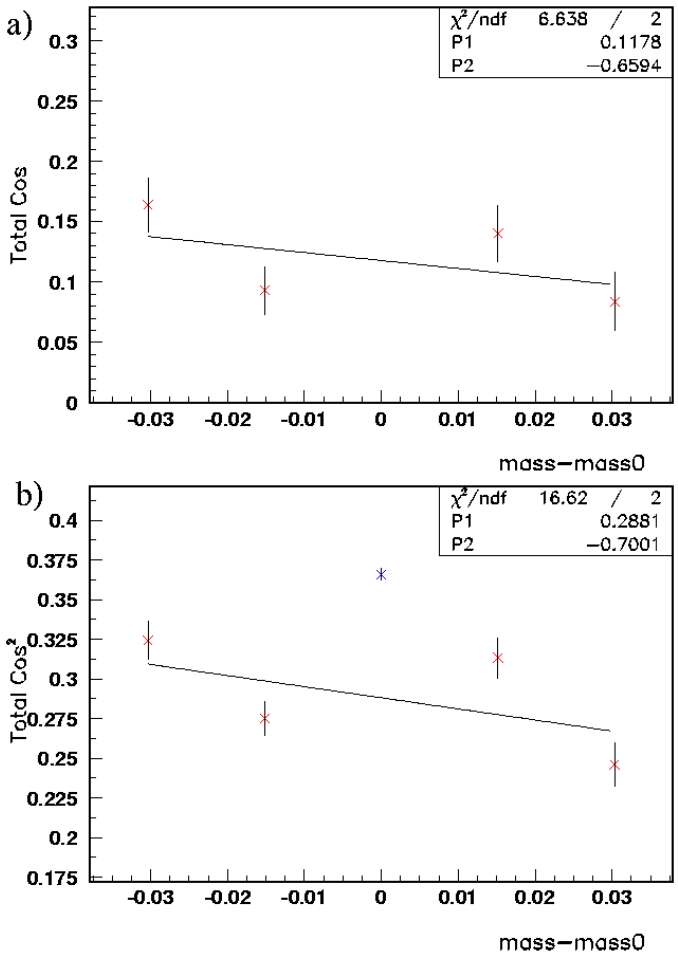

Figure 5.8: Sample a) first and b) second cosine moments versus the Λ mass minus the value of the peak Λ mass in each of the five bins mentioned in the text and the fit to the four side bins in the case of the inclusive Λ. Plotted in this fashion, the y-intercept gives the value of the background polarization The fit is for the kinematic region $0.25 < \zeta < 1$ and $x.xxx < p_T < x.xxx$, long tracks, and the top half of the spectrometer.

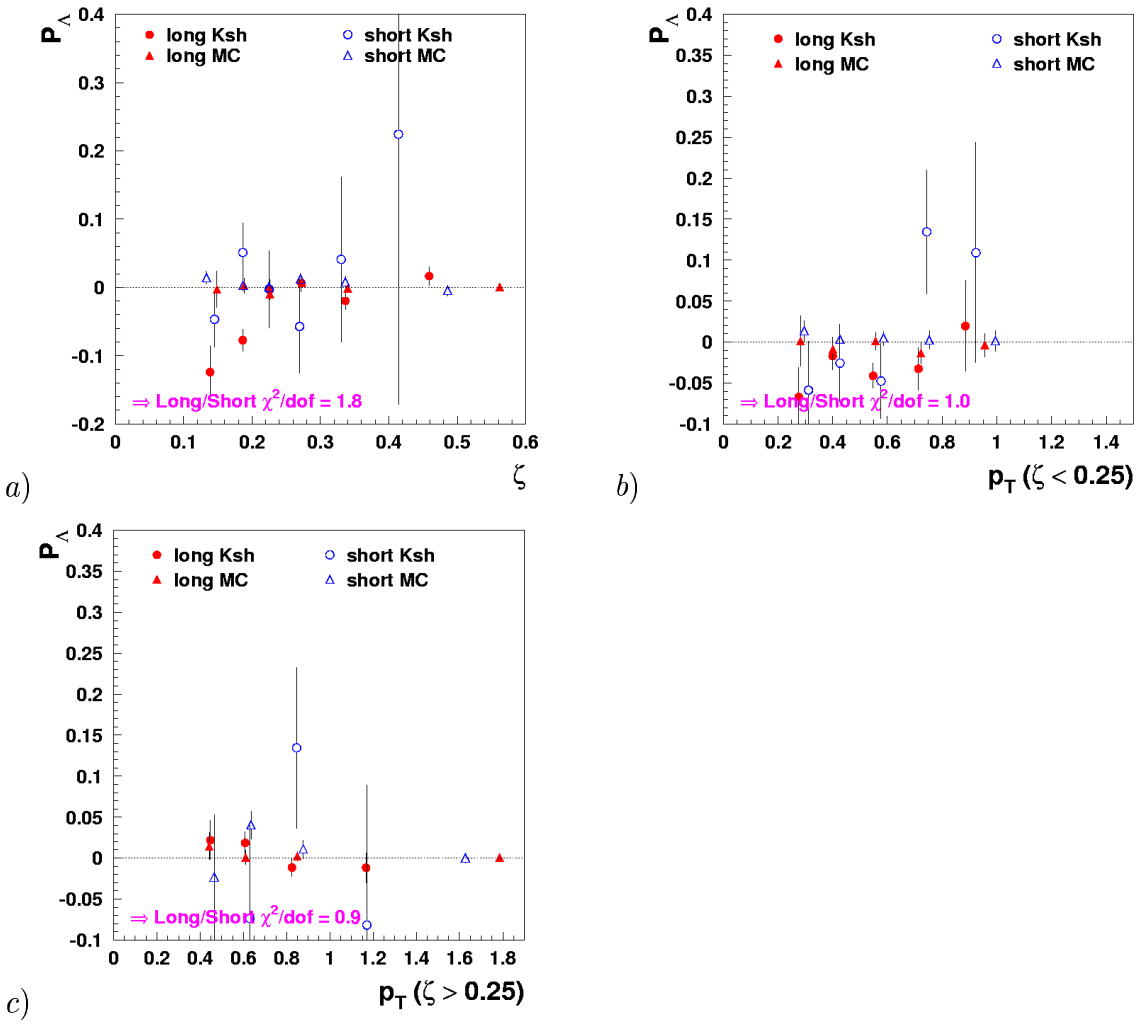

Figure 5.9: P_{Ks} and P_{MC} vs. a) ζ, b) p_T ($\zeta < 0.25$), and c)p_T ($\zeta > 0.25$).

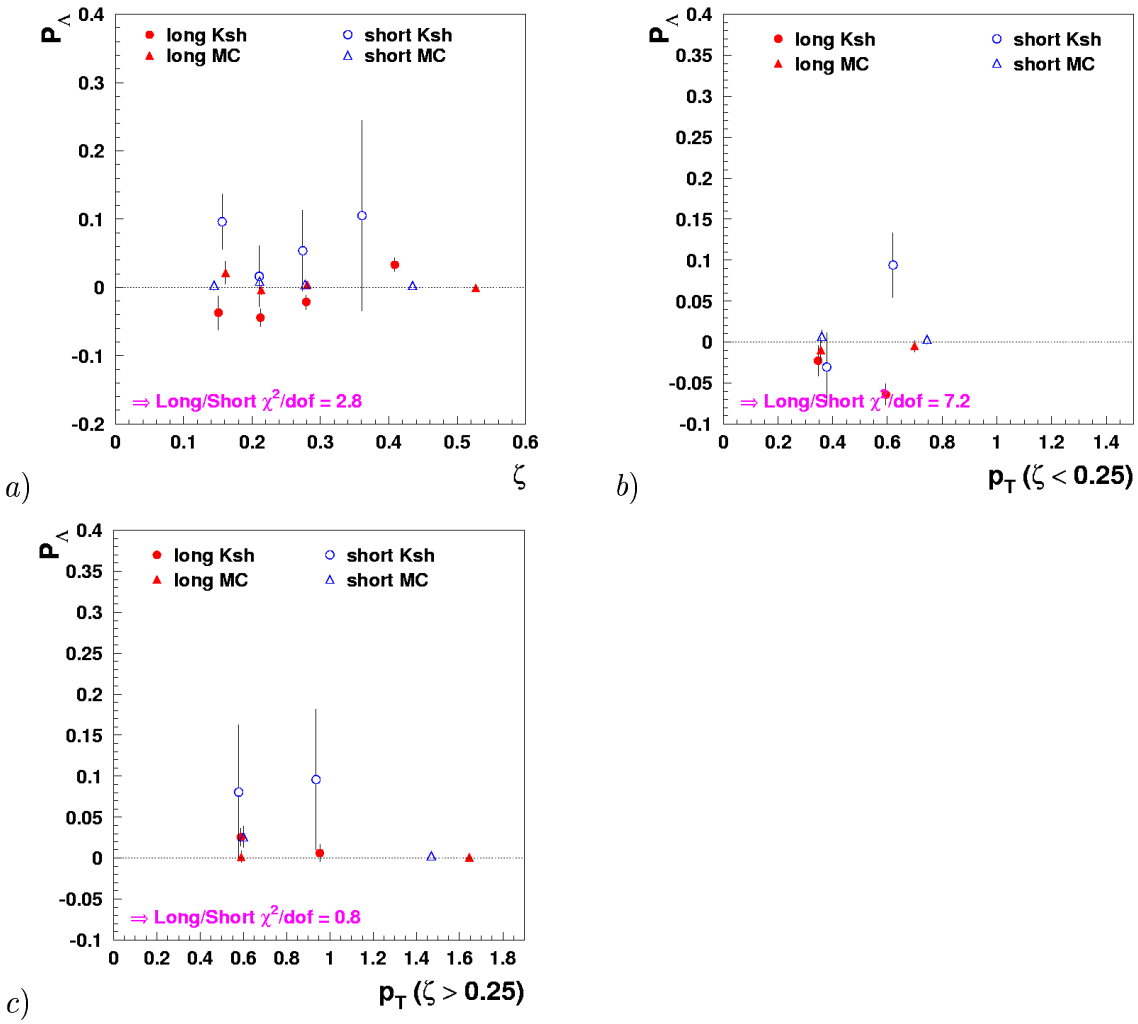

Figure 5.10: $P_{\bar{K}s}$ and P_{MC} vs. a) ζ, b) p_T ($\zeta < 0.25$), and c)p_T ($\zeta > 0.25$).

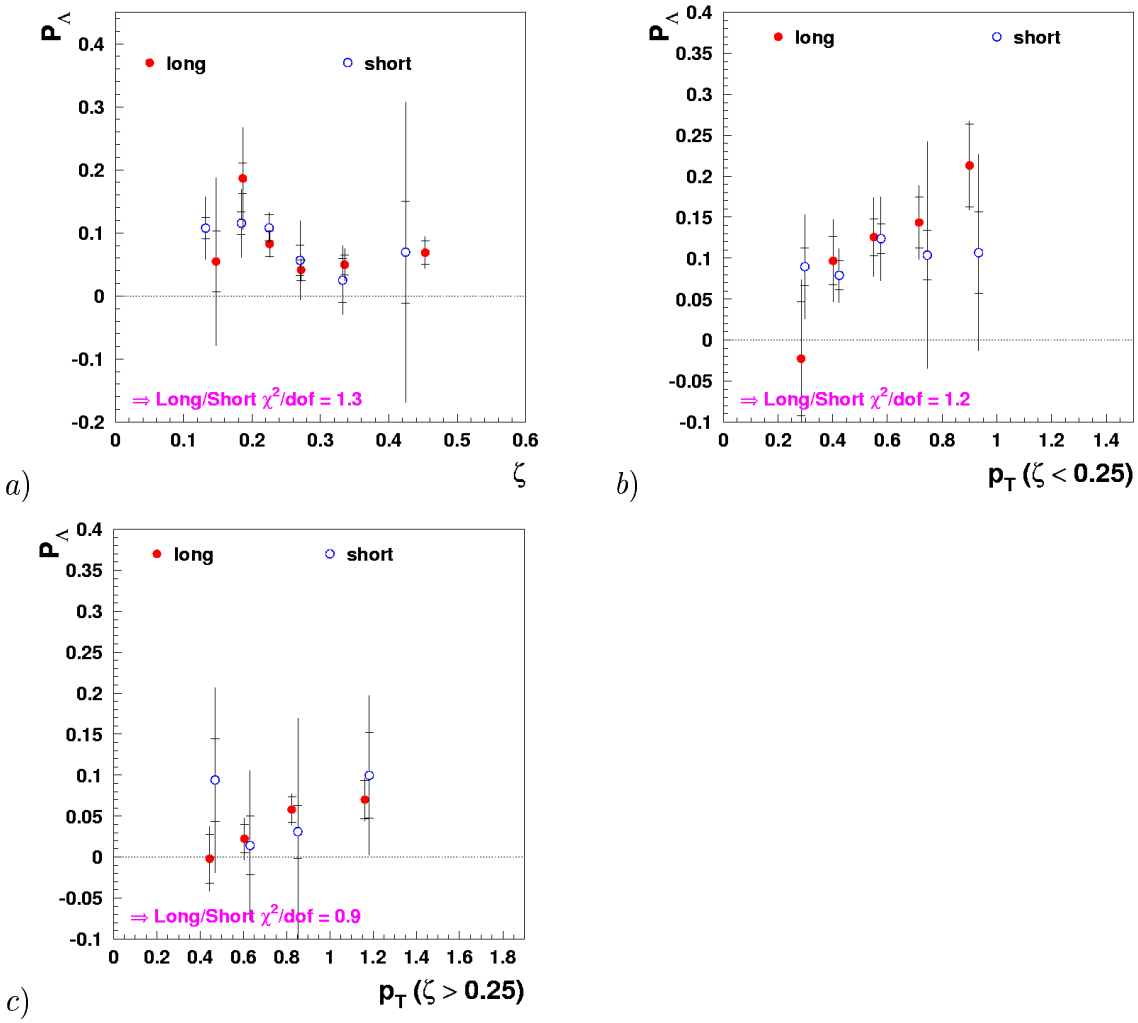

Figure 5.11: P_Λ vs. a) ζ, b) p_T ($\zeta < 0.25$), and c)p_T ($\zeta > 0.25$) for long and short tracks.

- use $P_{MC} = 5$ if $\mid P_\Lambda \mid < 0.075$;
- use $P_{MC} = 10$ if $\mid P_\Lambda \mid < 0.16$;
- use $P_{MC} = 20$, otherwise.

The final results for the inclusive $\bar{\Lambda}$ are shown in Figure 5.13 for long and short tracks separately and in Figure 5.14 for both long and short tracks averaged together. The systematic error estimate due to the Monte Carlo was also chosen somewhat arbitrarily from the available Monte Carlo polarization values based on the $\bar{\Lambda}$ polarization values as follows:

- use $P_{MC} = 0$ if $\mid P_{\bar{\Lambda}} \mid < 0.03$;

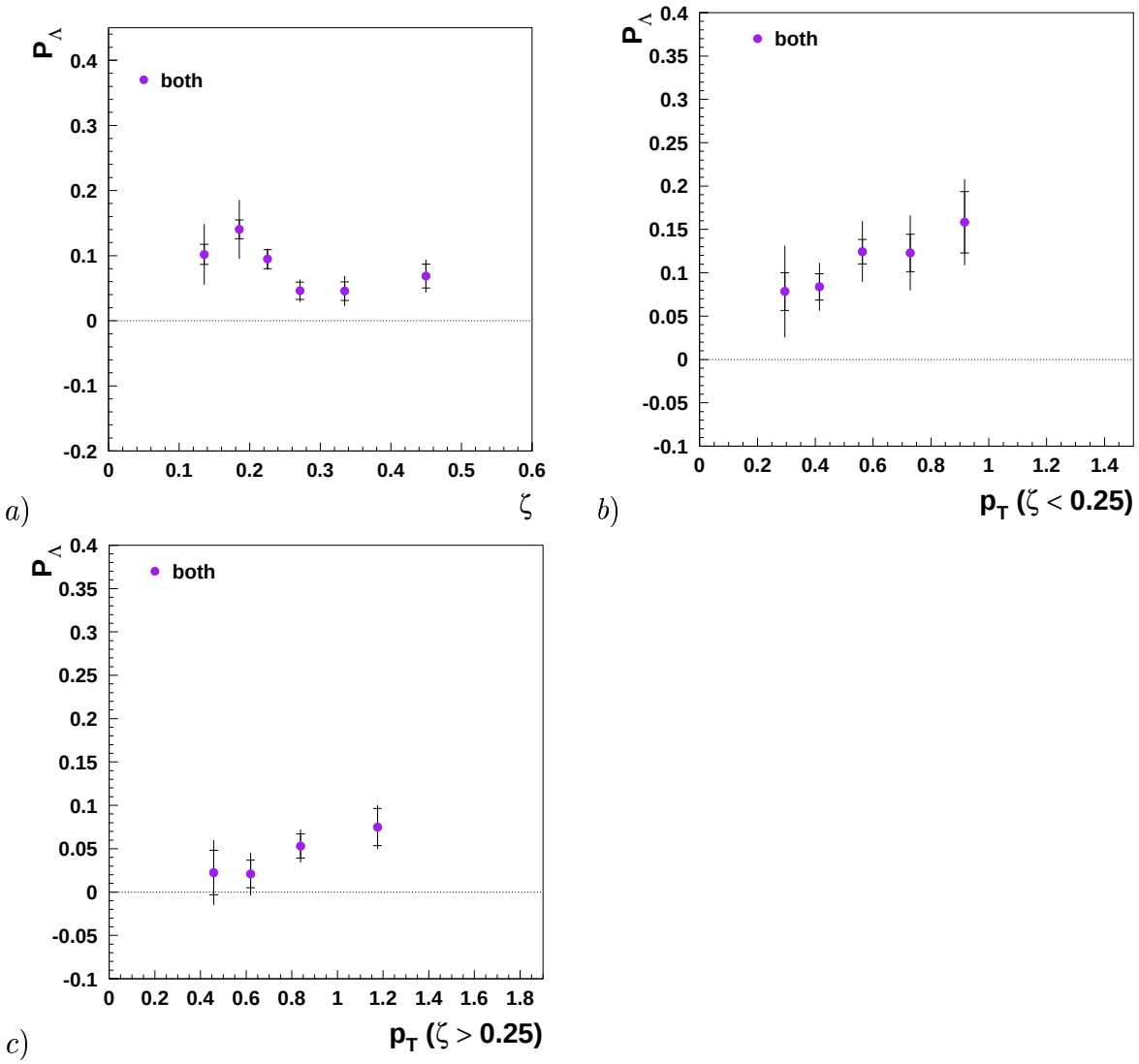

Figure 5.12: P_Λ vs. a) ζ, b) p_T ($\zeta < 0.25$), and c)p_T ($\zeta > 0.25$) for both tracks together.

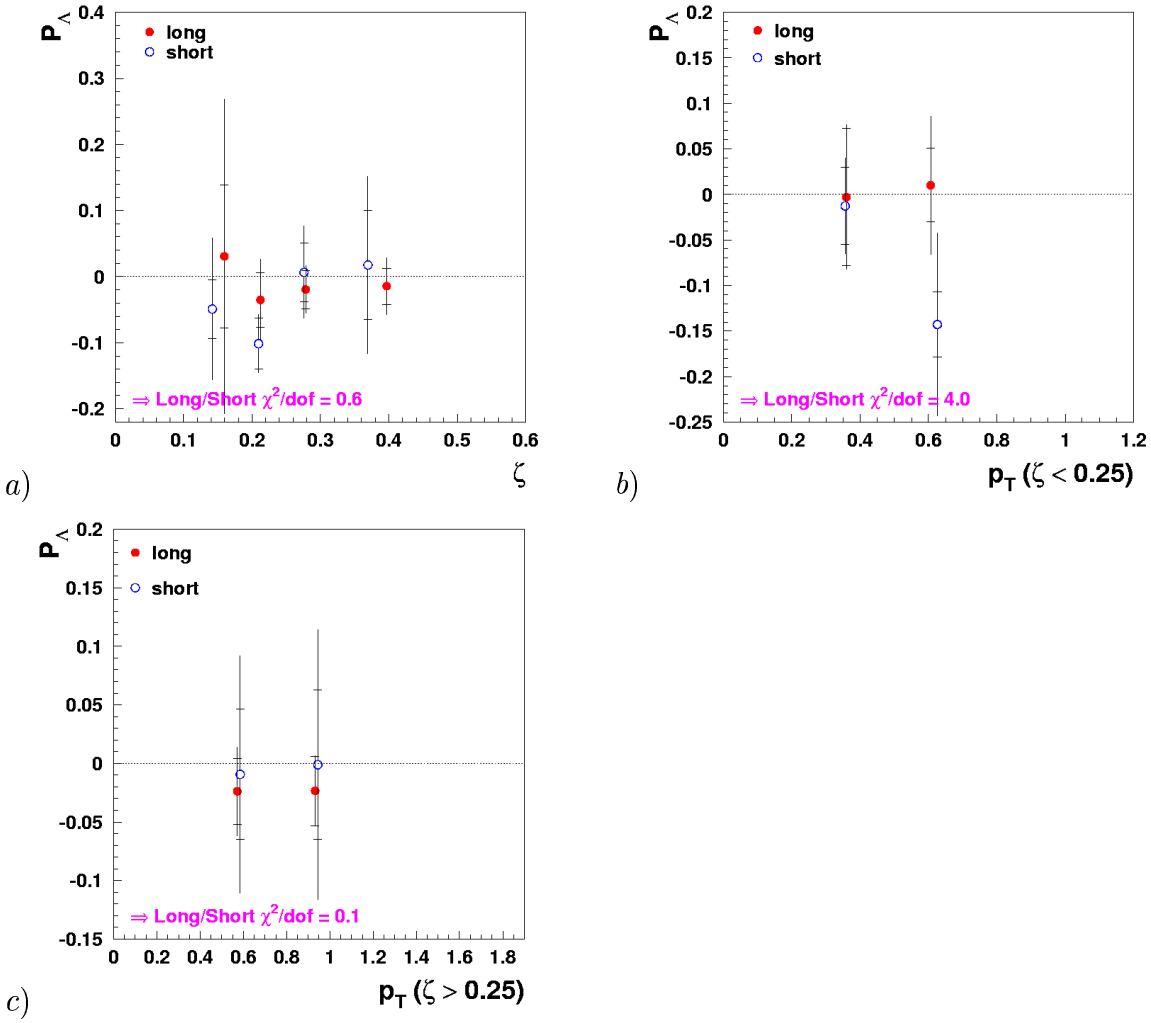

Figure 5.13: $P_{\bar{\Lambda}}$ vs. a) ζ, b) p_T ($\zeta < 0.25$), and c)p_T ($\zeta > 0.25$) for long and short tracks separately.

- use $P_{MC} = 10$, otherwise;

The choice of $P_{MC} > 0$ was really only needed for the one short track bin, so this is less arbitrary than it may seem.

The final results for the semi-inclusive Λ are shown in Figure 5.15 for long and short tracks separately and in Figure 5.16 for both long and short tracks averaged together. No Monte Carlo was done for the semi-inclusive case, but it is assumed that the systematic error from the semi-inclusive K^0_S will again be more than sufficient for a worst case scenario on the systematic error.

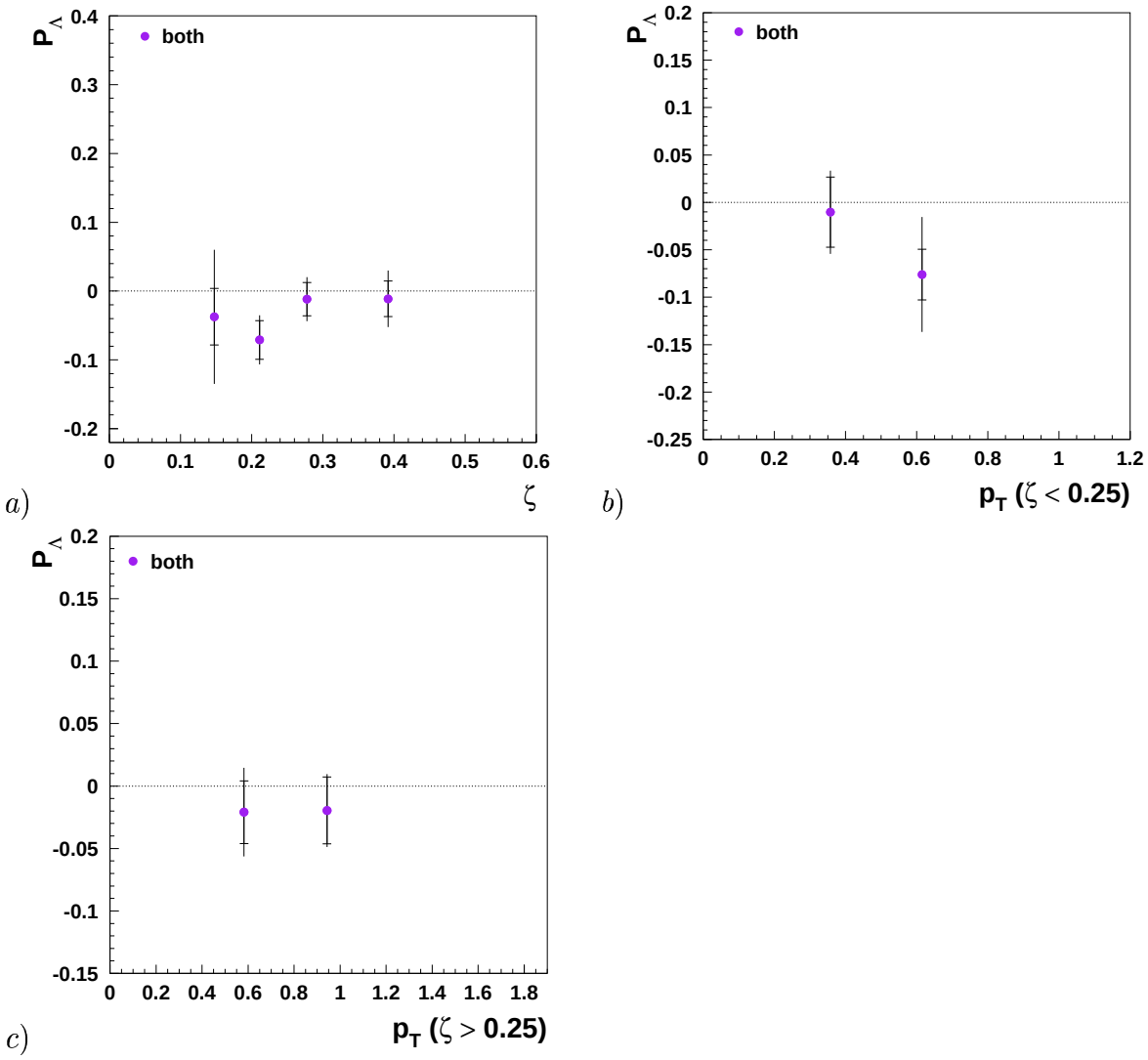

a) b) c)

Figure 5.14: $P_{\bar{\Lambda}}$ vs. a) ζ, b) p_T ($\zeta < 0.25$), and c)p_T ($\zeta > 0.25$) for both long and short tracks.

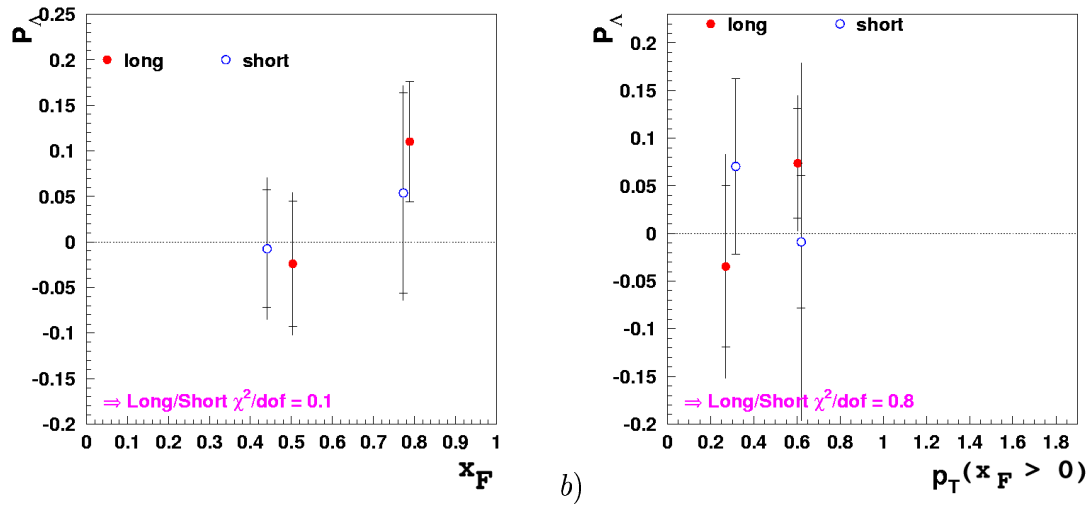

a) *b)*

Figure 5.15: P_Λ vs. a) x_F, b) p_T $(x_F > 0)$ for both long and short tracks separately.

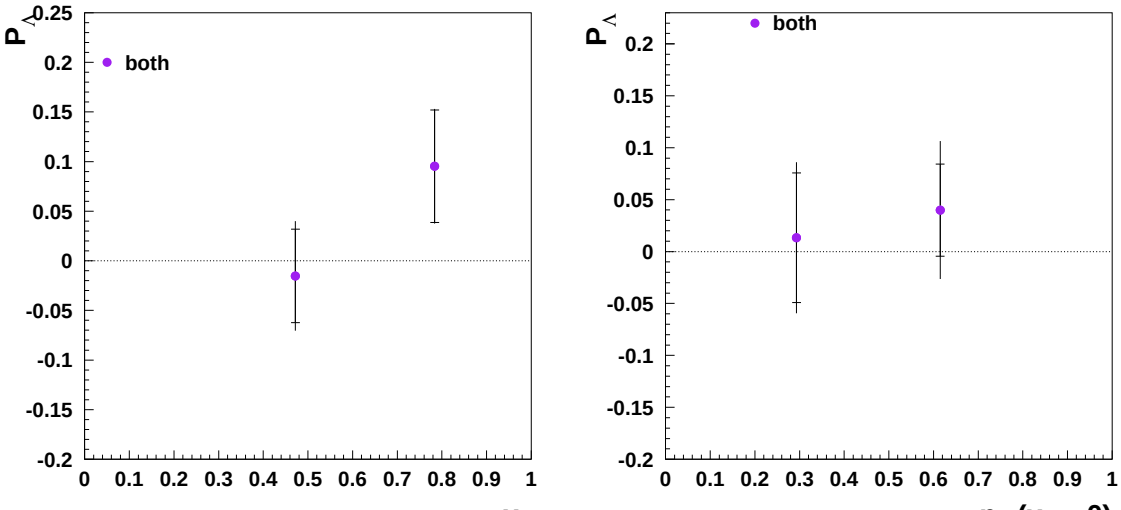

a) *b)*

Figure 5.16: P_Λ vs. a) x_F, b) p_T $(x_F > 0)$ for both long and short tracks averaged together.

Chapter 6

Conclusions

The spin polarization of the Λ particle has been studied at HERMES in both the inclusive and semi-inclusive regimes. The results seen in the last chapter are mostly encouraging, especially in the inclusive regime for the Λ. In the semi-inclusive, deep inelastic scattering regime, the statistics are not sufficient to make too powerful a statement, but the results are not surprising in light of what has been seen in other experiments. While there may be a trend towards an increasing, positive polarization with increasing x_F, it is hard to argue this with the huge error bars when looking at the polarization vs. p_T (for $x_F > 0$) since the result is also consistent with zero (although the central values guide the eye towards an increasing polarization with p_T) . At any rate, the results do not tend to lend support for the predictions given by Anselmino et al in Section 3.6. The statistics problem may be solved in the future with more data. More data currently exists, however, possible further complications with the transverse field of the magnet would possibly have to be accounted for and the analysis may not directly translate. Upgrades in the HERMES spectrometer made at the start of this year may also provide some events in the $x_F < 0$ region.

Fortunately, the results for the Λ in the inclusive study are more promising. Here, there are plenty of statistics for both the Λ and the K^0_S to make some statement of the Λ polarization in lepton-proton scattering, which has not been made before. Examining the

plot of P_Λ vs. ζ (Figure 5.12)(a), one might can see a change in the polarization around $\zeta = 0.25$ (unfortunately, perhaps blurred by the error bars). This is in agreement with the Monte Carlo plot in Figure 4.2, where a change from $x_F < 0$ to $x_F > 0$ takes place around $\zeta = 0.25$. Thus, the variable ζ has some relation to x_F, although, as pointed out in Section 4.2, the relationship is not perfect and the region $0 < \zeta < 0.25$ is most probably a mixture of target and current fragmentation regions and will be referred to as the "backward" region.

In the backward region, as seen in Figure 5.14(b), there is a noticeable polarization of around 10% (at least at higher p_T). At low p_T, there are more short tracks than long tracks and a smaller systematic error for short tracks over long tracks as well. It is interesting that a Λ can be produced polarized from an unpolarized target when the Λ is a result of the target remnant. The polarization here will hopefully stimulate further theoretical and experimental inquiry into the target fragmentation region.

In the "forward" region ($0.25 < \zeta < 1.0$), it is the short track statistics that suffer, although they are in agreement with the long tracks. The general picture here is in agreement with that of previous experiments in terms of the trend for an increasing polarization with p_T, however, the sign of the Λ polarization in our experiment is opposite that of the proton-proton collisions and our magnitude is not as large either. It should be noted that the results shown here are in agreement with the theoretical curve in Kubo's post-diction seen in Section 3.5 to older, previously released preliminary results of HERMES (of which the present results are similar). This would seem to indicate, however, that most of the Λ particles are directly produced in the lepton-proton collision and not as the result of a heavier hyperon decay.

The sign of the polarization can be understood in light of Kubo et al's quark recombination model or even more simply from thinking of the virtual photon as fluctuating into an $s - \bar{s}$ quark pair and applying the qualitative features of the DGM model to an incom-

ing s quark striking a $(ud)_0$ diquark in the proton target. In this picture, one would get the opposite polarization than that of $(ud)_0$ diquark from an incident proton beam incident on an s quark from the sea of the target. This should even be compared to the results of Gourlay et al. [34] wherein a K^- $(\bar{u}s)$ beam was incident on a proton target and a positive polarization resulted. This supports the spin of the Λ resulting from the s quark spin and relative angular momentum acquired by the s quark when taking part in the formation of the Λ.

The results for $\bar{\Lambda}$ in photoproduction may be a little confusing, however. If the Λ polarization is the result of a fluctuation into an $s - \bar{s}$ quark pair, then one might expect that the $\bar{\Lambda}$ would have the same polarization as that of the Λ. However, the results shown in Section 5.4(a) and (c) are consistent with *zero*. This could perhaps be accounted for by the way a $\bar{\Lambda}$ is produced compared to the Λ. Extending Kubo et al's use of the quark distribution of the photon, it is expected that the $\bar{s}$ content in the photon is the same as the s quark content (see M. Glück et al [35], from which the quark distributions were taken). Also, one has to take into into account the difference in the production mechanism for the $\bar{\Lambda}$ in that it must grab a $\bar{u}$ and a $\bar{d}$ quark from the sea of the target, as compared to the valence u and d quarks acquired for the Λ formation. Depending on how these quarks are drawn from the sea, one may end up with a different polarization since it is not just the $\bar{s}$ quark contributing to the polarization. but also the $\bar{u}$ and $\bar{d}$. Finally, the results in the backward region tend towards a negative $\bar{\Lambda}$ polarization, again due to some influence from target fragmentation.

In any case, there is a noticeable polarization of the Λ seen at HERMES in the case of inclusive production and a hint of polarization of Λ's in SIDIS that match trends seen by other experiments. These new measurements will hopefully, provide encouragement towards further study in the area of hyperon polarization, both theoretical and experimental, until a clear picture has emerged that explains this strange and unexpected phenomena. With more statistics from more recent (and ongoing) productions, HERMES will hopefully have

more to add in inclusive and semi-inclusive eP scattering.

Appendix A

Further Details of the Λ Analysis

A.1 Error Analysis

Recall from Chapter 3 the following expression for the formula for the polarization of the Λ using the weighted averaging technique.

$$\alpha P_n^{\Lambda} = \frac{< \cos\theta >_{TOP}^{TRUE} + \beta < \cos\theta >_{BOT}^{TRUE}}{< \cos^2\theta >_{TOP}^{TRUE} + \beta < \cos^2\theta >_{BOT}^{TRUE}} \tag{A.1}$$

where $\beta \equiv N_{BOT}/N_{TOP}$ and the cosine moments are the background subtracted cosine moments in the top and bottom. To calculate the error for eqn. (A.1), we note that it has the form

$$\alpha P_{\Lambda} = \frac{A + BC}{D + BE}$$

where

$$A =< \cos\theta >_{TOP}^{TRUE} \qquad B = N_{BOT}/N_{TOP} = \beta$$
$$C =< \cos\theta >_{BOT}^{TRUE} \qquad D =< \cos^2\theta >_{TOP}^{TRUE}$$
$$E =< \cos^2\theta >_{BOT}^{TRUE}$$

The error is given by

$$\delta(\alpha P_{\Lambda})^2 = \left(\frac{\partial P}{\partial A}\delta A\right)^2 + \left(\frac{\partial P}{\partial B}\delta B\right)^2 + \left(\frac{\partial P}{\partial C}\delta C\right)^2 + \left(\frac{\partial P}{\partial D}\delta D\right)^2 + \left(\frac{\partial P}{\partial E}\delta E\right)^2$$

For the error in B, the formula

$$\begin{aligned} \frac{\delta B}{B} &= \sqrt{\left(\frac{\Delta N_{BOT}}{N_{BOT}}\right)^2 + \left(\frac{\Delta N_{TOP}}{N_{TOP}}\right)^2} \\ &= \sqrt{\frac{1}{N_{BOT}} + \frac{1}{N_{TOP}}} \end{aligned}$$

is used. However, one must also determine the error for the TRUE cos moments. This is done in a similar fashion to above by setting

$$< \cos\theta >^{TRUE} = (1+f)X - fY \tag{A.2}$$

where f is defined as (N_{BG}/N_{TRUE}), $X \equiv < \cos\theta >^{MEAS}$, and $Y \equiv < \cos\theta >^{BG}$. Simply take partial derivatives as before to obtain the error. The error for the other formulas used for the determination of the Λ polarization are done in a similar fashion.

A.2 Burst List Mask Description

The burst list mask used for all year of data was 0x0208138C, which is a hexadecimal representation of the bits to check for data quality within the burst lists. Specifically, this mask checks that:

- the deadtime for trigger 21 is physical.
- the value of the burst length is reasonable.
- the uDST record is not marked as bad.
- there exists some PID information available (could fail if the calorimeter threshold was improperly set, for instance).
- the burst was marked as analyzeable in the logbook.
- there did exist *some* logbook data quality information and that the shift person responsible did not forget to enter this information by accident.

- the Transition Radiation Detector data quality was not marked as bad. If no TRD data quality information was available, then then the quality was assumed to be good.
- the RICH data quality was good (for years the RICH was in use; otherwise this bit is in reference to the Cherenkov detector).

A.3 Vertex Cut Determination

A particle that decays via a weak process, such as the Λ, will have a longer lifetime than other particles. By applying a vertex cut between the production and decay vertex, the background can be reduced. It can be reduced substantially with a strong vertex cut, but that would be at the expense of the true signal. As such, using the even averaging formula for the Λ polarization, the values of the polarization and their associated errors were studied for a variety of vertex cuts (10, 15, 20, and 25 cm).

The effect of the vertex cut can be seen in the mass peaks. For one bin of data ($0 < p_T < 3$ GeV and $0.164 < \zeta < 0.206$), we have the mass peaks in the top of the spectrometer as seen in Figure A.1. As one can see, for a 25 cm vertex cut, the background is reduced quite nicely as compared to the 10 cm cut, but the signal is also reduced quite significantly.

The results for the polarization of the Λ for the different vertex cuts are shown in Figures A.2, A.3, and A.4. These plots show that the points themselves do not change terribly with the changing vertex cuts, and that the errors also do not change appreciably. Although, a 10 cm vertex cut had the lowest error, the 15 cm vertex cut error was not too much larger and so, due to the extra background reduction, the 15 cm cut was chosen to be used when analyzing the data.

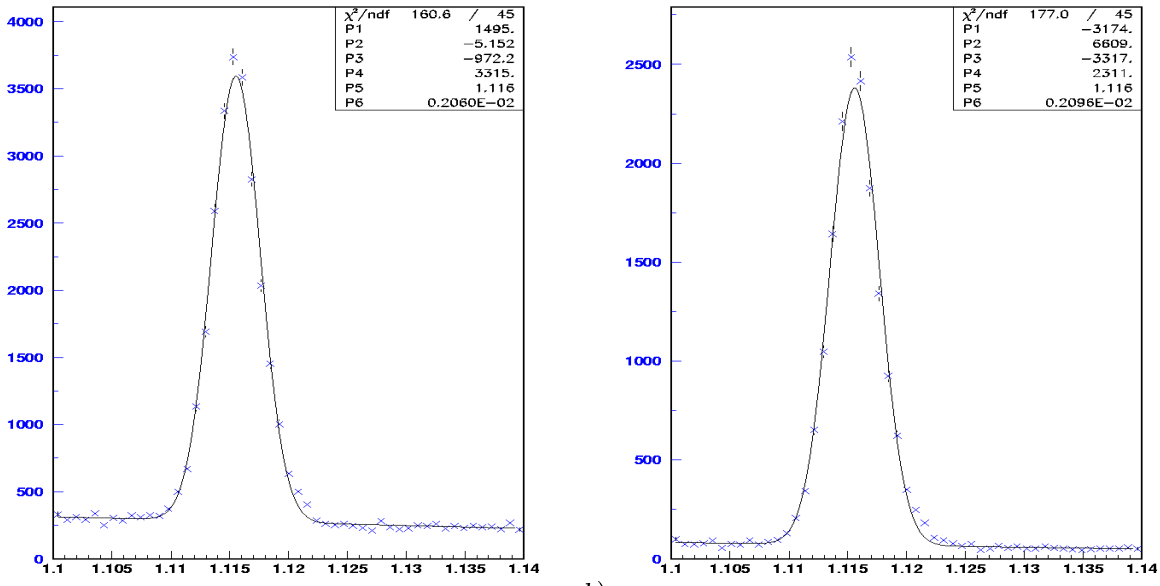

a) *b)*

Figure A.1: Mass peaks for a a) 10 cm and b) 25 cm vertex cut. The bin chosen for these peaks is in the text.

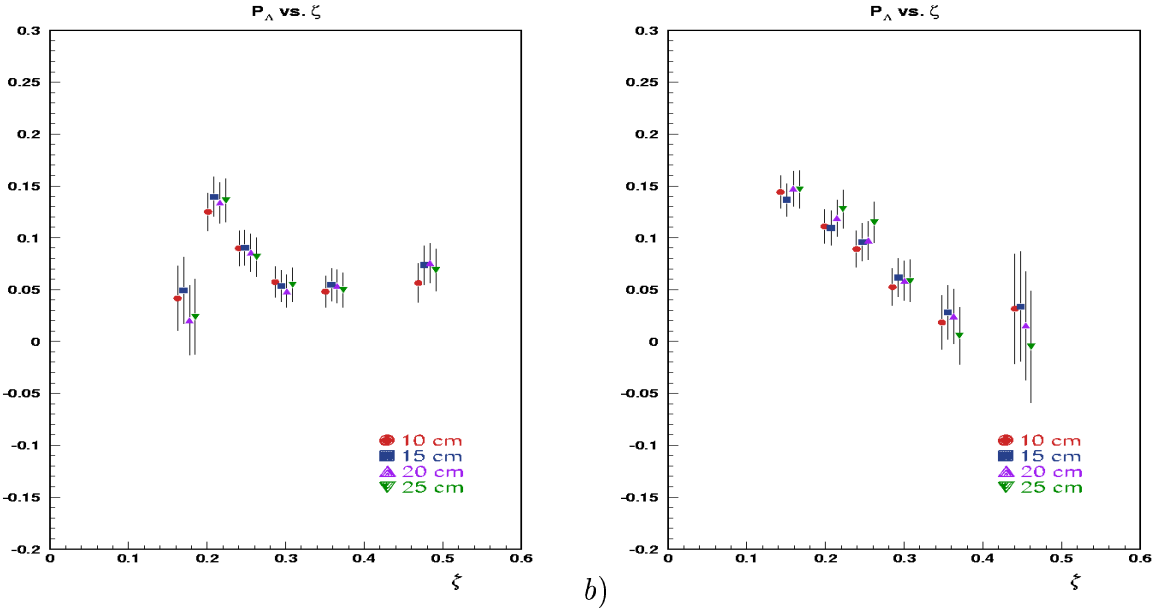

a) *b)*

Figure A.2: Λ Polarization vs. ζ for various vertex cut values. In a) we have long tracks only and in b) we have only short tracks.

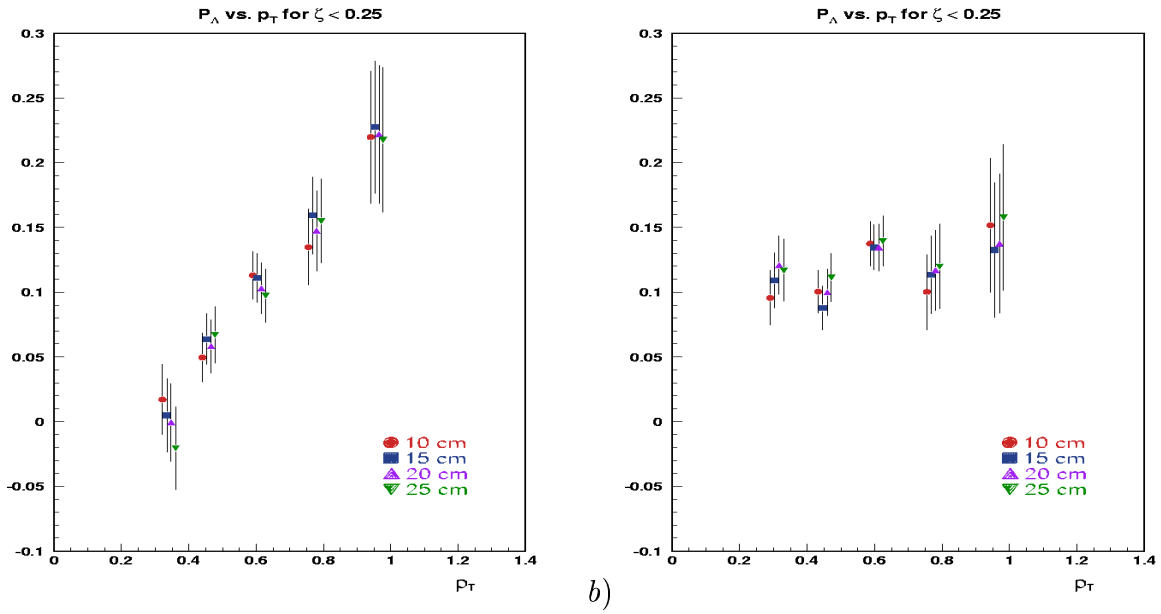

a) *b)*

Figure A.3: Λ Polarization vs. p_T ($\zeta < 0.25$)for various vertex cut values. In a) we have long tracks only and in b) we have only short tracks.

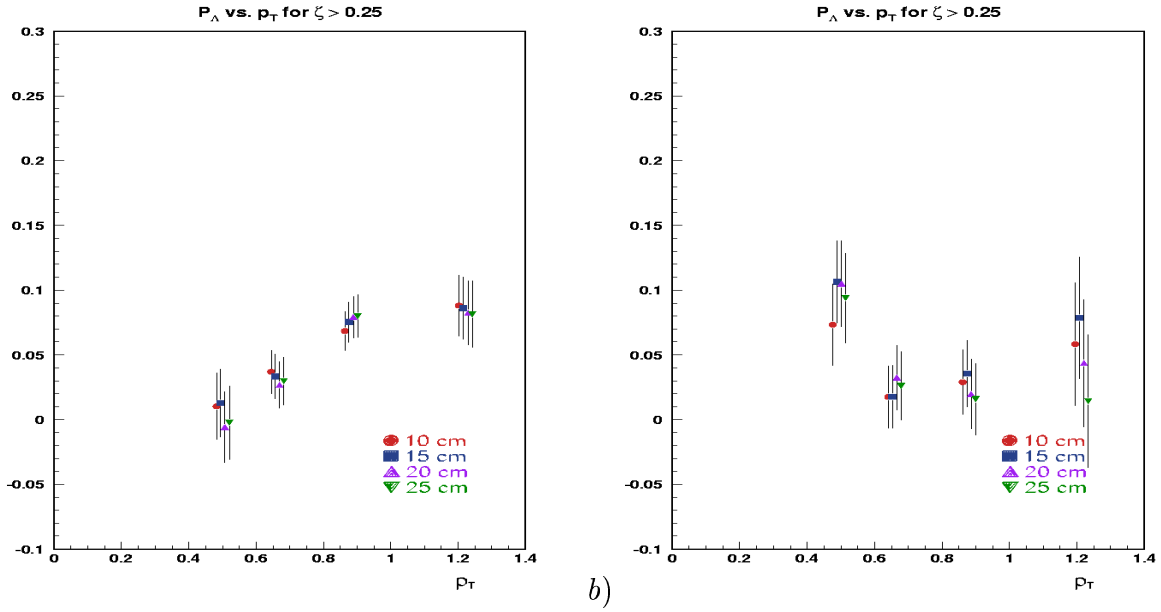

a) *b)*

Figure A.4: Λ Polarization vs. p_T ($\zeta > 0.25$) for various vertex cut values. In a) we have long tracks only and in b) we have only short tracks.

Appendix B

Maximum Likelihood Method

B.1 Introduction to Maximum Likelihood

The maximum likelihood method is a statistical technique used to determine an estimate on a parameter using observables obtained from experiment. This first section will be a short introduction to the method. For a basic introduction to the mathematics of the method, look to Tanis and Hogg [36] while good conceptual pictures can be found in Lyons [37]. If you let x_i be a measurement of the ith experiment and a be the parameter that one wishes to estimate, then the probability of each measurement will be defined as $f(x_i \mid a)$. Furthermore, suppose that there are N experiments so that we have measurements $x_1, x_2, \ldots, x_N$.

The next step is to construct the likelihood function, which will be denoted as $\mathcal{L}(a)$. This likelihood function is the joint probability of obtaining the measurements $x_i, i = 1, \ldots, N$, or rather

$$\begin{aligned} \mathcal{L}(a) &= f(x_1 \mid a) f(x_2 \mid a) \cdots f(x_N \mid a) \\ &= \prod_{i=1}^{N} f(x_i \mid a) \end{aligned} \tag{B.1}$$

Notice that the likelihood is a function of the parameter a and not the experimental observables. The best estimate of the parameter a is that value of a that maximizes the likelihood

function, *i.e.* that value of a that has the highest probability of producing the experimental observables. In many cases, it is easier to examine the log of the likelihood function, $L(a)$. Thus,

$$L(a) \;=\; \sum_{i=1}^{N} \log f(x_i \mid a) \tag{B.2}$$

Monte Carlo studies were done using the maximum likelihood method for the 3-dimensional polarization of the Λ, P^{Λ}. In this case, the x_i were the θ and ϕ of the decay proton in the Λ rest frame for each event i, the parameter a is the Λ polarization, and $f(x_i \mid P_\Lambda) \propto (1 + \alpha \vec{P}_\Lambda \cdot \hat{k_p})$, where $\hat{k_p}$ is the momentum direction of the proton (in the Λ rest frame).

B.2 Strengths and Weaknesses of Maximum Likelihood

The maximum likelihood method of parameter estimation has both its strengths and weaknesses [38]. One of its strengths is that it is extremely easy to apply parameter contraints when searching for an estimate, especially when using programs such as MINUIT (which will be discussed a bit more later on). Furthermore, once the estimate has been determined, the estimate for any function on that parameter is simply the value of the function evaluated at the estimate [37].

A key strength of the maximum likelihood method is that it is done event by event and not by bins. This has the advantage of being independent of considerations that need to be taken into account when binning, such as the total number of bins needed and the size of each bin [37]. It is also, usually, an efficient estimator [38]. This means that it will have the smallest average distance from its sample mean when an experiment is performed over several different samples. For a large number of events, the Maximum Likelihood Estimator is usually efficient.

However, even though the strengths of this estimation technique are impressive, optimism must be balanced by examining the weaknesses of the maximum likelihod method. One such

weakness is, depending on the likelihood function, the task to find the appropriate estimate can be quite computationally intensive. Also, it can be difficult to determine how good the fit to the data is, which requires a Monte Carlo simulation. Furthermore, for situations in which there is background in the signal, a more complicated likelihood function may be necessary [37]. This will increase the burdens of the two aforementioned problems as well. The Monte Carlo simulation for the Λ polarization will be covered in the next section for a 4π detector with some notes on applying the method to the HERMES acceptance.

B.3 Maximum Likelihood in Λ Polarization

The complete likelihood function for Λ Polarization, derived from the angular distribution of the decayed protons, is

$$\mathcal{L}(P_j^\Lambda) = \prod_{i=1}^{N} \frac{(1+\alpha(\vec{P^\Lambda}\cdot\vec{k_p}))\chi(\vec{x_i},\theta,\phi)}{\int(1+\alpha\vec{P^\Lambda}\cdot\vec{k_p})\chi(\vec{x_i},\theta,\phi)d\phi d\cos\theta} \tag{B.3}$$

where $j = x, y, z$, $\chi(\vec{x_i},\theta,\phi)$ is the acceptance function, and

$$\vec{P^\Lambda}\cdot\vec{k_p} = P_x^\Lambda \sin\theta\cos\phi + P_y^\Lambda \sin\theta\sin\phi + P_z^\Lambda\cos\theta. \tag{B.4}$$

The integral in the denominator is very important to include since it normalizes the probability for each event and it, too, contains a dependence on the parameter one is trying to estimate. With $L = \ln\mathcal{L}$, one gets

$$\begin{aligned} L(P_j^\Lambda) = & \sum_{i=1}^{N} ln(1+\alpha\vec{P^\Lambda}\cdot\vec{k_p}) + \ln(\chi(\vec{x_i},\theta,\phi)) \\ & - \ln\left(\int(1+\alpha\vec{P^\Lambda}\cdot\vec{k_p})\chi(\vec{x_i},\theta,\phi)d\phi d\cos\theta\right) \end{aligned} \tag{B.5}$$

The acceptance function complicates the above formula and, since it is an unknown function, it will be ignored at first, i. e. will be treated as a constant, and the case for 4-pi acceptance will be discussed. In the next section, it will be discussed how the acceptance function could be determined in the case of the HERMES spectrometer.

For this analysis, MINUIT was used. Since the idea of the maximum likelihood method is to maximize the likelihood function, one can use MINUIT to minimize the inverse of the likelihood function. Also, in the case of a constant valued acceptance function, the integral in eqn. (B.5) drops out and the second term in the expansion can be ignored since it is irrelevant for the maximization purposes (being independent of P_n, $n = x, y, z$). Thus, the function that is fed into MINUIT is

$$L(P_x^\Lambda, P_y^\Lambda, P_z^\Lambda) \;=\; -\sum_{i=1}^{N} \log(1 + \alpha(P_j^\Lambda \cos\theta_j)) \tag{B.6}$$

where $j = x, y, z$ and $\cos\theta_j$ is the angle between the proton momentum and the jth polarization axis.

To test the ability to extract the Λ polarization using this technique, a double blind analyis was performed. On the one hand, a polarized Monte Carlo was done with an unknown, set polarization. The polarization was then extracted using the above technique. The results are shown in table B.3.

As a small warning, the numbers chosen for the Λ polarization are not necessarily realistic in this study. One does not expect to measure three components of polarization from an unpolarized beam on an unpolarized target since that would be a violation of parity (which requires the polarization vector to be a pseudovector). The different number of events was chosen to test the ability to make the polarization determination when using relatively small data samples (such as that of trial 4 in an attempt to mimic the approximate number of events that are observed in the semi-inclusive lambda analysis). As expected, as the number of generated events decreased, the errors got larger, but the polarization obtained was always in good agreement with the input value.

The actual production chain used for this study was gmc_lpol, HSG (HERMES Smearing Generator), and then the udst-writer. The first item in the chain, gmc_lpol, was covered in Chapter 4. HSG simplifies the process of going through HMC (HERMES Monte Carlo) and HRC (HERMES Reconstruction Code) by using look up tables. Finally, the udst-writer

	Polarization Component	Actual Value	Predicted Value	Uncert.
trial 1	x-axis	1	0.9998	0.0073
	y-axis	0	0.0065	0.0081
	z-axis	0	0.0058	0.0081
trial 2	x-axis	0	-0.0063	0.0269
	y-axis	0	0.0046	0.0270
	z-axis	0	-0.0056	0.0271
trial 3	x-axis	0.45	0.4517	0.0255
	y-axis	0.2	0.1907	0.0260
	z-axis	0.7	0.7051	0.0249
trial 4	x-axis	0.45	0.4318	0.0427
	y-axis	0.2	0.2299	0.0431
	z-axis	0.7	0.7108	0.0417

Table B.1: Table of Maximum likelihood tests performed using a polarized Λ Monte Carlo generator. Trial 1 had 250,000 generated events (199,985 after a vertex separation cut); Trial 2 had 25,000 generated events (20,013 after a vertex separation cut); Trial 3 had 25,000 generated events (20,013 after a vertex separation cut); Trial 4 had 9,000 generated events (7194 after a vertex separation cut).

puts everything in a similar structure to that of the actual data tables HERMES uses. The advantage of using HSG here is a large increase in the speed of processing events. For instance, to get 3398 "good" Λ candidates using HMC thru HRC in a "fast" mode (using look up tables for certain detectors rather than simulating the detector response) it takes 16589 seconds while obtaining 2920 events with HSG it only take about 190 seconds.

B.4 Acceptance Correction

This analysis worked fine for the 4-pi analysis in Monte Carlo. However, it is desirable to determine the polarization for a full simulation of the HERMES spectrometer. This requires a method to determine the complicated acceptance function χ. In order to do this, a plan was devised to use the HERMES Smearing Generator (HSG) due to the speed advantage outlined above.

In all, the acceptance function would need to be defined by seven variables. Four of these variables $(\nu, Q^2, p_T^\Lambda, x_F)$ have distributions described reasonably well by Monte Carlo and three of the variables $(\phi_\Lambda^e, \theta_p, \phi_p)$ contain the new physics of interest first proposed in this research. In this case, ϕ_Λ^e is the angle of the Λ momentum with respect to the lepton beam. It was decided to attempt to bin in 5 bins for each of the four variables that the Monte Carlo describes well and 10 bins for the ϕ_Λ^e, θ_p, and ϕ_p variables, thus requiring 625,000 bins. The complete running speed of gmc_lpol to HSG to the histogramming package used to do the binning is 10-15 Million events/hr on the HERMES PC farm. Thus, to get 1000 events/bin (3% error per bin), it would take about 60 hours. To improve to 10000 events/bin (1% error per bin) would take 600 hours, or about 25 days.

This is an incredibly easy and fast solution to obtaining a lookup table for the acceptance function and would, thus, make the maximum likelihood method very attractive for studying the Λ polarization in all three dimensions. However, HSG was never meant to work as a general shortcut to doing HERMES Monte Carlo and fails especially for reconstructed

particles such as the Λ since it contains no vertex information for the decay products. It was found that the simulated data had a mass peak that was much narrower than the true mass peak width seen in the data and so this seemingly promising option had to be abandoned in favor of the moments style analysis used in this thesis.

Appendix C

Tables for Monte Carlo and Data

There is a lot of information that was not presented in the thesis proper, but is, nonetheless, important to record for posterity. The information taken from the Monte Carlo tables and from the K^0_S tables was used to determine the statistical error in the final data results. In the tables, the "T" represents results for the top of the spectrometer while "B" represents the results for the bottom of the spectrometer. In all the tables, the iteration method was used to calculate the Λ polarization. Please note that the errors are includes in parentheses and should be seen as the error on the last x digits, where x is the number of digits in the error. For example $0.2201(123) \equiv 0.2201 \pm 0.0123$. Some of the mass peaks (and, accordingly, σ values) have errors marked as (X). These errors are of the same size as the value, but, since the corresponding fit looked normal, should not affect the data in any way (a better fit would have approximately the same values, just a lower error, and the errors on the mass peaks and σ values are not part of the final error).

	$0 < \zeta < 1$	$0 < \zeta < 0.25$					$0.25 < \zeta < 1$			
$< p_T >$	T: 1.4287	T: 0.2973	0.4150	0.5712	0.7370	0.9709	T: 0.4580	0.6259	0.8639	1.7989
	B: 1.4282	B: 0.2976	0.4152	0.5713	0.7368	0.9710	B: 0.4574	0.6255	0.8635	1.8002
N_Λ	T: 1099570	T: 10537	33770	52167	34644	32290	T: 17025	55030	140724	724030
	B: 1100209	B: 10762	33683	52512	34577	32719	B: 16804	55008	140760	723288
N_{BG}	T: 226572	T: 1930	6236	10291	7131	7046	T: 3458	11207	29102	149782
	B: 227952	B: 2115	6633	10487	7351	7002	B: 3519	11287	29049	150404
mass	T: 1.1157(0)	T: 1.1159(3)	1.1157(2)	1.1157(1)	1.1157(2)	1.1157(2)	T: 1.1157(2)	1.1157(1)	1.1157(1)	1.1157(0)
	B: 1.1157(0)	B: 1.1158(3)	1.1157(2)	1.1157(1)	1.1157(2)	1.1157(2)	B: 1.1157(2)	1.1157(1)	1.1157(1)	1.1157(0)
σ	T: 0.002211(2)	T: 0.002291(30)	0.002225(13)	0.002232(10)	0.002209(11)	0.002188(12)	T: 0.002240(16)	0.002215(9)	0.002212(6)	0.002208(2)
	B: 0.002209(2)	B: 0.002244(37)	0.002220(17)	0.002217(10)	0.002190(11)	0.002213(12)	B: 0.002235(17)	0.002196(9)	0.002213(6)	0.002209(2)
$< \cos >_{\Lambda+BG}$	T: -0.0590(5)	T: -0.4493(34)	-0.3353(22)	-0.2455(19)	-0.1525(25)	0.0141(24)	T: -0.2103(41)	-0.1328(23)	-0.0860(14)	-0.0121(6)
	B: 0.0877(5)	B: 0.4718(33)	0.3450(22)	0.2618(19)	0.1759(25)	0.0066(24)	B: 0.2500(40)	0.1690(23)	0.1170(14)	0.0415(6)
$< \cos^2 >_{\Lambda+BG}$	T: 0.3315(3)	T: 0.3487(27)	0.3040(15)	0.2918(12)	0.2765(14)	0.2321(12)	T: 0.3832(22)	0.3640(12)	0.3599(7)	0.3335(3)
	B: 0.3331(3)	B: 0.3645(27)	0.3092(15)	0.2982(12)	0.2860(14)	0.2379(13)	B: 0.3885(22)	0.3690(12)	0.3605(7)	0.3337(3)
$< \cos >_{BG}$	T: -0.0344(6)	T: -0.4354(56)	-0.2934(32)	-0.2096(25)	-0.1352(30)	0.0045(29)	T: -0.1851(50)	-0.1015(28)	-0.0573(17)	0.0068(7)
	B: 0.0974(6)	B: 0.4609(53)	0.3391(31)	0.2516(25)	0.1850(30)	0.0496(29)	B: 0.2566(49)	0.1677(27)	0.1265(17)	0.0567(7)
$< \cos^2 >_{BG}$	T: 0.3302(3)	T: 0.3360(43)	0.2769(20)	0.2707(14)	0.2737(16)	0.2522(15)	T: 0.3768(26)	0.3611(14)	0.3546(9)	0.3328(4)
	B: 0.3344(3)	B: 0.3522(42)	0.2972(20)	0.2853(15)	0.2865(17)	0.2571(15)	B: 0.3952(26)	0.3699(14)	0.3589(9)	0.3347(4)
P_Λ	0.0515(21)	0.1186(317)	0.0129(153)	0.0381(112)	0.0549(132)	0.0458(145)	0.0779(165)	0.0684(90)	0.0512(56)	0.0522(25)

Table C.1: p_T distributions for long track MC for $P_\Lambda = 0.05$

$<\zeta>$	T: 0.1486	0.1882	0.2257	0.2726	0.3400	0.5622
	B: 0.1485	0.1883	0.2256	0.2726	0.3400	0.5627
N_Λ	T: 15462	56292	81072	119088	173339	654653
	B: 15396	56260	81727	119027	173400	654209
N_{BG}	T: 2958	11079	16480	24415	36292	135128
	B: 3170	11384	16920	24896	36275	135410
$mass$	T: 1.1158(2)	1.1157(1)	1.1157(1)	1.1157(1)	1.1157(1)	1.1157(0)
	B: 1.1158(2)	1.1157(1)	1.1157(1)	1.1157(1)	1.1157(1)	1.1157(0)
σ	T: 0.002244(25)	0.002235(10)	0.002211()7	0.002213(6)	0.002207(5)	0.002208(3)
	B: 0.002205(22)	0.002209(11)	0.002216(8)	0.002211(6)	0.002207(5)	0.002209(3)
$<\cos>_{\Lambda+BG}$	T: -0.2681(28)	-0.2333(18)	-0.1800(17)	-0.1237(15)	-0.0708(13)	-0.0096(7)
	B: 0.2819(28)	0.2477(18)	0.2012(16)	0.1516(15)	0.1009(13)	0.0401(7)
$<\cos^2>_{\Lambda+BG}$	T: 0.2151(18)	0.2722(11)	0.2991(9)	0.3228(8)	0.3418(7)	0.3424(3)
	B: 0.2206(18)	0.2796(11)	0.3064(9)	0.3284(8)	0.3434(7)	0.3420(3)
$<\cos>_{BG}$	T: -0.2379(43)	-0.1933(24)	-0.1423(21)	-0.0954(18)	-0.0441(15)	0.0100(8)
	B: 0.2687(42)	0.2360(23)	0.1973(20)	0.1548(17)	0.1070(15)	0.0559(8)
$<\cos^2>_{BG}$	T: 0.2053(25)	0.2582(13)	0.2948(11)	0.3221(9)	0.3380(8)	0.3410(4)
	B: 0.2207(25)	0.2741(14)	0.3065(11)	0.3302(9)	0.3425(8)	0.3429(4)
P_Λ	0.0597(269)	0.0317(112)	0.0420(84)	0.0544(65)	0.0540(51)	0.0530(26)

Table C.2: ζ distribution for long tracks $P_\Lambda = 0.05$

	$0 < \zeta < 1$	$0 < \zeta < 0.25$					$0.25 < \zeta < 1$			
$< p_{T'} >$	T: 0.9715	T: 0.2807	0.4108	0.5697	0.7377	0.9790	T: 0.4499	0.6206	0.8622	1.6095
	B: 0.9739	B: 0.2802	0.4107	0.5697	0.7380	0.9793	B: 0.4501	0.6206	0.8627	1.6112
N_Λ	T: 455238	T: 31208	46423	58581	40220	45849	T: 9673	21576	45780	155493
	B: 448083	B: 30543	45607	57801	39609	45365	B: 9366	20900	45129	153838
N_{BG}	T: 99547	T: 7233	10805	13370	8744	9731	T: 2103	4790	10054	32964
	B: 98148	B: 7052	10579	13280	8813	9711	B: 1973	4406	9696	32567
mass	T: 1.1156(0)	T: 1.1155(2)	1.1155(1)	1.1155(0)	1.1155(1)	1.1156(1)	T: 1.1155(3)	1.1156(2)	1.1156(1)	1.1156(1)
	B: 1.1156(0)	B: 1.1155(2)	1.1155(XX)	1.1155(XX)	1.1155(2)	1.1156(1)	B: 1.1156(3)	1.1156(2)	1.1156(XX)	1.1156(1)
σ	T: 0.002196(4)	T: 0.002177(18)	0.002178(18)	0.002178(8)	0.002184(16)	0.002209(11)	T: 0.002173(31)	0.002205(16)	0.002195(12)	0.002205(6)
	B: 0.002198(4)	B: 0.002198(18)	0.002167(XX)	0.002178(XX)	0.002191(15)	0.002212(12)	B: 0.002190(29)	0.002198(22)	0.002217(XX)	0.002204(7)
$< \cos >_{\Lambda+BG}$	T: 0.1199(7)	T: 0.0104(29)	0.1211(25)	0.1277(22)	0.0810(25)	-0.0231(20) $< \cos >_{\Lambda+BG}$	T: 0.3596(47)	0.3240(31)	0.2630(22)	0.1050(12)
	B: -0.0937(7)	B: 0.0152(29)	-0.0869(25)	-0.0975(22)	-0.0544(25)	0.0431(20)	B: -0.3328(49)	-0.2964(32)	-0.2401(22)	-0.0818(12)
$< \cos^2 >_{\Lambda+BG}$	T: 0.3091(4)	T: 0.3263(14)	0.3724(12)	0.3543(11)	0.3039(12)	0.2128(9)	T: 0.3932(29)	0.3518(19)	0.3285(13)	0.2822(7)
	B: 0.3046(4)	B: 0.3236(15)	0.3667(12)	0.3516(10)	0.3002(12)	0.2127(9)	B: 0.3785(29)	0.3395(19)	0.3197(13)	0.2787(7)
$< \cos >_{BG}$	T: 0.1384(9)	T: 0.0693(34)	0.1576(28)	0.1562(26)	0.1074(31)	0.0082(25)	T: 0.3522(61)	0.3159(37)	0.2525(26)	0.1224(14)
	B: -0.0814(9)	B: -0.0092(34)	-0.0942(30)	-0.0920(27)	-0.0613(31)	0.0396(24)	B: -0.3045(65)	-0.2608(40)	-0.2069(26)	-0.0670(15)
$< \cos^2 >_{BG}$	T: 0.3151(5)	T: 0.3276(18)	0.3666(15)	0.3590(13)	0.3098(15)	0.2206(12)	T: 0.3986(38)	0.3605(23)	0.3306(16)	0.2880(8)
	B: 0.3070(5)	B: 0.3227(18)	0.3633(15)	0.3492(13)	0.3027(15)	0.2190(12)	B: 0.3835(40)	0.3405(24)	0.3182(15)	0.2814(8)
P_Λ	0.0512(34)	0.0420(125)	0.0590(97)	0.0515(89)	0.0588(115)	0.0522(128)	0.0669(251)	0.0695(174)	0.0545(115)	0.0472(61)

Table C.3: p_T distributions for short track MC for $P_\Lambda = 0.05$

$<\zeta>$	T: 0.1330	0.1866	0.2247	0.2709	0.3365	0.4858
	B: 0.1329	0.1866	0.2247	0.2708	0.3364	0.4861
N_Λ	T: 64670	73708	75629	78750	74586	87532
	B: 63904	72695	73872	77643	73606	86112
N_{BG}	T: 14548	16729	16703	17625	15866	18312
	B: 14703	16505	16588	16996	15480	18009
$mass$	T: 1.1155(1)	1.1155(1)	1.1155(1)	1.1156(1)	1.1156(1)	1.1156(1)
	B: 1.1155(1)	1.1155(1)	1.1156(1)	1.1156(1)	1.1156(1)	1.1156(1)
σ	T: 0.002190(12)	0.002176(14)	0.002188(11)	0.002191(10)	0.002212(9)	0.002204(8)
	B: 0.002187(11)	0.002186(14)	0.002186(11)	0.002193(12)	0.002205(11)	0.002215(8)
$<\cos>_{\Lambda+BG}$	T: -0.0630(19)	0.0994(19)	0.1463(18)	0.1726(18)	0.1775(18)	0.1537(16)
	B: 0.0844(19)	-0.0712(19)	-0.1161(19)	-0.1448(18)	-0.1535(18)	-0.1306(16)
$<\cos^2>_{\Lambda+BG}$	T: 0.2790(9)	0.3326(9)	0.3303(10)	0.3245(10)	0.3103(10)	0.2784(9)
	B: 0.2806(9)	0.3298(9)	0.3239(10)	0.3176(10)	0.3027(10)	0.2742(9)
$<\cos>_{BG}$	T: -0.0123(22)	0.1415(23)	0.1633(22)	0.1830(21)	0.1957(22)	0.1578(18)
	B: 0.0652(22)	-0.0781(23)	-0.1068(23)	-0.1333(22)	-0.1349(22)	-0.1052(19)
$<\cos^2>_{BG}$	T: 0.2797(10)	0.3394(12)	0.3377(12)	0.3309(12)	0.3217(13)	0.2814(10)
	B: 0.2809(10)	0.3340(12)	0.3263(12)	0.3201(12)	0.3075(13)	0.2761(10)
P_Λ	0.0411(95)	0.0487(81)	0.0615(82)	0.0608(82)	0.0457(87)	0.0515(83)

Table C.4: ζ distribution for short tracks $P_\Lambda = 0.05$

	$0 < \zeta < 1$	$0 < \zeta < 0.25$					$0.25 < \zeta < 1$			
$< p_T >$	T: 1.4300	T: 0.2973	0.4150	0.5712	0.7370	0.9711	T: 0.4580	0.6259	0.8640	1.7992
	B: 1.4271	B: 0.2975	0.4151	0.5712	0.7368	0.9708	B: 0.4574	0.6255	0.8635	1.8001
N_Λ	T: 1097485	T: 10406	33476	51674	34434	32323	T: 16904	54779	140282	723613
	B: 1102850	B: 10916	34045	52944	34745	32741	B: 16954	55307	141223	723668
N_{BG}	T: 226526	T: 1936	6232	10289	7141	7039	T: 3460	11213	29121	149783
	B: 227931	B: 2115	6635	10483	7341	6995	B: 3521	11264	29045	150488
mass	T: 1.1157(0)	T: 1.1159(3)	1.1157(2)	1.1157(1)	1.1157(2)	1.1157(2)	T: 1.1157(2)	1.1157(1)	1.1157(1)	1.1157(0)
	B: 1.1157(0)	B: 1.1158(3)	1.1157(2)	1.1157(1)	1.1157(2)	1.1157(2)	B: 1.1157(2)	1.1157(1)	1.1157(1)	1.1157(0)
σ	T: 0.002211(2)	T: 0.002300(31)	0.002222(13)	0.002231(10)	0.002210(11)	0.002187(12)	T: 0.002242(17)	0.002215(9)	0.002213(6)	0.002208(2)
	B: 0.002209(2)	B: 0.002242(36)	0.002223(17)	0.002217(10)	0.002191(11)	0.002213(12)	B: 0.002235(18)	0.002197(9)	0.002214(6)	0.002208(2)
$< \cos >_{\Lambda+BG}$	T: -0.0502(5)	T: -0.4450(35)	-0.3297(22)	-0.2390(19)	-0.1454(25)	0.0201(24)	T: -0.2012(41)	-0.1232(23)	-0.0768(14)	-0.0032(6)
	B: 0.0964(5)	B: 0.4754(33)	0.3499(22)	0.2681(19)	0.1827(25)	0.0126(24)	B: 0.2586(40)	0.1781(23)	0.1261(14)	0.0503(6)
$< \cos^2 >_{\Lambda+BG}$	T: 0.3309(3)	T: 0.3464(27)	0.3014(15)	0.2893(12)	0.2747(14)	0.2316(12)	T: 0.3812(22)	0.3630(12)	0.3592(7)	0.3332(3)
	B: 0.3337(3)	B: 0.3674(27)	0.3115(15)	0.3003(12)	0.2880(14)	0.2383(13)	B: 0.3906(22)	0.3703(12)	0.3613(7)	0.3339(3)
$< \cos >_{BG}$	T: -0.0344(6)	T: -0.4351(56)	-0.2933(32)	-0.2095(25)	-0.1353(30)	0.0044(29)	T: -0.1853(50)	-0.1015(28)	-0.0571(17)	0.0068(7)
	B: 0.0975(6)	B: 0.4607(54)	0.3390(31)	0.2517(25)	0.1849(30)	0.0496(29)	B: 0.2567(49)	0.1678(27)	0.1265(17)	0.0568(7)
$< \cos^2 >_{BG}$	T: 0.3302(3)	T: 0.3360(43)	0.2769(20)	0.2707(14)	0.2737(16)	0.2522(15)	T: 0.3768(26)	0.3611(14)	0.3546(9)	0.3328(4)
	B: 0.3344(3)	B: 0.3521(42)	0.2971(20)	0.2854(15)	0.2864(17)	0.2571(15)	B: 0.3953(26)	0.3699(14)	0.3589(9)	0.3347(4)
P_Λ	0.1016(21)	0.1683(316)	0.0631(153)	0.0890(112)	0.1065(132)	0.0950(145) P_Λ	0.1281(165)	0.1192(90)	0.1003(56)	0.1024(25)

Table C.5: p_T distributions for long track MC for $P_\Lambda = 0.10$

$<\zeta>$	T: 0.1486	0.1882	0.2257	0.2727	0.3400	0.5623
	B: 0.1485	0.1883	0.2256	0.2726	0.3400	0.5626
N_Λ	T: 15360	55853	80553	118540	173006	654382
	B: 15517	56710	82279	119557	173941	654800
N_{BG}	T: 2958	11081	16476	24444	36305	135082
	B: 3178	11364	16852	24881	36253	135250
$mass$	T: 1.1158(2)	1.1157(1)	1.1157(1)	1.1157(1)	1.1157(1)	1.1157(0)
	B: 1.1158(2)	1.1157(1)	1.1157(1)	1.1157(1)	1.1157(1)	1.1157(0)
σ	T: 0.002243(25)	0.002234(10)	0.002211(7)	0.002214(6)	0.002207(5)	0.002209(3)
	B: 0.002208(22)	0.002208(11)	0.002218(8)	0.002211(6)	0.002207(5)	0.002208(3)
$<\cos>_{\Lambda+BG}$	T: -0.2636(28)	-0.2274(18)	-0.1726(17)	-0.1156(15)	-0.0617(13)	-0.0004(7)
	B: 0.2855(27)	0.2535(18)	0.2081(16)	0.1597(15)	0.1098(13)	0.0491(7)
$<\cos^2>_{\Lambda+BG}$	T: 0.2134(18)	0.2701(11)	0.2970(9)	0.3214(8)	0.3410(7)	0.3422(3)
	B: 0.2224(18)	0.2819(11)	0.3083(9)	0.3297(8)	0.3443(7)	0.3421(3)
$<\cos>_{BG}$	T: -0.2379(43)	-0.1933(24)	-0.1422(21)	-0.0954(18)	-0.0440(15)	0.0101(8)
	B: 0.2686(42)	0.2360(23)	0.1974(20)	0.1549(17)	0.1071(15)	0.0559(8)
$<\cos^2>_{BG}$	T: 0.2053(25)	0.2582(13)	0.2948(11)	0.3221(9)	0.3380(8)	0.3410(4)
	B: 0.2206(25)	0.2741(14)	0.3065(11)	0.3302(9)	0.3425(8)	0.3429(4)
P_Λ	0.1125(268)	0.0818(112)	0.0925(84)	0.1045(65)	0.1043(51)	0.1029(26)

Table C.6: ζ distribution for long tracks $P_\Lambda = 0.10$

	$0 < \zeta < 1$	$0 < \zeta < 0.25$					$0.25 < \zeta < 1$			
$< p_T >$	T: 0.9713	T: 0.2808	0.4109	0.5697	0.7376	0.9789	T: 0.4500	0.6205	0.8621	1.6094
	B: 0.9741	B: 0.2802	0.4107	0.5698	0.7381	0.9794	B: 0.4500	0.6207	0.8627	1.6115
N_Λ	T: 456889	T: 31181	46530	58550	40428	45855	T: 9801	21836	46174	155994
	B: 446336	B: 30476	45404	57568	39479	45358	B: 9265	20568	44651	153256
N_{BG}	T: 99587	T: 7252	10776	13481	8722	9719	T: 2099	4797	10014	32926
	B: 98282	B: 7110	10577	13310	8891	9770	B: 1980	4456	9751	32532
mass	T: 1.1156(0)	T: 1.1155(2)	1.1155(1)	1.1155(1)	1.1155(1)	1.1156(1)	T: 1.1155(3)	1.1156(2)	1.1156(1)	1.1156(1)
	B: 1.1156(0)	B: 1.1155(2)	1.1155(1)	1.1155(1)	1.1155(2)	1.1156(1)	B: 1.1156(3)	1.1156(2)	1.1156(1)	1.1156(1)
σ	T: 0.002196(4)	T: 0.002179(17)	0.002177(18)	0.002176(16)	0.002186(16)	0.002211(11)	T: 0.002173(30)	0.002211(16)	0.002198(12)	0.002206(6)
	B: 0.002198(4)	B: 0.002194(19)	0.002167(17)	0.002178(15)	0.002188(15)	0.002212(12)	B: 0.002186(29)	0.002195(22)	0.002214(13)	0.002204(7)
$< \cos >_{\Lambda+BG}$	T: 0.1276(7)	T: 0.0187(29)	0.1308(25)	0.1368(22)	0.0888(25)	-0.0179(20)	T: 0.3668(47)	0.3301(30)	0.2701(21)	0.1122(12)
	B: -0.0858(7)	B: 0.0239(29)	-0.0770(25)	-0.0885(22)	-0.0464(25)	0.0491(20)	B: -0.3230(49)	-0.2902(32)	-0.2330(22)	-0.0747(12)
$< \cos^2 >_{\Lambda+BG}$	T: 0.3103(4)	T: 0.3263(14)	0.3732(12)	0.3558(11)	0.3051(12)	0.2126(9)	T: 0.3965(29)	0.3541(19)	0.3307(13)	0.2832(7)
	B: 0.3035(4)	B: 0.3238(15)	0.3659(12)	0.3503(10)	0.2990(12)	0.2126(9)	B: 0.3748(29)	0.3372(19)	0.3175(13)	0.2779(7)
$< \cos >_{BG}$	T: 0.1384(9)	T: 0.0695(34)	0.1576(28)	0.1562(26)	0.1076(31)	0.0083(25)	T: 0.3528(61)	0.3153(37)	0.2525(26)	0.1224(14)
	B: -0.0813(9)	B: -0.0089(34)	-0.0941(30)	-0.0919(27)	-0.0612(31)	0.0396(24)	B: -0.3038(66)	-0.2610(40)	-0.2070(26)	-0.0670(15)
$< \cos^2 >_{BG}$	T: 0.3151(5)	T: 0.3276(18)	0.3666(15)	0.3590(13)	0.3099(15)	0.2206(12)	T: 0.3989(38)	0.3604(23)	0.3307(16)	0.2879(8)
	B: 0.3070(5)	B: 0.3226(18)	0.3633(15)	0.3492(13)	0.3027(15)	0.2190(12)	B: 0.3830(40)	0.3406(24)	0.3181(16)	0.2815(8)
P_Λ	0.1018(34)	0.0923(125)	0.1114(97)	0.1020(89)	0.1090(115)	0.1029(128)	0.1262(250)	0.1167(174)	0.1061(115)	0.0968(61)

Table C.7: p_T distributions for short track MC for $P_\Lambda = 0.10$

$<\zeta>$	T: 0.1331	0.1866	0.2247	0.2709	0.3365	0.4858
	B: 0.1328	0.1866	0.2247	0.2708	0.3364	0.4862
N_Λ	T: 64422	73993	76006	79210	74972	88012
	B: 64120	72539	73575	77025	73237	85734
N_{BG}	T: 14576	16668	16730	17562	15894	18298
	B: 14672	16469	16592	17070	15487	17994
$mass$	T: 1.1155(1)	1.1155(1)	1.1155(1)	1.1156(1)	1.1156(1)	1.1156(1)
	B: 1.1155(1)	1.1155(1)	1.1155(1)	1.1156(1)	1.1156(1)	1.1156(1)
σ	T: 0.002188(12)	0.002179(13)	0.002189(11)	0.002193(10)	0.002213(9)	0.002202(8)
	B: 0.002189(11)	0.002187(14)	0.002188(11)	0.002190(12)	0.002203(11)	0.002218(8)
$<\cos>_{\Lambda+BG}$	T: -0.0554(19)	0.1076(19)	0.1541(18)	0.1805(17)	0.1846(18)	0.1606(15)
	B: 0.0920(19)	-0.0626(19)	-0.1077(19)	-0.1367(18)	-0.1462(18)	-0.1238(16)
$<\cos^2>_{\Lambda+BG}$	T: 0.2783(9)	0.3336(9)	0.3319(10)	0.3265(10)	0.3120(10)	0.2796(9)
	B: 0.2812(9)	0.3286(9)	0.3226(10)	0.3161(10)	0.3011(10)	0.2732(9)
$<\cos>_{BG}$	T: -0.0124(22)	0.1417(23)	0.1634(22)	0.1831(21)	0.1957(22)	0.1579(18)
	B: 0.0651(22)	-0.0779(23)	-0.1068(23)	-0.1331(22)	-0.1349(22)	-0.1052(19)
$<\cos^2>_{BG}$	T: 0.2797(10)	0.3395(12)	0.3377(12)	0.3310(12)	0.3217(13)	0.2814(10)
	B: 0.2809(10)	0.3339(12)	0.3262(12)	0.3199(12)	0.3075(13)	0.2761(10)
P_Λ	0.0945(95)	0.0985(81)	0.1112(82)	0.1119(82)	0.0944(87)	0.1022(83)

Table C.8: ζ distribution for short tracks $P_\Lambda = 0.10$

	$0 < \zeta < 1$	$0 < \zeta < 0.25$					$0.25 < \zeta < 1$			
$< p_T >$	T: 1.2318	T: 0.2951	0.4119	0.5615	0.7320	0.9644	T: 0.4534	0.6195	0.8593	1.7988
	B: 1.2205	B: 0.2947	0.4120	0.5610	0.7320	0.9646	B: 0.4524	0.6197	0.8589	1.7993
N_Λ	T: 702513	T: 25503	66893	65826	25745	17628	T: 18046	40935	76694	365238
	B: 715409	B: 28549	70741	68484	26095	17558	B: 18562	41481	77712	366065
N_{BG}	T: 144766	T: 5445	12893	13228	5242	3820	T: 3725	8473	15938	75872
	B: 146346	B: 5945	13586	13454	5444	3849	B: 3854	8441	15870	75846
mass	T: 1.1157(0)	T: 1.1159(1)	1.1158(1)	1.1157(1)	1.1157(2)	1.1157(2)	T: 1.1157(2)	1.1157(1)	1.1157(1)	1.1157(0)
	B: 1.1157(0)	B: 1.1159(1)	1.1158(1)	1.1157(1)	1.1157(2)	1.1156(2)	B: 1.1157(2)	1.1157(1)	1.1157(1)	1.1157(0)
σ	T: 0.002212(2)	T: 0.002201(28)	0.002217(11)	0.002229(9)	0.002215(13)	0.002169(16)	T: 0.002206(15)	0.002228(11)	0.002203(8)	0.002209(3)
	B: 0.002212(3)	B: 0.002214(21)	0.002235(13)	0.002217(9)	0.002198(13)	0.002201(16)	B: 0.002250(16)	0.002191(1)	0.002208(7)	0.002208(3)
$< \cos >_{\Lambda+BG}$	T: -0.0810(6)	T: -0.4489(20)	-0.3228(15)	-0.2229(17)	-0.1243(28)	0.0285(33)	T: -0.1869(39)	-0.1072(26)	-0.0594(20)	0.0152(9)
	B: 0.1577(6)	B: 0.4787(18)	0.3616(14)	0.2770(16)	0.1842(28)	0.0299(33)	B: 0.2805(38)	0.1971(26)	0.1449(19)	0.0682(9)
$< \cos^2 >_{\Lambda+BG}$	T: 0.3211(3)	T: 0.3243(16)	0.2772(10)	0.2657(10)	0.2645(16)	0.2319(17)	T: 0.3734(21)	0.3568(14)	0.3575(10)	0.3330(4)
	B: 0.3292(3)	B: 0.3454(16)	0.2973(10)	0.2871(10)	0.2802(16)	0.2401(17)	B: 0.3947(21)	0.3699(14)	0.3640(10)	0.3346(4)
$< \cos >_{BG}$	T: -0.0784(7)	T: -0.4440(35)	-0.3058(22)	-0.2148(22)	-0.1295(34)	0.0031(39)	T: -0.1888(48)	-0.1091(32)	-0.0606(23)	0.0079(10)
	B: 0.1375(7)	B: 0.4657(34)	0.3398(22)	0.2493(22)	0.1792(34)	0.0514(39)	B: 0.2535(46)	0.1745(32)	0.1284(23)	0.0560(10)
$< \cos^2 >_{BG}$	T: 0.3225(4)	T: 0.3190(29)	0.2616(14)	0.2571(13)	0.2647(19)	0.2544(20)	T: 0.3735(25)	0.3588(16)	0.3546(12)	0.3327(5)
	B: 0.3283(4)	B: 0.3331(28)	0.2787(14)	0.2702(13)	0.2797(19)	0.2543(20)	B: 0.3885(25)	0.3652(17)	0.3572(12)	0.3348(5)
P_Λ	0.2015(26)	0.2046(225)	0.1810(114)	0.2101(103)	0.1944(154)	0.1984(196)	0.2360(160)	0.2175(104)	0.1977(75)	0.2043(35)

Table C.9: p_T distributions for long track MC for $P_\Lambda = 0.20$

$<\zeta>$	T: 0.1432	0.1857	0.2249	0.2717	0.3393	0.5613
	B: 0.1433	0.1857	0.2248	0.2715	0.3391	0.5613
N_Λ	T: 50731	73861	69114	79093	96780	332955
	B: 53778	77603	71752	81155	97297	333750
N_{BG}	T: 10549	14564	13941	16490	20253	68886
	B: 11248	14994	14410	16630	20246	68755
$mass$	T: 1.1159	1.1157(1)	1.1157(1)	1.1157(1)	1.1156(1)	1.1157(1)
	B: 1.1159(1)	1.1157(1)	1.1157(1)	1.1157(1)	1.1157(1)	1.1157(1)
σ	T: 0.002192	0.002219(9)	0.002226(8)	0.002211(7)	0.002205(7)	0.002211(4)
	B: 0.002203(15)	0.002219(10)	0.002230(8)	0.002209(7)	0.002215(7)	0.002207(4)
$<\cos>_{\Lambda+BG}$	T: -0.3008(14)	-0.2717(15)	-0.1988(18)	-0.1167(18)	-0.0471(17)	0.0174(9)
	B: 0.3305(14)	0.3218(15)	0.2612(17)	0.1973(18)	0.1321(17)	0.0679(9)
$<\cos^2>_{\Lambda+BG}$	T: 0.2178(10)	0.2803(9)	0.3032(10)	0.3238(10)	0.3439(9)	0.3424(5)
	B: 0.2341(10)	0.3028(10)	0.3233(10)	0.3401(10)	0.3499(9)	0.3434(5)
$<\cos>_{BG}$	T: -0.2854(24)	-0.2448(21)	-0.1791(23)	-0.1134(22)	-0.0495(20)	0.0100(11)
	B: 0.3122(24)	0.2808(21)	0.2300(22)	0.1708(21)	0.1132(20)	0.0560(11)
$<\cos^2>_{BG}$	T: 0.2105(15)	0.2666(12)	0.3014(12)	0.3264(11)	0.3412(10)	0.3416(6)
	B: 0.2245(15)	0.2830(13)	0.3129(12)	0.3347(12)	0.3460(10)	0.3431(6)
P_Λ	0.1877(157)	0.2023(100)	0.1944(92)	0.2165(79)	0.2052(68)	0.2030(37)

Table C.10: ζ distribution for long tracks $P_\Lambda = 0.20$

	$0 < \zeta < 1$	$0 < \zeta < 0.25$					$0.25 < \zeta < 1$			
$< p_T >$	T: 0.5720	T: 0.2723	0.4025	0.5556	0.7313	0.9720	T: 0.4458	0.6147	0.8562	1.6068
	B: 0.5668	B: 0.2718	0.4021	0.5555	0.7320	0.9721	B: 0.4450	0.6149	0.8580	1.6114
N_Λ	T: 700810	T: 237855	177833	97078	31950	24863	T: 11452	16941	26146	79057
	B: 702849	B: 241044	176842	93909	30853	24895	B: 10040	15202	24188	77088
N_{BG}	T: 155715	T: 51554	39574	22023	7018	5354	T: 2369	3713	5525	16769
	B: 149335	B: 54074	39439	21743	6802	5210	B: 2155	3382	5324	16346
mass	T: 1.1156(0)	T: 1.1155(1)	1.1155(1)	1.1155(1)	1.1155(2)	1.1156(2)	T: 1.1155(3)	1.1156(2)	1.1156(2)	1.1156(1)
	B: 1.1156(0)	B: 1.1155(1)	1.1155(1)	1.1155(1)	1.1155(2)	1.1156(XX)	B: 1.1156(3)	1.1156(2)	1.1156(2)	1.1156(1)
σ	T: 0.002192(3)	T: 0.002206(6)	0.002187(7)	0.002183(10)	0.002190(20)	0.002215(14)	T: 0.002205(34)	0.002216(17)	0.002210(14)	0.002202(9)
	B: 0.002207(3)	B: 0.002186(6)	0.002189(8)	0.002175(10)	0.002171(18)	0.002208(XX)	B: 0.002167(21)	0.002195(27)	0.002198(17)	0.002202(10)
$< \cos >_{\Lambda+BG}$	T: 0.0237(6)	T: -0.0949(9)	0.0069(12)	0.0785(17)	0.0881(27)	-0.0051(26)	T: 0.3769(44)	0.3498(34)	0.2844(28)	0.1272(17)
	B: 0.0496(6)	B: 0.1542(9)	0.0723(12)	0.0063(17)	-0.0148(28)	0.0575(26)	B: -0.3048(48)	-0.2797(37)	-0.2222(30)	-0.0579(17)
$< \cos^2 >_{\Lambda+BG}$	T: 0.2924(3)	T: 0.2563(5)	0.3119(6)	0.3320(8)	0.2986(13)	0.2113(12)	T: 0.4049(27)	0.3661(21)	0.3364(17)	0.2850(9)
	B: 0.2881(3)	B: 0.2615(5)	0.3097(6)	0.3209(8)	0.2890(13)	0.2137(12)	B: 0.3757(28)	0.3395(22)	0.3160(17)	0.2757(9)
$< \cos >_{BG}$	T: 0.0322(7)	T: -0.0749(11)	0.0298(14)	0.0861(20)	0.0908(34)	0.0104(33)	T: 0.3597(58)	0.3193(42)	0.2513(34)	0.1201(20)
	B: 0.0237(7)	B: 0.1261(11)	0.0282(14)	-0.0227(20)	-0.0399(34)	0.0370(33)	B: -0.2894(64)	-0.2687(46)	-0.2113(36)	-0.0668(21)
$< \cos^2 >_{BG}$	T: 0.2961(4)	T: 0.2659(5)	0.3119(7)	0.3261(10)	0.2996(17)	0.2221(16)	T: 0.4099(36)	0.3649(26)	0.3322(21)	0.2877(11)
	B: 0.2932(3)	B: 0.2690(5)	0.3099(7)	0.3202(10)	0.2909(17)	0.2201(16)	B: 0.3814(38)	0.3505(28)	0.3208(21)	0.2813(11)
P_Λ	0.2075(28)	0.1990(52)	0.2115(53)	0.2144(71)	0.2093(130)	0.1987(173)	0.2082(232)	0.2321(198)	0.2004(154)	0.2091(85)

Table C.11: p_T distributions for short track MC for $P_\Lambda = 0.20$

$<\zeta>$	T: 0.1181	0.1837	0.2240	0.2701	0.3356	0.4847
	B: 0.1173	0.1836	0.2239	0.2701	0.3355	0.4857
N_Λ	T: 405386	95844	60809	51980	42162	45232
	B: 413332	91276	56824	48718	40202	43273
N_{BG}	T: 90460	21897	13616	11469	8924	9432
	B: 92276	21377	12867	10730	8469	9228
$mass$	T: 1.1156	1.1155(1)	1.1155(1)	1.1155(1)	1.1156(1)	1.1156(1)
	B: 1.1156(0)	1.1155(1)	1.1156(1)	1.1156(1)	1.1156(1)	1.1157(1)
σ	T: 0.002191	0.002168	0.002200	0.002199	0.002199	0.002213
	B: 0.002185(5)	0.002185(14)	0.002177(14)	0.002171(13)	0.002207(14)	0.002213(11)
$<\cos>_{\Lambda+BG}$	T: -0.1027(7)	0.1646(17)	0.2215(21)	0.2345(22)	0.2125(23)	0.1763(21)
	B: 0.1628(7)	-0.0781(18)	-0.1348(22)	-0.1552(23)	-0.1434(24)	-0.1092(22)
$<\cos^2>_{\Lambda+BG}$	T: 0.2537(3)	0.3694(8)	0.3714(11)	0.3500(12)	0.3166(13)	0.2813(12)
	B: 0.2601(3)	0.3587(8)	0.3495(11)	0.3296(12)	0.2986(13)	0.2702(12)
$<\cos>_{BG}$	T: -0.0792(8)	0.1796(20)	0.2089(25)	0.2157(27)	0.2052(29)	0.1573(26)
	B: 0.1290(8)	-0.1200(21)	-0.1477(27)	-0.1640 (28)	-0.1451(30)	-0.1063(26)
$<\cos^2>_{BG}$	T: 0.2603(4)	0.3690(10)	0.3713(14)	0.3500(16)	0.3229(17)	0.2808(14)
	B: 0.2638(4)	0.3638(11)	0.3587(14)	0.3366(16)	0.3089(17)	0.2754(14)
P_Λ	T: 0.2054(40)	0.2065(69)	0.2195(90)	0.2213(102)	0.2019(117)	0.2158(117)

Table C.12: ζ distribution for short tracks $P_\Lambda = 0.20$

	$0 < \zeta < 1$	$0 < \zeta < 0.25$					$0.25 < \zeta < 1$			
$< p_T >$	T: 0.6825	T: 0.2996	0.4161	0.5656	0.7306	0.9173	T: 0.4589	0.6194	0.8391	1.1792
	B: 0.6815	B: 0.2985	0.4162	0.5655	0.7300	0.9127	B: 0.4596	0.6202	0.8386	1.1751
N_Λ	T: 63873	T: 2072	8014	10853	4959	1871	T: 4079	11206	14464	6189
	B: 67895	B: 2297	8618	11654	5101	1895	B: 4270	11950	15700	6732
N_{BG}	T: 7288	T: 284	997	1497	600	237	T: 349	988	1658	712
	B: 6689	B: 249	987	1290	524	178	B: 325	953	1288	587
$mass$	T: 1.1156(1)	T: 1.1155(0)	1.1155(3)	1.1155(2)	1.1156(3)	1.1159(2)	T: 1.1156(4)	1.1156(0)	1.1157(1)	1.1157(1)
	B: 1.1157(1)	B: 1.1157(5)	1.1157(0)	1.1157(2)	1.1158(4)	1.1159(6)	B: 1.1158(4)	1.1158(2)	1.1158(2)	1.1158(4)
σ	T: 0.002314(25)	T: 0.001908(40)	0.002064(48)	0.002156(54)	0.002384(45)	0.002532(63)	T: 0.002319(63)	0.002376(22)	0.002426(25)	0.002529(35)
	B: 0.002192(18)	B: 0.001808(34)	0.001924(17)	0.002029(27)	0.002215(58)	0.002258(89)	B: 0.002201(36)	0.002281(42)	0.002366(51)	0.002534(73)
$< \cos >_{\Lambda+BG}$	T: -0.1443(21)	T: -0.4255(75)	-0.2917(46)	-0.1884(44)	-0.0987(69)	0.0403(107)	T: -0.2079(88)	-0.1226(54)	-0.0759(47)	-0.0161(72)
	B: 0.1758(20)	B: 0.4283(75)	0.3147(45)	0.2303(42)	0.1511(68)	0.0293(113)	B: 0.2112(87)	0.1379(53)	0.1080(46)	0.0565(71)
$< \cos^2 >_{\Lambda+BG}$	T: 0.3308(11)	T: 0.3192(58)	0.2795(29)	0.2735(25)	0.2759(37)	0.2469(56)	T: 0.3920(46)	0.3770(27)	0.3719(24)	0.3660(36)
	B: 0.3387(11)	B: 0.3268(57)	0.2949(29)	0.2873(25)	0.2894(38)	0.2717(61)	B: 0.3937(45)	0.3789(27)	0.3708(23)	0.3774(36)
$< \cos >_{BG}$	T: 0.0003(30)	T: -0.2601	-0.1364	-0.0241	0.0583	0.1031	T: -0.0729(147)	0.0313(89)	0.0575(76)	0.1170(113)
	B: 0.0356(32)	B: 0.2825	0.1331	0.0512	-0.0170	-0.0963	B: 0.1144(152)	0.0267(91)	-0.0229(77)	-0.0455(116)
$< \cos^2 >_{BG}$	T: 0.2248(17)	T: 0.1982(101)	0.1728(44)	0.1513(30)	0.1576(45)	0.1705(63)	T: 0.2814(79)	0.2853(47)	0.2862(42)	0.2883(61)
	B: 0.2308(18)	B: 0.2134(96)	0.1687(43)	0.1642(34)	0.1723(50)	0.1777(75)	B: 0.2852(84)	0.2856(48)	0.2834(42)	0.2877(61)
P_Λ	0.0711(80)	-0.0227(691)	0.0968(293)	0.1256(224)	0.1434(310)	0.2130(508)	-0.0018(297)	0.0225(176)	0.0582(155)	0.0700(234)

Table C.13: p_T distributions for long tracks in Λ photoproduction

$<\zeta>$	T: 0.1473	0.1863	0.2255	0.2716	0.3353	0.4529
	B: 0.1470	0.1861	0.2255	0.2713	0.3353	0.4539
N_Λ	T: 4461	10105	11706	14769	13828	9211
	B: 4799	10987	12178	15894	14526	9655
N_{BG}	T: 880	1570	1086	1240	1261	994
	B: 788	1359	988	1189	1123	1150
$mass$	T: 1.1155(4)	1.1155(XX)	1.1155(2)	1.1156(2)	1.1157(2)	1.1158(1)
	B: 1.1158(3)	1.1157(2)	1.1157(2)	1.1158(2)	1.1158(2)	1.1158(1)
σ	T: 0.002014(98)	0.002146(XX)	0.002249(41)	0.002302(31)	0.002470(37)	0.002619(32)
	B: 0.001884(56)	0.002004(30)	0.002088(30)	0.002200(27)	0.002351(43)	0.002517(34)
$<\cos>_{\Lambda+BG}$	T: -0.2339(51)	-0.2080(44)	-0.1965(46)	-0.1567(45)	-0.0853(49)	-0.0189(63)
	B: 0.2520(51)	0.2632(42)	0.2277(45)	0.1765(43)	0.1143(49)	0.0532(60)
$<\cos^2>_{\Lambda+BG}$	T: 0.1965(31)	0.2677(25)	0.3143(26)	0.3472(23)	0.3800(25)	0.4039(30)
	B: 0.2079(31)	0.2881(25)	0.3261(25)	0.3508(23)	0.3868(24)	0.3984(29)
$<\cos>_{BG}$	T: -0.0601(68)	-0.0465(58)	-0.0244(73)	-0.0004(74)	0.0528(81)	0.0826(93)
	B: 0.0918(71)	0.0695(62)	0.0522(77)	0.0345(77)	0.0147(83)	-0.0530(95)
$<\cos^2>_{BG}$	T: 0.1062(32)	0.1600(31)	0.2053(40)	0.2490(40)	0.2970(44)	0.3090(50)
	B: 0.1181(36)	0.1706(34)	0.2092(42)	0.2560(42)	0.2924(45)	0.3093(50)
P_Λ	0.0547(479)	0.1865(244)	0.0825(200)	0.0413(162)	0.0496(156)	0.0686(187)

Table C.14: ζ distribution for long tracks in Λ photoproduction

	$0 < \zeta < 1$	$0 < \zeta < 0.25$					$0.25 < \zeta < 1$			
$< p_T >$	T: 0.5456	T: 0.2824	0.4082	0.5607	0.7306	0.9181	T: 0.4521	0.6158	0.8378	1.1668
	B: 0.5553	B: 0.2827	0.4092	0.5623	0.7305	0.9188	B: 0.4555	0.6166	0.8355	1.1686
N_Λ	T: 44911	T: 7069	10853	9848	3819	1719	T: 1927	4025	4420	1593
	B: 46446	B: 6942	11026	10353	4161	1879	B: 2000	4059	4528	1878
N_{BG}	T: 6975	T: 1727	1681	1171	341	101	T: 254	493	487	235
	B: 5846	B: 1358	1411	985	297	89	B: 201	422	487	196
mass	T: 1.1158(1)	T: 1.1154(0)	1.1155(2)	1.1157(3)	1.1158(4)	1.1157(0)	T: 1.1161(7)	1.1164(1)	1.1164(5)	1.1164(1)
	B: 1.1158(1)	B: 1.1156(3)	1.1157(2)	1.1158(2)	1.1158(4)	1.1157(0)	B: 1.1161(7)	1.1162(2)	1.1163(5)	1.1162(1)
σ	T: 0.002156(18)	T: 0.001767(24)	0.001939(16)	0.002074(19)	0.002222(83)	0.002339(50)	T: 0.002576(101)	0.002590(46)	0.002647(48)	0.002784(72)
	B: 0.002049(11)	B: 0.001696(16)	0.001853(22)	0.001982(16)	0.002060(26)	0.002191(42)	B: 0.002506(141)	0.002567(49)	0.002576(61)	0.002601(60)
$< \cos >_{\Lambda+BG}$	T: 0.2071(25)	T: 0.1242(60)	0.1975(53)	0.2064(57)	0.1513(91)	0.0364(124)	T: 0.3893(107)	0.3479(74)	0.2916(73)	0.1892(121)
	B: -0.1679(26)	B: -0.0796(64)	-0.1575(55)	-0.1474(58)	-0.1055(89)	0.0022(119)	B: -0.3574(109)	-0.3437(75)	-0.2791(73)	-0.1650(116)
$< \cos^2 >_{\Lambda+BG}$	T: 0.3702(13)	T: 0.3357(31)	0.3888(26)	0.4076(27)	0.3707(43)	0.2852(57)	T: 0.4034(65)	0.3705(45)	0.3470(42)	0.3062(65)
	B: 0.3728(13)	B: 0.3448(33)	0.3971(26)	0.4062(27)	0.3652(41)	0.2824(54)	B: 0.3950(65)	0.3698(44)	0.3495(41)	0.3102(62)
$< \cos >_{BG}$	T: 0.2394(27)	T: 0.2008(47)	0.2500(55)	0.2379(73)	0.1934(138)	0.1600(198) $< \cos >_{BG}$	T: 0.3538(185)	0.2990(106)	0.2939(100)	0.1413(189)
	B: -0.2157(30)	B: -0.1631	-0.2132	-0.2206	-0.1897	-0.1669	B: -0.3130(192)	-0.2908(110)	-0.2683(100)	-0.2164(194)
$< \cos^2 >_{BG}$	T: 0.2396(16)	T: 0.1892(28)	0.2492(34)	0.2776(42)	0.2622(71)	0.2138(94) $< \cos^2 >_{BG}$	T: 0.3300(124)	0.2630(70)	0.2521(66)	0.2262(97)
	B: 0.2362(18)	B: 0.1815(32)	0.2434(37)	0.2755(45)	0.2662(73)	0.2190(101)	B: 0.3068(127)	0.2585(71)	0.2356(63)	0.2506(114)
P_Λ	0.0878(90)	T: 0.0895(230)	0.0790(177)	0.1237(182)	0.1036(299)	0.1067(493)	T: 0.0939(509)	0.0143(356)	0.0310(323)	0.0998(525)

Table C.15: p_T distributions for short tracks in Λ photoproduction

$<\zeta>$	T: 0.1316	0.1840	0.2246	0.2704	0.3325	0.4224
	B: 0.1324	0.1840	0.2248	0.2700	0.3323	0.4265
N_Λ	T: 15338	9909	7281	7220	4349	1277
	B: 15467	10538	7649	7423	4523	1366
N_{BG}	T: 3043	1221	643	689	618	204
	B: 2445	1021	583	654	517	247
$mass$	T: 1.1154(2)	1.1157(3)	1.1159(3)	1.1162(4)	1.1165(1)	1.1167(2)
	B: 1.1156(2)	1.1158(2)	1.1159(3)	1.1161(4)	1.1163(1)	1.1165(1)
σ	T: 0.001770(13)	0.002068(18)	0.002307(55)	0.002508(31)	0.002769(46)	0.002927(87)
	B: 0.001701(12)	0.001974(15)	0.002208(34)	0.002452(29)	0.002637(42)	0.002751(85)
$<\cos>_{\Lambda+BG}$	T: 0.0637(40)	0.2394(58)	0.3157(68)	0.3187(62)	0.3033(69)	0.3020(102)
	B: -0.0156(41)	-0.1811(58)	-0.2639(69)	-0.2981(62)	-0.2955(69)	-0.2881(100)
$<\cos^2>_{\Lambda+BG}$	T: 0.3006(19)	0.4327(27)	0.4680(33)	0.4053(35)	0.3283(40)	0.2471(59)
	B: 0.3096(20)	0.4264(27)	0.4611(32)	0.4047(34)	0.3310(40)	0.2480(57)
$<\cos>_{BG}$	T: 0.1767(35)	0.3096(72)	0.3240(123)	0.3066(120)	0.2728(96)	0.2656(160)
	B: -0.1393(40)	-0.2814(79)	-0.3056(124)	-0.3123(121)	-0.2588(100)	-0.2612(164)
$<\cos^2>_{BG}$	T: 0.1812(19)	0.3265(45)	0.3530(71)	0.3279(73)	0.2368(62)	0.1959(90)
	B: 0.1747(22)	0.3176(48)	0.3468(74)	0.3256(74)	0.2295(64)	0.1955(94)
P_Λ	0.1075(164)	0.1154(179)	0.1080(211)	0.0564(238)	0.0248(348)	0.0695(805)

Table C.16: ζ distribution for short tracks in Λ photoproduction

	$0 < x)F < 1$	$0 < x)F < 1$	
$< p_T >$	T: 0.5284	T: 0.2966	0.6318
	B: 0.5192	B: 0.2930	0.6243
N_Λ	T: 1975	T: 615	1373
	B: 1976	B: 633	1352
N_{BG}	T: 200	T: 46	141
	B: 200	B: 53	133
mass	T: 1.1155(6)	T: 1.1155(10)	1.1155(7)
	B: 1.1157(6)	B: 1.1157(9)	1.1157(7)
σ	T: 0.002211(103)	T: 0.002130(175)	0.002266(124)
	B: 0.002080(54)	B: 0.002015(66)	0.002124(84)
$< \cos >_{\Lambda+BG}$	T: -0.0754(113)	T: -0.0777(204)	-0.0742(136)
	B: 0.0932(115)	B: 0.0710(200)	0.1028(139)
$< \cos^2 >_{\Lambda+BG}$	T: 0.2889(60)	T: 0.2881(109)	0.2892(72)
	B: 0.2973(61)	B: 0.2843(103)	0.3025(75)
$< \cos >_{BG}$	T: 0.0160(172)	T: -0.0191(329)	0.0409(199)
	B: 0.0223(177)	B: 0.0908(328)	-0.0094(210)
$< \cos^2 >_{BG}$	T: 0.2194(93)	T: 0.2174(186)	0.2156(106)
	B: 0.2295(95)	B: 0.2250(179)	0.2358(112)
P_Λ	0.0421(479) P_Λ	-0.0346(847)	0.0736(576)

Table C.17: Total distribution for long tracks in Λ SIDIS

$< x_F >$	T: 0.5024	0.7876
	B: 0.5037	0.7890
N_Λ	T: 1055	942
	B: 1101	880
N_{BG}	T: 108	69
	B: 105	80
$mass$	T: 1.1155(8)	1.1156(3)
	B: 1.1157(7)	1.1157(8)
σ	T: 0.002089(84)	0.002406(88)
	B: 0.002037(47)	0.002152(155)
$< \cos >_{\Lambda+BG}$	T: -0.1177(146)	-0.0237(174)
	B: 0.1125(146)	0.0680(181)
$< \cos^2 >_{\Lambda+BG}$	T: 0.2665(79)	0.3161(92)
	B: 0.2717(78)	0.3279(94)
$< \cos >_{BG}$	T: -0.0064(222)	0.0384(277)
	B: 0.0235(223)	0.0028(296)
$< \cos^2 >_{BG}$	T: 0.1911(118)	0.2572(147)
	B: 0.2001(116)	0.2847(160)
P_Λ	-0.0240(686)	0.1102(661)

Table C.18: x_F distribution for long tracks in Λ SIDIS

	$0 < x)F < 1$	$0 < x)F < 1$	
$< p_T >$	T: 0.4755	T: 0.2902	0.5907
	B: 0.4786	B: 0.2928	0.5982
N_Λ	T: 1432	T: 563	896
	B: 1413	B: 559	868
N_{BG}	T: 215	T: 63	116
	B: 184	B: 52	107
$mass$	T: 1.1158(8)	T: 1.1159(11)	1.1157(10)
	B: 1.1158(7)	B: 1.1157(10)	1.1159(9)
σ	T: 0.002245(83)	T: 0.002308(223)	0.002279(68)
	B: 0.002012(107)	B: 0.001918(169)	0.002131(90)
$< \cos >_{\Lambda+BG}$	T: 0.1138(127)	T: 0.1087(199)	0.1180(164)
	B: -0.1050(134)	B: -0.0820(206)	-0.1182(177)
$< \cos^2 >_{\Lambda+BG}$	T: 0.2813(66)	T: 0.2662(107)	0.2905(84)
	B: 0.3040(72)	B: 0.2718(106)	0.3266(96)
$< \cos >_{BG}$	T: 0.1696(143)	T: 0.1338(210)	0.1998(191)
	B: -0.1294(167)	B: -0.0854(238)	-0.1781(213)
$< \cos^2 >_{BG}$	T: 0.2079(82)	T: 0.2054(123)	0.2130(107)
	B: 0.2061(90)	B: 0.1746(113)	0.2185(126)
P_Λ	0.0096(565)	0.0703(923)	-0.0088(693)

Table C.19: p_T distributions for short tracks in Λ SIDIS

x_F	T: 0.4368	0.7739
	B: 0.4440	0.7718
N_Λ	T: 1062	371
	B: 1068	383
N_{BG}	T: 153	42
	B: 106	38
$mass$	T: 1.1156(8)	1.1160(16)
	B: 1.1157(0)	1.1160(17)
σ	T: 0.002097(125)	0.002620(208)
	B: 0.001923(47)	0.002535(209)
$<\cos>_{\Lambda+BG}$	T: 0.1100(150)	0.1217(242)
	B: -0.1069(156)	-0.1008(263)
$<\cos^2>_{\Lambda+BG}$	T: 0.2877(78)	0.2628(123)
	B: 0.3016(83)	0.3123(144)
$<\cos>_{BG}$	T: 0.1755(162)	0.1507(359)
	B: -0.1419(185)	-0.1182(378)
$<\cos^2>_{BG}$	T: 0.2063(96)	0.2240(186)
	B: 0.1967(104)	0.2415(203)
P_Λ	-0.0075(645)	0.0537(1102)

Table C.20: x_F distribution for short tracks in Λ SIDIS

	$0 < \zeta < 1$	$0 < \zeta < 0.25$		$0.25 < \zeta < 1$	
$< p_T >$	T: 0.6696	T: 0.3747	0.6191	T: 0.5884	0.9466
	B: 0.6690	B: 0.3741	0.6233	B: 0.5851	0.9463
N_Λ	T: 13419	T: 1615	3256	T: 4462	3978
	B: 14683	B: 1755	3775	B: 4882	4336
N_{BG}	T: 2637	T: 506	928	T: 540	609
	B: 2419	B: 434	839	B: 499	512
$mass$	T: 1.1154(2)	T: 1.1154(1)	1.1153(1)	T: 1.1155(4)	1.1156(1)
	B: 1.1154(2)	B: 1.1153(1)	1.1152(0)	B: 1.1155(4)	1.1154(4)
σ	T: 0.002213(85)	T: 0.001958(63)	0.002107(47)	T: 0.002208(99)	0.002406(45)
	B: 0.002113(47)	B: 0.001805(52)	0.001976(39)	B: 0.002258(61)	0.002245(88)
$< \cos >_{\Lambda+BG}$	T: 0.1566(43)	T: 0.3223(90)	0.1654(75)	T: 0.1542(83)	0.0768(88)
	B: -0.1621(42)	B: -0.3428(89)	-0.1831(72)	B: -0.1508(81)	-0.0747(86)
$< \cos^2 >_{\Lambda+BG}$	T: 0.3309(24)	T: 0.2799(62)	0.2656(43)	T: 0.3718(43)	0.3749(45)
	B: 0.3346(23)	B: 0.2933(61)	0.2751(42)	B: 0.3815(41)	0.3647(43)
$< \cos >_{BG}$	T: 0.0195(47)	T: 0.1286(101)	0.0009(66)	T: 0.0220(116)	-0.0566(115)
	B: -0.0634(49)	B: -0.1829(101)	-0.0367(66)	B: -0.0706(119)	0.0200(118)
$< \cos^2 >_{BG}$	T: 0.1986(27)	T: 0.1481(56)	0.1352(36)	T: 0.2650(63)	0.2717(63)
	B: 0.2003(28)	B: 0.1588(63)	0.1284(37)	B: 0.2645(66)	0.2714(64)
P_Λ	-0.0124(175)	-0.0029(755)	0.0100(404)	-0.0239(281)	-0.0235(295)

Table C.21: p_T distributions for long tracks in $\bar{\Lambda}$ photoproduction

$<\zeta>$	T: 0.1596	0.2119	0.2787	0.3976
	B: 0.1593	0.2123	0.2782	0.3961
N_Λ	T: 993	3303	4741	4330
	B: 1213	3637	5096	4775
N_{BG}	T: 621	729	548	675
	B: 611	586	526	561
$mass$	T: 1.1152(9)	1.1153(1)	1.1154(4)	1.1156(1)
	B: 1.1152(8)	1.1153(4)	1.1154(4)	1.1155(4)
σ	T: 0.001922(393)	0.002076(43)	0.002167(101)	0.002438(46)
	B: 0.001835(275)	0.001903(57)	0.002134(47)	0.002357(82)
$<\cos>_{\Lambda+BG}$	T: 0.2072(99)	0.2313(77)	0.1678(77)	0.0703(88)
	B: -0.2397(92)	-0.2392(76)	-0.1645(75)	-0.0706(85)
$<\cos^2>_{\Lambda+BG}$	T: 0.2024(59)	0.2914(45)	0.3445(41)	0.3977(44)
	B: 0.2136(59)	0.3010(45)	0.3504(40)	0.3940(42)
$<\cos>_{BG}$	T: 0.0490(74)	0.0251(82)	0.0315(108)	-0.0410(114)
	B: -0.0953(72)	-0.0760(86)	-0.0596(111)	0.0114(117)
$<\cos^2>_{BG}$	T: 0.1119(39)	0.1562(44)	0.2376(60)	0.2924(61)
	B: 0.1210(41)	0.1532(49)	0.2340(62)	0.2917(62)
P_Λ	0.0305(1082)	-0.0353(413)	-0.0194(288)	-0.0144(273)

Table C.22: ζ distribution for long tracks in $\bar{\Lambda}$ photoproduction

	$0 < \zeta < 1$	$0 < \zeta < 0.25$		$0.25 < \zeta < 1$	
$< p_T >$	T: 0.5410	T: 0.3391	0.6086	T: 0.5727	0.9290
	B: 0.5508	B: 0.3428	0.6128	B: 0.5678	0.9304
N_Λ	T: 7688	T: 2087	2756	T: 1746	1212
	B: 8161	B: 2158	3010	B: 1833	1237
N_{BG}	T: 3348	T: 1612	850	T: 313	179
	B: 2802	B: 1377	704	B: 269	164
$mass$	T: 1.1160(0)	T: 1.1155(7)	1.1158(1)	T: 1.1166(3)	1.1168(2)
	B: 1.1157(0)	B: 1.1154(6)	1.1156(5)	B: 1.1161(7)	1.1163(4)
σ	T: 0.002265(35)	T: 0.001846(206)	0.002238(56)	T: 0.002550(66)	0.002785(101)
	B: 0.002177(31)	B: 0.001842(209)	0.002044(59)	B: 0.002530(150)	0.002683(82)
$< \cos >_{\Lambda+BG}$	T: -0.2098(52)	T: -0.1707(92)	-0.1565(98)	T: -0.3469(107)	-0.2559(133)
	B: 0.2239(54)	B: 0.1662(95)	0.2062(98)	B: 0.3459(109)	0.2569(137)
$< \cos^2 >_{\Lambda+BG}$	T: 0.3495(28)	T: 0.3436(51)	0.3761(47)	T: 0.3569(66)	0.3165(77)
	B: 0.3671(29)	B: 0.3511(52)	0.4003(47)	B: 0.3722(66)	0.3317(78)
$< \cos >_{BG}$	T: -0.2128(38)	T: -0.1789(51)	-0.2145(80)	T: -0.2990(141)	-0.2248(166)
	B: 0.1822(44)	B: 0.1580(57)	0.1883(94)	B: 0.2597(155)	0.2264(180)
$< \cos^2 >_{BG}$	T: 0.2255(24)	T: 0.1954(32)	0.2563(47)	T: 0.2629(91)	0.2319(104)
	B: 0.2265(26)	B: 0.1915(36)	0.2702(52)	B: 0.2689(97)	0.2376(109)
P_Λ	-0.0642(231)	-0.0127(423)	-0.1429(356)	-0.0094(556)	-0.0011(639)

Table C.23: p_T distributions for short tracks in $\bar{\Lambda}$ photoproduction

$<\zeta>$	T: 0.1416	0.2090	0.2752	0.3709
	B: 0.1416	0.2096	0.2767	0.3678
N_{Λ}	T: 2267	2240	2232	1048
	B: 2288	2587	2342	1016
N_{BG}	T: 1829	486	351	185
	B: 1599	387	314	180
$mass$	T: 1.1153(6)	1.1159(1)	1.1165(7)	1.1171(1)
	B: 1.1153(6)	1.1157(5)	1.1161(6)	1.1163(2)
σ	T: 0.001796(208)	0.002177(55)	0.002542(64)	0.002793(102)
	B: 0.001805(204)	0.002097(45)	0.002375(59)	0.002923(100)
$<\cos>_{\Lambda+BG}$	T: -0.0821(84)	-0.2792(116)	-0.3071(106)	-0.3034(119)
	B: 0.0840(87)	0.3188(110)	0.3072(107)	0.2960(128)
$<\cos^2>_{\Lambda+BG}$	T: 0.2984(44)	0.4523(57)	0.3862(60)	0.2724(73)
	B: 0.3025(45)	0.4674(53)	0.4025(60)	0.2844(76)
$<\cos>_{BG}$	T: -0.1559(48)	-0.3155(118)	-0.2515(170)	-0.2765(145)
	B: 0.1374(53)	0.2940(137)	0.2614(175)	0.2527(169)
$<\cos^2>_{BG}$	T: 0.1857(28)	0.3362(77)	0.2912(102)	0.2085(94)
	B: 0.1886(31)	0.3417(84)	0.3166(105)	0.2066(98)
P_{Λ}	-0.0488(445)	-0.1013(381)	0.0064(445)	0.0176(826)

Table C.24: ζ distribution for short tracks in $\bar{\Lambda}$ photoproduction

	$0 < \zeta < 1$	$0 < \zeta < 0.25$					$0.25 < \zeta < 1$			
$< p_T >$	T: 0.6905	T: 0.2897	0.4137	0.5616	0.7275	0.9013	T: 0.4617	0.6228	0.8389	1.1822
	B: 0.6969	B: 0.2899	0.4138	0.5630	0.7280	0.8983	B: 0.4633	0.6239	0.8407	1.1829
N_Λ	T: 91540	T: 5285	12551	13720	4918	1338	T: 4482	16139	24188	10562
	B: 100265	B: 5492	13250	15529	5533	1555	B: 4470	16900	26558	12117
N_{BG}	T: 20872	T: 567	1842	2433	935	255	T: 1061	4058	5913	2914
	B: 19696	B: 544	1705	2238	775	229	B: 1117	3930	5809	2839
mass	T: 0.4962(0)	T: 0.4944(1)	0.4951(0)	0.4956(1)	0.4960(1)	0.4963(2)	T: 0.4961(1)	0.4966(1)	0.4971(1)	0.4976(1)
	B: 0.4964(0)	B: 0.4955(1)	0.4958(0)	0.4960(0)	0.4961(1)	0.4960(1)	B: 0.4966(1)	0.4969(1)	0.4969(0)	0.4970(1)
σ	T: 0.005544(22)	T: 0.004202(70)	0.004768(47)	0.005055(51)	0.005385(90)	0.005681(198)	T: 0.005685(104)	0.005990(59)	0.006061(59)	0.006260(74)
	B: 0.005215(20)	B: 0.004208(67)	0.004456(44)	0.004757(43)	0.005075(72)	0.005020(144)	B: 0.005232(98)	0.005566(53)	0.005746(42)	0.005942(62)
$< \cos >_{\Lambda+BG}$	T: -0.1768(20)	T: -0.6815(62)	-0.4445(54)	-0.2954(54)	-0.2169(88)	-0.1940(151)	T: -0.1044(99)	-0.0414(48)	-0.0351(37)	-0.0206(52)
	B: 0.1794(20)	B: 0.6676(64)	0.4499(53)	0.2957(52)	0.2239(85)	0.2244(144)	B: 0.1179(99)	0.0594(48)	0.0359(36)	0.0248(50)
$< \cos^2 >_{\Lambda+BG}$	T: 0.5037(9)	T: 0.6941(28)	0.6292(20)	0.5753(21)	0.5114(37)	0.4142(72)	T: 0.5638(37)	0.4794(20)	0.4270(17)	0.3716(26)
	B: 0.5054(8)	B: 0.6956(27)	0.6296(20)	0.5738(20)	0.5115(36)	0.4287(68)	B: 0.5712(37)	0.4847(20)	0.4315(17)	0.3752(25)
$< \cos >_{BG}$	T: 0.0161(34)	T: -0.4738(172)	-0.1811(123)	0.0221(110)	0.0887(174)	0.1553(289)	T: -0.0407(149)	0.0439(76)	0.0833(57)	0.0984(75)
	B: 0.0270(34)	B: 0.4950(171)	0.2612(116)	0.0810(111)	-0.0046(192)	-0.0835(315)	B: 0.0457(153)	-0.0081(76)	-0.0617(57)	-0.0708(74)
$< \cos^2 >_{BG}$	T: 0.3659(17)	T: 0.6051(68)	0.5398(46)	0.4980(45)	0.4301(81)	0.3348(147)	T: 0.4052(65)	0.3342(36)	0.2863(30)	0.2420(41)
	B: 0.3626(17)	B: 0.6061(71)	0.5351(45)	0.4807(46)	0.4384(82)	0.3392(141)	B: 0.4067(67)	0.3324(36)	0.2834(30)	0.2394(40)
P_Λ	-0.0183(58)	-0.0670(360)	-0.0169(170)	-0.0411(152)	-0.0326(259)	0.0197(555)	0.0217(240)	0.0186(134)	-0.0115(114)	-0.0119(183)

Table C.25: p_T distributions for long track K^0_S in Photoproduction

$<\zeta>$	T: 0.1386	0.1864	0.2260	0.2719	0.3364	0.4589
	B: 0.1385	0.1863	0.2257	0.2719	0.3364	0.4595
N_Λ	T: 9200	12766	14272	19615	20918	16739
	B: 9758	14094	15769	21304	22450	18474
N_{BG}	T: 620	2020	3028	4588	4944	4844
	B: 632	1800	2675	4409	5044	4671
$mass$	T: 0.4941(0)	0.4953(1)	0.4962(1)	0.4966(1)	0.4970(1)	0.4974(1)
	B: 0.4952(0)	0.4959(0)	0.4963(0)	0.4966(0)	0.4968(0)	0.4973(1)
σ	T: 0.004168(43)	0.004797(52)	0.005467(59)	0.005805(51)	0.006070(50)	0.006285(60)
	B: 0.004000(14)	0.004601(45)	0.005108(55)	0.005358(44)	0.005735(46)	0.006022(54)
$<\cos>_{\Lambda+BG}$	T: -0.7518(31)	-0.3961(55)	-0.1851(54)	-0.0832(45)	-0.0388(41)	-0.0004(42)
	B: 0.7380(33)	0.3786(53)	0.1991(52)	0.0966(44)	0.0364(40)	0.0133(41)
$<\cos^2>_{\Lambda+BG}$	T: 0.6597(23)	0.6055(21)	0.5577(21)	0.5010(18)	0.4362(18)	0.3916(21)
	B: 0.6585(22)	0.6036(20)	0.5556(20)	0.5075(18)	0.4383(18)	0.3946(20)
$<\cos>_{BG}$	T: -0.6374(102)	-0.0881(118)	0.0041(104)	0.0567(80)	0.0696(67)	0.0730(54)
	B: 0.6518(91)	0.1989(120)	0.0568(103)	-0.0161(81)	-0.0361(66)	-0.0568(54)
$<\cos^2>_{BG}$	T: 0.5820(64)	0.5419(46)	0.4619(43)	0.3852(36)	0.3127(33)	0.2418(29)
	B: 0.5755(61)	0.5260(48)	0.4568(43)	0.3855(36)	0.3057(32)	0.2386(30)
P_Λ	-0.1241(386)	-0.0773(164)	-0.0030(141)	0.0062(122)	-0.0196(123)	0.0168(140)

Table C.26: ζ distribution for long track K^0_S in Photoproduction

	$0 < \zeta < 1$	$0 < \zeta < 0.25$					$0.25 < \zeta < 1$			
$< p_T >$	T: 0.5704	T: 0.2958	0.4115	0.5602	0.7292	0.9096	T: 0.4502	0.6134	0.8306	1.1545
	B: 0.5714	B: 0.2952	0.4113	0.5621	0.7276	0.9084	B: 0.4506	0.6150	0.8310	1.1581
N_Λ	T: 22465	T: 2283	5364	5646	1812	673	T: 1438	2384	2341	696
	B: 23626	B: 2463	5755	5482	2171	636	B: 1378	2501	2716	618
N_{BG}	T: 11111	T: 918	2413	2335	926	218	T: 866	1397	1328	331
	B: 10348	B: 850	2342	2321	569	246	B: 701	1462	1144	403
$mass$	T: 0.4992(1)	T: 0.4977(2)	0.4989(1)	0.4994(1)	0.4998(2)	0.4999(3)	T: 0.4990(2)	0.4992(2)	0.5000(2)	0.5002(3)
	B: 0.4986(0)	B: 0.4981(2)	0.4985(1)	0.4984(1)	0.4983(2)	0.4979(3)	B: 0.4987(2)	0.4989(2)	0.4992(2)	0.4992(3)
σ	T: 0.005888(53)	T: 0.005838(160)	0.005926(105)	0.006257(107)	0.005953(198)	0.005862(272)	T: 0.005593(208)	0.005301(158)	0.005616(156)	0.006350(329)
	B: 0.005739(50)	B: 0.006157(163)	0.005953(101)	0.005614(102)	0.005965(157)	0.005224(263)	B: 0.005324(188)	0.005310(141)	0.005898(146)	0.005637(302)
$< \cos >_{\Lambda+BG}$	T: 0.2798(20)	T: 0.3907(86)	0.3569(47)	0.2921(44)	0.2156(69)	0.1063(111)	T: 0.2323(50)	0.2254(39)	0.2054(42)	0.1536(89)
	B: -0.2847(21)	B: -0.4108(86)	-0.3668(47)	-0.2945(45)	-0.2118(69)	-0.0858(108)	B: -0.2393(52)	-0.2286(38)	-0.2012(42)	-0.1590(92)
$< \cos^2 >_{\Lambda+BG}$	T: 0.2178(13)	T: 0.3936(53)	0.3014(31)	0.2395(27)	0.1783(41)	0.1236(61)	T: 0.1122(25)	0.1094(20)	0.1085(22)	0.1071(39)
	B: 0.2264(13)	B: 0.4175(52)	0.3158(30)	0.2465(28)	0.1777(40)	0.1130(57)	B: 0.1149(26)	0.1107(19)	0.1105(21)	0.1142(44)
$< \cos >_{BG}$	T: 0.1279(14)	T: 0.1734(120)	0.1485(58)	0.1257(48)	0.1079(62)	0.0695(90)	T: 0.1562(39)	0.1447(31)	0.1392(36)	0.0991(83)
	B: -0.1201(15)	B: -0.1625(137)	-0.1467(61)	-0.1136(50)	-0.0854(68)	-0.0473(89)	B: -0.1476(39)	-0.1426(32)	-0.1330(37)	-0.1117(75)
$< \cos^2 >_{BG}$	T: 0.0844(7)	T: 0.2025(72)	0.1346(33)	0.1040(25)	0.0801(28)	0.0691(37)	T: 0.0633(18)	0.0593(13)	0.0634(15)	0.0762(32)
	B: 0.0868(8)	B: 0.2087(83)	0.1451(34)	0.1137(26)	0.0880(32)	0.0631(36)	B: 0.0605(17)	0.0578(13)	0.0667(16)	0.0727(30)
P_Λ	-0.0087(221)	-0.0587(599)	-0.0255(474)	-0.0475(459)	0.1346(759)	0.1091(1345)	-0.0971(1497)	-0.0736(1135)	0.1346(980)	-0.0816(1706)

Table C.27: p_T distributions for short track K^0_S in Photoproduction

$<\zeta>$	T: 0.1448	0.1862	0.2245	0.2692	0.3303	0.4124
	B: 0.1448	0.1862	0.2246	0.2697	0.3299	0.4157
N_Λ	T: 3685	6151	5228	4732	2398	408
	B: 4206	6448	5352	4780	2558	429
N_{BG}	T: 1100	2662	2793	2649	1394	254
	B: 1067	2513	2443	2452	1312	274
$mass$	T: 0.4988(1)	0.4990(1)	0.4993(1)	0.4993(1)	0.4996(2)	0.5007(4)
	B: 0.4981(1)	0.4983(1)	0.4987(1)	0.4988(1)	0.4992(2)	0.4996(4)
σ	T: 0.006299(123)	0.006144(104)	0.005725(113)	0.005656(118)	0.005743(159)	0.005390(364)
	B: 0.006304(111)	0.005859(96)	0.005519(99)	0.005556(108)	0.005522(142)	0.005848(434)
$<\cos>_{\Lambda+BG}$	T: 0.3924(79)	0.3228(44)	0.2628(37)	0.2276(32)	0.1966(36)	0.1665(73)
	B: -0.4050(75)	-0.3181(44)	-0.2692(38)	-0.2333(33)	-0.1941(37)	-0.1698(65)
$<\cos^2>_{\Lambda+BG}$	T: 0.4517(43)	0.2730(27)	0.1793(22)	0.1275(17)	0.0889(16)	0.0649(26)
	B: 0.4636(41)	0.2735(27)	0.1862(22)	0.1319(17)	0.0914(16)	0.0597(24)
$<\cos>_{BG}$	T: 0.1535(126)	0.1434(62)	0.1302(34)	0.1384(25)	0.1399(34)	0.1266(85)
	B: -0.1049(139)	-0.1363(64)	-0.1273(36)	-0.1352(26)	-0.1309(35)	-0.1521(77)
$<\cos^2>_{BG}$	T: 0.2505(69)	0.1270(34)	0.0856(17)	0.0671(11)	0.0594(13)	0.0492(27)
	B: 0.2554(74)	0.1418(34)	0.0901(18)	0.0681(12)	0.0575(14)	0.0517(26)
P_Λ	-0.0466(408)	0.0513(436)	-0.0025(567)	-0.0570(692)	0.0413(1212)	0.2242(3953)

Table C.28: ζ distribution for short track K^0_S in Photoproduction

	$0 < x)F < 1$	$0 < x)F < 1$	
$< p_T >$	T: 0.5377	T: 0.2955	0.6405
	B: 0.5432	B: 0.2958	0.6445
N_Λ	T: 2913	T: 854	2078
	B: 3055	B: 858	2200
N_{BG}	T: 535	T: 132	375
	B: 491	B: 122	340
$mass$	T: 0.4965(1)	T: 0.4957(2)	0.4970(2)
	B: 0.4965(1)	B: 0.4955(2)	0.4969(1)
σ	T: 0.005667(119)	T: 0.004955(205)	0.005991(147)
	B: 0.005402(113)	B: 0.004664(192)	0.005625(140)
$< \cos >_{\Lambda+BG}$	T: -0.0923(105)	T: -0.1086(200)	-0.0859(123)
	B: 0.0967(105)	B: 0.1530(204)	0.0757(123)
$< \cos^2 >_{\Lambda+BG}$	T: 0.3981(52)	T: 0.4198(99)	0.3887(61)
	B: 0.4103(52)	B: 0.4456(95)	0.3972(61)
$< \cos >_{BG}$	T: 0.0954(206)	T: 0.1030(399)	0.0886(242)
	B: -0.0469(200)	B: -0.0741(401)	-0.0556(229)
$< \cos^2 >_{BG}$	T: 0.3022(110)	T: 0.3601(205)	0.2793(128)
	B: 0.2887(107)	B: 0.3436(211)	0.2639(122)
P_Λ	-0.0133(348)	0.0818(636)	-0.0415(411)

Table C.29: p_T distributions for long track K^0_S in SIDIS

x_F	T: 0.5005	0.8064
	B: 0.4928	0.8042
N_Λ	T: 1442	1505
	B: 1500	1562
N_{BG}	T: 230	243
	B: 200	262
$mass$	T: 0.4959(2)	0.4971(2)
	B: 0.4961(2)	0.4968(2)
σ	T: 0.005272(164)	0.006031(163)
	B: 0.004983(148)	0.005814(180)
$< \cos >_{\Lambda+BG}$	T: -0.1840(154)	-0.0036(140)
	B: 0.1863(156)	0.0100(139)
$< \cos^2 >_{\Lambda+BG}$	T: 0.4478(74)	0.3508(71)
	B: 0.4650(74)	0.3577(70)
$< \cos >_{BG}$	T: 0.1254(315)	0.0809(263)
	B: -0.0145(319)	-0.0419(245)
$< \cos^2 >_{BG}$	T: 0.3564(168)	0.2577(141)
	B: 0.3716(166)	0.2409(130)
P_Λ	-0.0375(488)	0.0032(498)

Table C.30: x_F distribution for long track K^0_S in SIDIS

	$0 < x)F < 1$	$0 < x)F < 1$	
$< p_T >$	T: 0.4846	T: 0.2915	0.5968
	B: 0.4937	B: 0.2915	0.6032
N_Λ	T: 601	T: 203	424
	B: 700	B: 247	489
N_{BG}	T: 304	T: 105	159
	B: 223	B: 58	107
$mass$	T: 0.4998(3)	T: 0.4995(5)	0.5000(4)
	B: 0.4988(3)	B: 0.4986(4)	0.4987(4)
σ	T: 0.005290(288)	T: 0.004899(440)	0.005718(362)
	B: 0.006073(284)	B: 0.005453(372)	0.006531(337)
$< \cos >_{\Lambda+BG}$	T: 0.1586(117)	T: 0.1872(205)	0.1407(142)
	B: -0.1794(118)	B: -0.1957(220)	-0.1700(137)
$< \cos^2 >_{\Lambda+BG}$	T: 0.1534(63)	T: 0.1726(113)	0.1434(76)
	B: 0.1630(67)	B: 0.1950(130)	0.1458(75)
$< \cos >_{BG}$	T: 0.0927(82)	T: 0.0974(156)	0.0940(92)
	B: -0.0760(80)	B: -0.0412(145)	-0.0831(92)
$< \cos^2 >_{BG}$	T: 0.0717(34)	T: 0.0851(73)	0.0636(33)
	B: 0.0731(32)	B: 0.0703(64)	0.0707(34)
P_Λ	-0.1041(1236)	0.0071(2002)	-0.1745(1472)

Table C.31: p_T distributions for short track K^0_S in SIDIS

x_F	T: 0.4758	0.7676
	B: 0.4767	0.7743
N_Λ	T: 415	175
	B: 516	172
N_{BG}	T: 222	77
	B: 139	66
$mass$	T: 0.4997(4)	0.4999(5)
	B: 0.4990(3)	0.4984(7)
σ	T: 0.005453(343)	0.004825(505)
	B: 0.005934(318)	0.006225(622)
$<\cos>_{\Lambda+BG}$	T: 0.1968(145)	0.0738(185)
	B: -0.2203(145)	-0.0786(183)
$<\cos^2>_{\Lambda+BG}$	T: 0.1784(83)	0.0977(77)
	B: 0.1903(88)	0.0944(69)
$<\cos>_{BG}$	T: 0.0965(107)	0.0643(154)
	B: -0.0741(113)	-0.0657(144)
$<\cos^2>_{BG}$	T: 0.0771(48)	0.0624(55)
	B: 0.0749(43)	0.0714(52)
P_Λ	-0.0440(1449)	-0.0425(2890)

Table C.32: x_F distribution for short track K^0_S in SIDIS

	$0 < \zeta < 1$	$0 < \zeta < 0.25$		$0.25 < \zeta < 1$	
$< p_T >$	T: 0.6951	T: 0.3606	0.6095	T: 0.6039	0.9670
	B: 0.6991	B: 0.3610	0.6099	B: 0.6044	0.9699
N_Λ	T: 83561	T: 13269	19937	T: 21746	30162
	B: 92568	B: 14324	22801	B: 23239	33168
N_{BG}	T: 15257	T: 1434	3147	T: 4281	5579
	B: 14071	B: 1360	2599	B: 4093	5586
$mass$	T: 0.4965(0)	T: 0.4949(0)	0.4958(0)	T: 0.4971(0)	0.4977(0)
	B: 0.4967(0)	B: 0.4957(0)	0.4964(0)	B: 0.4968(0)	0.4974(0)
σ	T: 0.005617(24)	T: 0.004542(44)	0.005058(40)	T: 0.005872(58)	0.006401(42)
	B: 0.005282(19)	B: 0.004399(43)	0.004874(37)	B: 0.005587(45)	0.005834(35)
$< \cos >_{\Lambda+BG}$	T: 0.1699(22)	T: 0.5393(49)	0.2886(44)	T: 0.0516(43)	0.0204(34)
	B: -0.1773(21)	B: -0.5383(48)	-0.2854(43)	B: -0.0716(42)	-0.0288(32)
$< \cos^2 >_{\Lambda+BG}$	T: 0.5025(9)	T: 0.6491(19)	0.5468(18)	T: 0.5015(18)	0.4088(16)
	B: 0.5062(9)	B: 0.6520(19)	0.5517(17)	B: 0.5057(17)	0.4134(15)
$< \cos >_{BG}$	T: -0.0661(42)	T: 0.1965(143)	-0.1492(96)	T: -0.0610(78)	-0.0995(61)
	B: 0.0214(44)	B: -0.2383(145)	0.0278(110)	B: 0.0382(80)	0.0737(62)
$< \cos^2 >_{BG}$	T: 0.3695(21)	T: 0.5846(54)	0.4807(44)	T: 0.3487(38)	0.2691(33)
	B: 0.3687(22)	B: 0.5677(54)	0.4531(49)	B: 0.3548(38)	0.2800(33)
P_Λ	-0.0090(60)	-0.0225(187)	-0.0640(131)	0.0253(111)	0.0063(103)

Table C.33: p_T distributions for long track $\bar{K}^0_S$ in Photoproduction

$<\zeta>$	T: 0.1507	0.2123	0.2792	0.4088
	B: 0.1507	0.2122	0.2790	0.4084
N_Λ	T: 12230	18224	24547	30240
	B: 13125	20845	27710	32101
N_{BG}	T: 870	3036	4867	5665
	B: 780	2679	4258	5916
$mass$	T: 0.4945(0)	0.4959(0)	0.4968(0)	0.4978(0)
	B: 0.4955(0)	0.4965(0)	0.4969(0)	0.4974(0)
σ	T: 0.004432(44)	0.005041(51)	0.005743(52)	0.006435(40)
	B: 0.004190(35)	0.004949(40)	0.005503(37)	0.005908(46)
$<\cos>_{\Lambda+BG}$	T: 0.6566(40)	0.2582(48)	0.0835(40)	0.0030(34)
	B: -0.6532(39)	-0.2575(46)	-0.0862(39)	-0.0222(33)
$<\cos^2>_{\Lambda+BG}$	T: 0.6378(21)	0.5644(19)	0.4942(17)	0.4177(16)
	B: 0.6422(20)	0.5689(18)	0.5000(16)	0.4186(15)
$<\cos>_{BG}$	T: 0.3618(157)	-0.1104(101)	-0.1151(79)	-0.0753(58)
	B: -0.3945(169)	0.0128(111)	0.0626(84)	0.0565(59)
$<\cos^2>_{BG}$	T: 0.5932(67)	0.5008(45)	0.3801(38)	0.2670(31)
	B: 0.5769(68)	0.4724(48)	0.3793(40)	0.2785(31)
P_Λ	-0.0369(253)	-0.0441(130)	-0.0213(107)	0.0333(102)

Table C.34: ζ distribution for long track $\bar{K}^0_S$ in Photoproduction

	$0 < \zeta < 1$	$0 < \zeta < 0.25$		$0.25 < \zeta < 1$	
$< p_T >$	T: 0.5643	T: 0.3621	0.6054	T: 0.5613	0.9231
	B: 0.5680	B: 0.3635	0.6058	B: 0.5662	0.9202
N_Λ	T: 19594	T: 5769	7554	T: 3899	2389
	B: 20589	B: 6057	7825	B: 4068	2636
N_{BG}	T: 8020	T: 2303	2791	T: 1872	956
	B: 6811	B: 1894	2437	B: 1533	872
$mass$	T: 0.5004(1)	T: 0.4999(1)	0.5004(1)	T: 0.5005(1)	0.5010(2)
	B: 0.4990(1)	B: 0.4983(1)	0.4991(1)	B: 0.4992(1)	0.4998(1)
σ	T: 0.005988(55)	T: 0.006149(102)	0.006028(88)	T: 0.005806(125)	0.005751(148)
	B: 0.005822(50)	B: 0.005876(90)	0.005728(79)	B: 0.005759(116)	0.005900(146)
$< \cos >_{\Lambda+BG}$	T: -0.2947(22)	T: -0.3866(49)	-0.2950(38)	T: -0.2252(32)	-0.1924(48)
	B: 0.2975(23)	B: 0.4024(50)	0.2913(38)	B: 0.2269(33)	0.1900(47)
$< \cos^2 >_{\Lambda+BG}$	T: 0.2262(15)	T: 0.3455(32)	0.2346(24)	T: 0.1104(16)	0.1134(24)
	B: 0.2327(15)	B: 0.3643(33)	0.2356(24)	B: 0.1139(17)	0.1162(24)
$< \cos >_{BG}$	T: -0.1131(17)	T: -0.1606(68)	-0.1053(48)	T: -0.1267(25)	-0.1149(43)
	B: 0.1041(20)	B: 0.1396(74)	0.1148(50)	B: 0.1242(30)	0.1213(51)
$< \cos^2 >_{BG}$	T: 0.0695(9)	T: 0.1497(43)	0.0943(26)	T: 0.0479(11)	0.0536(18)
	B: 0.0733(10)	B: 0.1526(45)	0.1033(29)	B: 0.0514(13)	0.0642(23)
P_Λ	0.0383(237)	-0.0304(422)	0.0939(395)	0.0807(824)	0.0957(855)

Table C.35: p_T distributions for short track $\bar{K}^0_S$ in Photoproduction

$<\zeta>$	T: 0.1560	0.2104	0.2738	0.3614
	B: 0.1562	0.2102	0.2744	0.3606
N_Λ	T: 4758	7493	5635	1632
	B: 5214	7747	5807	1857
N_{BG}	T: 1574	3141	2408	820
	B: 1266	2668	2116	614
$mass$	T: 0.4999(1)	0.5004(1)	0.5006(1)	0.5009(2)
	B: 0.4982(1)	0.4991(1)	0.4993(1)	0.4995(2)
σ	T: 0.006370(107)	0.005818(90)	0.005903(100)	0.005696(189)
	B: 0.006110(97)	0.005603(82)	0.005680(94)	0.006344(197)
$<\cos>_{\Lambda+BG}$	T: -0.4344(62)	-0.2894(35)	-0.2277(31)	-0.1840(43)
	B: 0.4302(62)	0.2955(35)	0.2282(32)	0.1821(43)
$<\cos^2>_{\Lambda+BG}$	T: 0.4349(37)	0.2122(22)	0.1279(16)	0.0792(18)
	B: 0.4371(37)	0.2188(22)	0.1335(17)	0.0793(18)
$<\cos>_{BG}$	T: -0.1740(108)	-0.1201(46)	-0.1173(25)	-0.1366(40)
	B: 0.1816(121)	0.1151(47)	0.1164(29)	0.1252(53)
$<\cos^2>_{BG}$	T: 0.2099(64)	0.0995(26)	0.0538(11)	0.0461(14)
	B: 0.2338(71)	0.0986(26)	0.0599(13)	0.0476(19)
P_Λ	0.0962(409)	0.0163(451)	0.0536(594)	0.1053(1395)

Table C.36: ζ distribution for short track $\bar{K}^0_S$ in Photoproduction

References

[1] *New American Bible*, page 4. Catholic Book Publishing Company, St. Joseph medium sized edition, 1992.

[2] G. Bunce et al. Λ^0 polarization in inclusive production by 300-Gev protons on beryllium. *Physical Review Letters*, 36(19):1113–1116, 1976.

[3] K. Heller. Spin and high energy hyperon production, results and prospects. In C.W. de Jager, T.J. Ketel, P.J. Mulders, J.E.J Oberski, and M. Oskam-Tamboezer, editors, *Spin 96 Proceedings*, pages 23–30. World Scientific, September 1996. Proceedings of the 12th International Symposium.

[4] G. Bunce et al. Λ^0 polarization in inclusive production by 24 GeV protons on platinum. *Physics Letters*, 68B(5):480–482, 1977.

[5] G. Bunce et al. Polarization of Λ's and $\bar{\Lambda}$'s produced by 400-GeV protons. *Physical Review Letters*, 41(9):607–611, 1978.

[6] G. Bunce et al. A study of inclusive Λ polarization from hydrogen and other targets at 28 gev. *Physics Letters*, 90B(3):319–323, 1980.

[7] G. Bunce et al. Polarization of Ξ and Λ hyperons produced by 400-GeV/c protons. *Physical Review Letters*, 51(22):2025–2028, 1983.

[8] F. Lomanno et al. Measurement of λ^0 polarization in inclusive λ^0 production at 28.5 GeV/c. *Physical Review Letters*, 43(26):1905–1908, 1979.

[9] S. Erhan et al. λ^0 polarization in proton-proton interactions at $\sqrt{s}$ =53 and 62 GeV. *Physics Letters*, 82B(2):301–304, 1979.

[10] Donald H. Perkins. *Introduction to High-Energy Physics*, pages 147–149. Addison-Wesley Publishing Company, 1972.

[11] K. Heller. Hyperon polarization at high energy. In K.-H. Althoff and W. Meyer, editors, *High Energy Spin Physics*, volume 1. Springer-Verlag, September 1990. Proceedings of the 9th International Symposium.

[12] J. Soffer. Is the riddle of the hyperon polarizations solved. In *Batavia 1999, Hyperon physics*, pages 121–126, September 1999.

[13] Julián Félix. On theoretical studies of Λ^0 polarization. *Modern Physics Letters A*, 14(13):827–842, 1999.

[14] A. Simon et al. Documentation 2000: Longitudinal polarimeter. internal note, July 2000.

[15] W. Lorenzon for the HERMES Collaboration. Proposal to desy for a longitudinal electron polarimeter at hera-east section, May 1995. IPR-95-03.

[16] W.R. Leo. *Techniques for Nuclear and Particle Physics Experiments*, pages 17–68. Springer-Verlag, 1994.

[17] The HERMES Collaboration. The hermes spectrometer. *Nuclear Instruments and Methods in Physics Research A*, 417:230–265, 1998.

[18] The HERMES collaboration. Technical design report: Hermes. Technical report, The HERMES Collaboration, July 1993.

[19] Dirk De Schepper, Ralf Kaiser, and Evaristo Cisbani. Particle identification with the hermes rich detector: Description of the different approaches, March 1998. Internal Report: HERMES 98-008.

[20] Frances Halzen and Alan D. Martin. *Quarks and Leptons: An Introductory Course in Modern Particle Physics*. John Wiley & Sons, 1984.

[21] D. Boer and P.J. Mulders. Time-reversal odd distribution functions in leptoproduction. *Phys. Rev. D*, 57:5780–5786, 1998.

[22] P.J. Mulders and R.D. Tangerman. The complete tree-level result up to order $1/Q$ for polarized deep inelastic leptoproduction. *Nuclear Physics B*, 461:197–237, 1996.

[23] Gösta Gustafson Bo Andersson and Gunnar Ingelman. A semiclassical model for the polarization on inclusively produced λ^0-particles at high energies. *Physics Letters*, 85B(4):417–420, 1979.

[24] Thomas A. Degrand and Hannu I. Miettinen. Models for polarization asymmetry in inclusive hadron production. *Phys. Rev. D*, 24(9):2419–2427, 1981.

[25] Jussi Markkanen Thomas A. Degrand and Hannu I. Miettinen. Hyperon polarization asymmetry: Polarized beams and ρ production. *Phys. Rev. D*, 32(9):2445–2448, 1985.

[26] Thomas A. Degrand and Hannu I. Miettinen. Quark dynamics of polarization in inclusive hadron production. *Phys. Rev. D*, 23(5):1227–1230, 1981.

[27] Ken-ichi Kubo Yuichi Yamamoto and Hiroshi Toki. Quark recombination model for spin polarization in high energy inclusive hadron reactions. *Progress of Theoretical Physics*, 98(1):95–128, 1997.

[28] Yuichi Yamamoto Ken-ichi Kubo and Hiroshi Toki. New mechanisms for the anomalous spin observables in high energy hyperon productions. *Progress of Theoretical Physics*, 101(3):615–625, 1999.

[29] K. Suzuki K.-I. Kubo, N. Nakajima and H. Toki. Quark recombination model for polarizations in inclusive hyperon productions at high energy. hep-ph/9906451, June 1999.

[30] Ken-Ichi Kubo and Katsuhiko Suzuki. Spin polarization of hyperons in hadron-hadron inclusive collisions. Oct 2005. hep-ph/0505179.

[31] M. Anselmino et al. Λ polarization from unpolarized quark fragmentation. *Phys. Rev. D*, 63(054029), 2001.

[32] M. Anselmino et al. Transverse λ polarization in unpolarized semi-inclusive dis. hep-ph/0106254, June 2001.

[33] M. Anselmino et al. Transverse lambda polarization in semi-inclusive DIS. hep-ph/0109186, September 2001.

[34] S. A. Gourlay et al. Polarization of λs and $\bar{\Lambda}$s in pp, $\bar{p}p$, and $k^- p$ interactions at 176 GeV/c. *Physical Review Letters*, 56(21):2244–2247, 1986.

[35] E. Reya M. Glück and A. Vogt. Photonic parton distributions. *Phys. Rev. D*, 46(5):1973–1979, 1992.

[36] Robert V. Hogg and Elliot A. Tanis. *Probability and Statistical Inference*, pages 376–387. Prentice Hall, 1993.

[37] Louis Lyons. *Statistics for Nuclear and Particle Physicists*, pages 84–103, 110–120, 152–157, 204–210. Cambridge University Press, 1986.

[38] C. Blocker. Maximum likelihood primer, April 2002.

Author's Biography

Aaron Elvis Jude Andrus was born on November 6, 1975. He graduated from Benjamin Franklin High School in Livonia, Michigan in June of 1993, receiving honors in mathematics, science, English, and social studies. He went on as a partial alumnus scholarship to the University of Michigan-Dearborn where he received his Bachelor's of Science in May of 1997, graduating with honors and a recipient of the Chancellor's Medallion. Then, Aaron came to the University of Illinois in Urbana-Champaign, where he obtained his Master's of Science in May of 2000.

My research and studies at the University of Illinois was paid for teaching assistantships from the University of Illinois at Urbana Champaign's Physics department and from the generous contribution of the NSF grants NSF PHY 00-72044 and NSF PHY 02-44889.